NASA Contractor Report 4689

Spectroscopy and Excitation Dynamics of the Trivalent Lanthanides Tm^{3+} and Ho^{3+} in $LiYF_4$

Brian M. Walsh

Grant NAG1-955
Prepared for Langley Research Center

August 1995

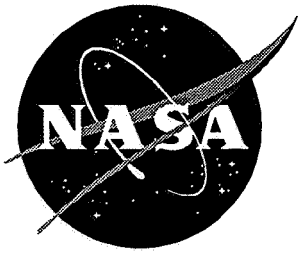

NASA Contractor Report 4689

Spectroscopy and Excitation Dynamics of the Trivalent Lanthanides Tm^{3+} and Ho^{3+} in $LiYF_4$

Brian M. Walsh
Boston College • Chestnut Hill, Massachusetts

National Aeronautics and Space Administration
Langley Research Center • Hampton, Virginia 23681-0001

Prepared for Langley Research Center
under Grant NAG1-955

August 1995

Printed copies available from the following:

NASA Center for AeroSpace Information
800 Elkridge Landing Road
Linthicum Heights, MD 21090-2934
(301) 621-0390

National Technical Information Service (NTIS)
5285 Port Royal Road
Springfield, VA 22161-2171
(703) 487-4650

Dedication

This thesis is dedicated
to the memory of Clayton H. Bair

Spectroscopy and Excitation Dynamics of the Trivalent Lanthanides Tm^{3+} and Ho^{3+} in $LiYF_4$

by

Brian M. Walsh

Thesis Advisor: Dr. Baldassare Di Bartolo

Abstract

A detailed study of the spectroscopy and excitation dynamics of the trivalent lanthanides Tm^{3+} and Ho^{3+} in Yttrium Lithium Fluoride, $LiYF_4$ (YLF), has been done. YLF is a very versatile laser host that has been used to produce laser action at many different wavelengths when doped with trivalent lanthanides. Since the early 1970's YLF has been the subject of many studies, the main goal of which has been to produce long wavelength lasers in the eye safe 2μm region. This study concentrates on a presentation and analysis of the spectroscopic features, and the temporal evolution of excitation energy in YLF crystals doped with Tm^{3+} and Ho^{3+} ions.

Absorption spectroscopy is studied to identify wavelength regions where energy can be absorbed in Holmium YLF and Thulium YLF, and to determine their respective absorption cross sections. These measurements are applied in the Judd-Ofelt theory to determine radiative transition rates of spontaneous emission. Luminescence spectroscopy is studied under cw diode laser excitation at 785nm. The effect of dopant ion concentration and excitation power on the observed luminescence are considered in these measurements. An analysis of these measurements have been used to determine channels of energy transfer between Tm^{3+} and Ho^{3+} ions (cross relaxation, upconversion, and resonant energy transfer). The temporal response of Tm and Ho in singly and co-doped YLF to pulsed laser excitation with a $Ti:Al_2O_3$ laser and a $CoMgF_2$ laser tuned to various wavelengths have also been studied. The energy transfer mechanisms of cross relaxation, upconversion, and resonant energy transfer between Tm^{3+} and Ho^{3+} ions have been modeled, and the model parameters extracted by a fitting procedure to the measured temporal response curves. Rate equation approaches to modeling are presented that result in predictions of rate constants for energy transfer processes, as well as more conventional approaches to modeling such as the Förster-Dexter models, which give the interaction strengths in terms of microscopic interaction parameters.

Acknowledgments

I would like to thank my Advisor at Boston College, Professor Baldassare Di Bartolo, for giving me the opportunity to conduct my research for this thesis at NASA Langley Research Center. I have benefited over the years from his teaching, guidance, wisdom, and friendship. His willingness to understand the human aspects of life's endeavors is a quality I greatly admire.

I would like to acknowledge the support of NASA grant NAG 1-955. I would especially like to express my gratitude to Clayton H. Bair and Phillip Brockmann for offering me the opportunity to work with them during my first two years at NASA. They were always willing to lend assistance to my endeavors in the laboratory. I am grateful for having had the opportunity to work with them. It was an experience that was both instructive and enjoyable.

My appreciation also goes to Ed Modlin, Technician Extraordinaire, who kept the workings of my experimental apparatus, well...working. I also enjoyed the endless hours of comic relief he provided me with his jokes and sense of humor.

To my other co-workers at NASA, namely Guzin Armagan, Waldo Rodrigez, Phillip Narajno, Elizabeth Filer, Norman Barnes, Addison Inge, and Stephanie Vay, I express my thanks for their collaborative assistance during my research.

I would like to thank Drs. David Broido, Kristof Kempa, Guzin Armagan, and Norman Barnes for serving on my thesis committee.

To my friends and family, what can I say, but thanks for being there 100% not 99.

Table of Contents

List of Tables

Chapter 8

List of Figures

Chapter 7

CHAPTER 1
Introduction

Every story involves one or more archetypes. To make a good story a single archetype is usually enough.

Umberto Eco
Travels in Hyperreality

1.1 Overview

A notable feature of the rare earth (RE) ions when doped into crystals is the large number of sharp lines in the absorption and emission spectra. The wavelengths of these lines range from the ultraviolet to the infrared. Solid state crystals, which are insulators, have a band gap that corresponds to the energy of an ultraviolet photon, so that visible or infrared luminescence is not expected from the pure (undoped) crystal. The bulk material in which the RE ions are imbedded will have a perturbative effect on the ions that serves to shift and split the free ion energy levels. These perturbed electronic states can also interact with the phonon states of the crystal lattice to produce various effects. Despite this, the situation is greatly simplified since the band structure of the solid does not play a part in the absorption and emission characteristics of the RE ion.

An emitting solid is, nevertheless, a complicated system consisting of a large number of ions, each of which is capable of interacting with its neighbors. Once the ions are excited with a suitable source, the effects of these interactions becomes manifest. Generally, in the case of RE ions a diverse assortment of luminescent phenomena are observed. The challenge is to differentiate between the various luminescent behaviors that are observed, to identify the channels through which energy is transferred, and to determine the nature of the interaction that promotes transfer.

This situation is complicated enough in materials that contain only a single ion species, so it is no surprise that the complexity is increased when ions of different species are introduced. This increased complexity, however, has a beneficial aspect in that it can be used to produce luminescence in an ion of one species by exciting an ion of another species (sensitized luminescence). This, of course, makes possible a diverse range of lasing action in RE doped crystals under various excitation schemes.

This thesis describes a series of experiments designed to probe into the spectroscopy and excitation dynamics of Lithium Yttrium Fluoride $LiYF_4$ (YLF) containing Tm^{3+} and Ho^{3+} ions. The research addresses the full problem of the dynamics of excitation energy. This will take into account the spectroscopic details of absorption and emission lines in co-doped and singly doped YLF crystals, the channels of their excitation and their respective decay behavior. Various experimental parameters have been varied, such as concentrations of the dopant ions, wavelength of the excitation source and power of the excitation source. This is useful as an aid to differentiate between various competing processes which occur in these complex systems, and to facilitate the task of determining which of the dopant ions are responsible for which processes, how the ions interact with each other, and their relative importance in the overall behavior of the response of YLF:Tm,Ho systems to an excitation source. Emphasis is placed on a coherent presentation of the experimental data. Careful attention is given towards the interpretation of the experimental results and theoretical analysis of the experimental data.

1.2 Historical Background

The early research on YLF based systems concerned 2μm laser action of sensitized Ho^{3+} YLF. Remski, et al. [Re69] demonstrated energy transfer assisted pulsed lasing action at 77°K of Ho^{3+} in YLF:Er,Ho. Chiklis, et al. [Ch71] demonstrated

flashlamp pumped high efficiency room temperature laser action at 2.065μm in YLF:Er,Tm,Ho. The analysis of the optical spectrum and determination of the energy levels were reported for Tm^{3+} in YLF by Jenssen, et al. [Je75] and for Ho^{3+} in YLF by Karayanis, et al. [Ka76].

The availability of mid-infrared diode lasers in the 1980's initiated a resurgence in Ho^{3+} sensitized lasers because diode pumped operation offers an attractive alternative to lamp-pumped schemes and also because the GaAlAs diode emission has a good spectral overlap with the absorption of Tm^{3+}, making for an efficient, site selective pumping scheme. A sampling of studies using diode-laser pumping to achieve 2μm laser action in Ho^{3+} sensitized YLF include Kintz, et. al. [Ki87], Hemmati [He89], Esterowitz [Es90], Budini, et al. [Bu92] and Storm [St93].

Despite the abundance of studies involving lasing schemes in YLF systems, there remains a paucity of spectroscopic studies in the literature. Brenier, et al. [Br89] in an extensive paper, studied the excited state dynamics of Tm^{3+} ions in YLF and the Tm^{3+} -> Ho^{3+} energy transfer in YLF. In this study they examined the processes of upconversion, cross relaxation and energy transfer to explain the observed response of YLF:Tm and YLF:Tm, Ho systems to pulsed excitation at various wavelengths. Ozen [Oz91] in her Ph.D. thesis examined the energy transfer process between Tm^{3+} and Ho^{3+} in YLF. This study examined the temperature dependence of the decay of Tm^{3+} and Ho^{3+} in YLF under excitation from a tunable dye laser and the spectroscopic features under tungsten lamp excitation.

1.3 Purpose

Rare earth doped solid state materials have become an important class of solids attracting much attention among researchers, as is evidenced by the abundance of studies

that can be found in the literature. There are two reasons promoting an incentive to study these materials. The first reason is technical and the second rests on scientific grounds.

From a technical point of view, rare earth materials have been used in a wide variety of optical technologies (i.e., lasers, IR quantum counters, television, and lamp phosphors.) The research at NASA Langley Research Center has focused on the development of reliable, compact solid state lasers in the eye safe 2μm range for remote sensing of the earth's atmosphere from space. From a scientific point of view, a basic understanding of excitation transport in inhomogeneous and disordered solids has the potential for usefulness in many branches of physics.

As was mentioned earlier in this chapter, a substantial amount of work has been done on the lasing characteristics of RE solid state materials. It is the case, however, that spectroscopic measurements are somewhat sparse in light of the importance some of the solid state lasers have achieved. This has especially been the case regarding Tm^{3+} and Ho^{3+} singly and co-doped YLF systems. This situation seems to be improving. During the course of the research for this thesis YLF has seemed to be attracting even more attention from a spectroscopic point of view. Most of these studies have concentrated on specific topics, the results of which have been presented at scientific conferences in the form of slim articles. A comprehensive characterization YLF:Tm,Ho from a spectroscopic point of view has not yet been achieved. Many important questions remain unanswered. The intent of this thesis is not to answer all of these questions, but to conduct a study that covers many topics with the intent of connecting the various aspects in a uniform and consistent manner.

As this thesis will show, especially in the later chapters, YLF:Tm,Ho is an extremely complex system. It displays a bewildering plethora of complex and competing processes. These processes comprise the topic of energy transfer. Energy transfer

manifests itself in various forms (i.e., upconversion, cross relaxation, and direct transfer). These various forms of transfer will be explained at such time when they arise in the context of the thesis.

A number of spectroscopic properties are of importance for the modeling and understanding of YLF:Tm,Ho lasers. These include radiative decay rates, absorption and emission cross sections, energy levels, Boltzmann fractions, and various energy transfer rates. This thesis seeks, as one of its goals, to determine specific values for these physical parameters whenever possible. This set of values will be useful for those researchers attempting to understand and model the optical and temporal behavior of the emission from YLF:Tm,Ho.

1.4 Preview of Contents

Spectroscopic measurements of the absorption in YLF:Tm and YLF:Ho were made, and used in the Judd-Ofelt theory to calculate radiative transition rates between sets of energy levels (manifolds). Radiative transition rates were also calculated independently by comparison of measured emission cross sections and emission cross sections derived from absorption cross sections.

Luminescence measurements under cw diode excitation have been made. The effect of dopant ion concentration is studied by recording the luminescence from various manifolds under the same experimental conditions. Comparison of the spectra allows for a determination of how an increase or decrease in a given dopant ion concentration affects the luminescence of the system as a whole, and helps to identify channels of excitation. The response of the system to changes in the power of the excitation source is also studied. The power of the excitation source affects the distribution of energy in the excited states of the system. Changing the power may increase or decrease the number of

excitations in a set of energy levels. Such changes represent a loss or a gain in the medium. Upconversion, for example, is a process in which an excited ion transfers its energy to another excited ion, exciting it to a higher level. This process results in a loss for one set of levels and a gain for another set of levels. Therefore, studying the response under changes in excitation power helps to identify which levels show a gain or a loss, and indicate how the levels are populated.

The temporal response of the system under pulsed excitation at several different wavelengths has also been studied. The rate of change of populations in sets of energy levels has been studied with models that describe the observed behavior. Direct energy transfer from Tm -> Ho is accounted for in an analysis of rate equations. Cross-relaxation is accounted for in a model that incorporates spatial averaging over donor environments and diffusion among thulium ions. A descriptive analysis of the decay data is also employed in conjunction with other spectroscopic experiments to identify the modes and channels of excitation.

1.5 Outline of Contents

In the next chapter the theory of rare earth ions in solids is presented. Electronic configurations, the crystal field, energy levels, and the electron-phonon interaction is discussed. An outline of the principles involving the Judd-Ofelt theory are presented and methods of calculating emission cross sections are given. Finally, some models of energy transfer and their applicability are discussed.

In chapter 3, YLF as a host lattice is presented. The structure and symmetry of YLF crystals are discussed. The mechanical, thermal and optical properties have been collected from the literature and are tabulated here.

In chapter 4, the experimental apparatus and spectroscopic samples used in this study are presented. The details and specifications of absorption, cw emission and pulsed emission measurement apparatus are given in detail. Methods of measuring the polarized spectra are also given to unambiguously establish a proper reference for the spectra presented in this thesis. Finally the spectroscopic samples used in this thesis are listed, along with their RE ion dopant concentrations and growth method.

In chapter 5, the results and interpretation for YLF:Ho are presented. The Judd-Ofelt theory is applied to YLF:Ho and radiative rates are calculated for a number of levels. Absorption spectra and cw emission spectra in terms of cross sections are given. Finally, the temporal behavior of YLF:Ho to pulsed excitation is presented.

In chapter 6, the results and interpretation for YLF:Tm are presented. The Judd-Ofelt theory is applied to YLF:Tm and radiative rates are calculated for a number of levels. Absorption spectra and cw emission spectra in terms of cross sections are given. Finally, the temporal behavior of YLF:Tm to pulsed excitation is presented, with special attention to characterizing and modeling cross-relaxation. Rates for the processes are calculated based on the model parameters.

In chapter 7, the results and interpretation of co-doped YLF:Tm,Ho are presented. Sensitized luminescence is discussed and a descriptive analysis of the spectroscopic data is made. Upconversion is considered and rates are extracted from power dependent luminescence measurements. Decay data is presented and rate equation modeling is used to describe the Tm -> Ho energy transfer.

The thesis ends with a summary of results and conclusions. Some suggestions for future work are also put forth.

References to Chapter 1

[Br89] A. Brenier, J. Rubin, R. Moncorge and C. Pedrini, "Excited state dynamics of the Tm^{3+} ions and the Tm^{3+} - Ho^{3+} energy transfer in $LiYF_4$," J. Phys. France **50**, 1463-1482 (1989)

[Bu92] P.A. Budini, M.G. Knights, E.P. Chiklis, and H.P. Jenssen,"Performance of a Diode-Pumped High PRF Tm, Ho:YLF Laser," IEEE J. Quantum Elec. **28**, 1029-1032 (1992)

[Ch71] E.P. Chiklis, C.S. Naiman, R.C. Folweiler, D.R. Gabbe, H.P. Jenssen, and A. Linz,"High efficiency room temperature 2.06μm laser using sensitized Ho^{3+} :YLF," Appl. Phys. Lett. **19**, 119-121 (1971)

[Es90] L. Esterowitz,"Diode-pumped holmium, thulium, and erbium lasers between 2 and 3μm operating cw at room temperature," Opt. Eng. **29**, 676-680 (1990)

[He89] H. Hemmati, "2.07-μm cw diode-laser pumped Tm,Ho:$YLiF_4$ room-temperature laser," Opt. Lett. **14**, 435 (1989)

[Je75] H.P. Jenssen, A. Linz, R.P. Leavitt, C.A. Morrison and D.E. Wortman,"Analysis of the optical spectrum of Tm^{3+} in $LiYF_4$," Phys. Rev. **B11**, 92 (1975)

[Ka76] N. Karayianis, D.E. Wortman and H.P. Jenssen, "Analysis of the optical spectrum of Ho^{3+} in $LiYF_4$," J. Phys. Chem. Solids **37** ,675-682 (1976)

[Ki87] G.J. Kintz, L. Esterowitz, and R. Allen,"Cascade laser emission at 2.31μm and 2.08μm from laser diode-pumped Tm,Ho:YLF at room temperature," in *Tech. Dig.*, OSA Tunable Solid State Laser Conf., 1987, **vol. 20**, paper MC2, p.20

[Oz91] G. Ozen Ph.D. Thesis, "Energy Transfer Processes Between Tm^{3+} and Ho^{3+} in $LiYF_4$," NASA Contractor Report 187578 (1991)

[Re69] R.L. Remski, L.T. James, K.H. Gooen, B. Di Bartolo, and A. Linz, "Pulsed laser action in $LiYF_4$:Er^{3+}, Ho^{3+} at 77°K," IEEE J. Quantum Electron. **QE-15**, 214 (1969)

[St93] M.E. Storm, "Holmium YLF Amplifier Performance and the Prospects for Multi-Joule Energies Using Diode-Laser Pumping," IEEE J. Quan. Elec. **29**, 440 (1993)

CHAPTER 2
Theory of Rare Earth Ions In Solids

There is a theory which states that if ever anyone discovers exactly what the Universe is for and why it is here, it will instantly dissapear and be replaced by something even more bizarre and inexplicable.

Douglas Adams
The Restaurant at the end of the Universe

2.1 Electronic Configuration

The rare earths are divided into two sets of elements, the *lanthanides* and the *actinides*. The neutral forms of these elements have an electronic configuration made up by progressively filling the 4f electronic shell for the lanthanides and the 5f electronic shell for the actinides. A feature common to all the elements in the lanthanide series is a Xenon based electronic structure ($1s^2 2s^2 2p^6 3s^2 3p^6 3d^{10} 4s^2 4p^6 4d^{10} 5s^2 5p^6$) with two or three outer electrons ($6s^2$ or $5d6s^2$). The energy and spatial extent of the 4f wavefunctions show a sudden decrease at the beginning of the lanthanide series. Continuing through the lanthanide series, each additional added electron is accompanied by an increase in the effective nuclear charge. This causes a reduction of the 4f shell because of the imperfect shielding of one 4f electron with another. Each element of the lanthanide series is characterized by the number of 4f electrons it possesses, n=1 for Cerium through n=14 for Lutecium. The lanthanides are ionized by successive removal of electrons. The first stage of ionization consists of removal of a 6s electron, the second by removal of an additional 6s electron, and the third by removal of all the 6s and 5d electrons or perhaps a 4f electron. This third stage of ionization comprise the triply ionized lanthanides, which are the most common valence states of RE ions in solids.

Many of the properties of rare earth ions result from the fact that the contracted 4f shell behaves as an inner shell. Since it behaves as an inner shell, the 4f wavefunctions do not penetrate into the environment outside the electronic configuration. The result is that the $5s^2 5p^6$ shell shields the f-electrons from interactions originating in the ions environment.

2.2 The Crystal Field

To study the energy level structure of electron configurations of rare earth ions in solids, the effect of the crystal lattice must be taken into account. When an ion is placed in a crystal lattice the free-space electronic energy levels are modified by interactions with the new environment. Typical absorption and emission spectra of RE ions in solids show groups of sharp lines indicating that these various groups of lines are due to transitions between 4f free ion states that are split by interactions with the surrounding charges of the lattice. In other words, the cumulative effects of the lattice charges surrounding the ion cause a perturbation that splits the ionic energy levels into sub levels. By splitting, it is meant that the 2J+1 fold degeneracy is partially removed. This is the well-known *Stark effect*. The perturbation that causes the splitting is an electrostatic field known as the *crystal field*. The theory that describes this effect is known as *crystal field theory*. In reality, however, a more general ligand field theory gives a more accurate picture. In this theory, covalent bonding plays an additional role since the electrons of the ion are partially shared with the surrounding ions or ligands. As was mentioned earlier, however, the shielding of 4f electrons from the surrounding environment reduces this effect. Ligand field theory is more appropriate to systems of transition metal ions, which are not shielded from the surrounding environment. Crystal field theory is then an accurate approximation when applied to RE ions.

If the above suppositions are correct then we must reconcile the above with the fact that transitions between 4f Stark levels are forbidden for electric dipole radiation by the parity selection rule, which states that electric dipole transitions can only occur between levels of opposite parity. Since the energy levels of the 4f shell all have the same parity there must be a mechanism that changes the parity of some of the levels. A resolution to this problem was found when it was recognized by VanVleck [Va37] that the crystal field, apart from splitting the energy levels by removing the 2J+1 degeneracy could also mix higher states of opposite parity into the 4f states. Odd power terms in the expansion of the crystal field potential can mix states of opposite parity into $4f^N$ from higher configurations, such as $4f^{N-1}5d$, that make some of the transitions allowed. It should be noted that magnetic dipole transitions do not violate the parity selection rule (e.g., they can occur between states of the same parity). A weaker mechanism that can also contribute to the admixing of states is the interaction of the electronic states with lattice vibrations. This mechanism becomes the dominant one when ions are placed in sites with inversion symmetry, since the crystal field contribution becomes zero in this case.

2.3 Energy Levels of Rare Earth Ions in Solids

The next question to be dealt with is to what extent the crystal field splits the levels and how many levels are obtained for a given crystal field. Wybourne [Wy65] gives an extensive account of this subject.

In general, one starts with a free-ion Hamiltonian H_F given by:

$$H_F = -\frac{\hbar^2}{2m}\sum_{i=1}^{N}\nabla_i^2 - \sum_{i=1}^{N}\frac{Ze^2}{r_i} + \sum_{i<j}^{N}\frac{e^2}{r_{ij}} + H_{S-O} \qquad (2\text{-}1)$$

where the first term is the sum of the kinetic energies of all the electrons of a 4f ion, the second term is the potential energy of all the electrons in the field of the nucleus, the third term is the repulsive Coulomb potential of the interactions between pairs of electrons, and the last term is the spin-orbit Hamiltonian, which accounts for coupling between the spin angular momentum and the orbital angular momentum.

In the free atom there is a spherical symmetry and each level is 2J+1 degenerate. When the ion is placed in a crystal environment the spherical symmetry is destroyed and each level splits under the influence of the crystal field. In fact, the spherical symmetry is reduced to the point symmetry at the ion site. The degree to which the 2J+1 degeneracy is removed will depend on the point symmetry surrounding the ion. This aspect will become clear shortly. The perturbed Hamiltonian for an ion in a crystal is written as:

$$H = H_F + V \tag{2-2}$$

where V, the perturbation Hamiltonian, is due to the potential provided by the crystal environment around the ion. Since the eigenfunctions of the free Hamiltonian possess complete spherical symmetry and are expressible in terms of spherical harmonics, it is natural to expand V in terms of spherical harmonics or operators that transform like spherical harmonics. So, the potential is expanded in terms of the tensor operators C_{kq}:

$$V = \sum_{k,q,i} B_{kq} C_{kq}(\vartheta_i, \varphi_i) \tag{2-3}$$

where the summation over i involves all electrons of the ion of interest. The terms B_{kq} are the coefficients of expansion and are known as *crystal field parameters*. They are generally determined empirically from experimental data. It turns out that for identical 4f

electrons the energy matrix element of V between states of opposite parity (the crystal field split energies) is nonzero only for k even and $k \leq 6$. This follows from the triangle rule for addition of angular momentum $l_1 + l_2 \geq k$. The values for k and q are also limited by the point symmetry of the ion. This arises from the fact that the Hamiltonian must be invariant under operations of the point symmetry group. Thus, the crystal field must also exhibit the same symmetry as the point symmetry of the ion, since it is part of the total Hamiltonian. Equating the crystal field expansion with the expansion that has been transformed through operations of the point symmetry group gives the crystal field for a particular ionic point symmetry. Thus, the spherical symmetry of an ion in a crystal is reduced to the point symmetry at the site of the ion.

Once the point symmetry and the appropriate form of the crystal field are known, it is possible to construct the crystal field energy matrix. This matrix is then diagonalized using an estimated set of starting parameters. The resulting theoretical set of energy levels are compared to the set of experimental levels and, by an iterative fitting procedure, the parameters are adjusted to obtain the best overall fit to experiment.

The thirty-two crystallographic point groups can be divided into four general symmetry classes as follows [Ru56]:

1. Cubic: O_h , O , T_d , T_h , T
2. Hexagonal: D_{6h} , D_6 , C_{6v} , C_{6h} , C_6 , D_{3h} , C_{3h} , D_{3d} , D_3 , C_{3v} , S_6 , C_3
3. Tetragonal: D_{4h} , D_4 , C_{4v} , C_4 , D_{2d} , S_4
4. Lower symmetry: D_{2h} , D_2 , C_{2v} , C_{2h} , C_2 , C_s , S_2 , C_1

It can be shown that knowledge of the symmetry class at the site of the ion can be used to predict the number of levels a given J state splits into. The number of levels a state of angular momentum J splits into for a given point symmetry is presented in table

2-1. Alternatively, rare-earth ions can be used to probe the crystal symmetry if the number of levels of the ion can be determined.

Table 2-1 Splitting Under Point Symmetry For Integral J

J=	0	1	2	3	4	5	6	7	8
Cubic	1	1	2	3	4	4	6	6	7
Hexagonal	1	2	3	5	6	7	9	10	11
Tetragonal	1	2	4	5	7	8	10	11	13
Lower symmetry	1	3	5	7	9	11	13	15	17

As has already been stated, the positions of the levels arise from a combination of the Coulomb, spin-orbit, and crystal field interactions. These splittings of the $4f^N$ configuration are shown in figure 2-1. The electrostatic interaction leads to a split ^{2S+1}L on the order of 10^4 cm^{-1}. The spin-orbit interaction splits the levels further into $^{2S+1}L_J$, separating the J states by 10^3 cm^{-1}. Finally, the crystal field removes or partially removes the degeneracy in J yielding an energy level separation on the order of 10^2 cm^{-1}. The extent to which the Stark split sublevels spread depends on the strength of the crystal field. The larger the crystal field, the larger will be the spread of the J sublevels. Figure 2-2 is a more explicit example, Holmium $LiYF_4$ in this case, of how the states split under various interactions.

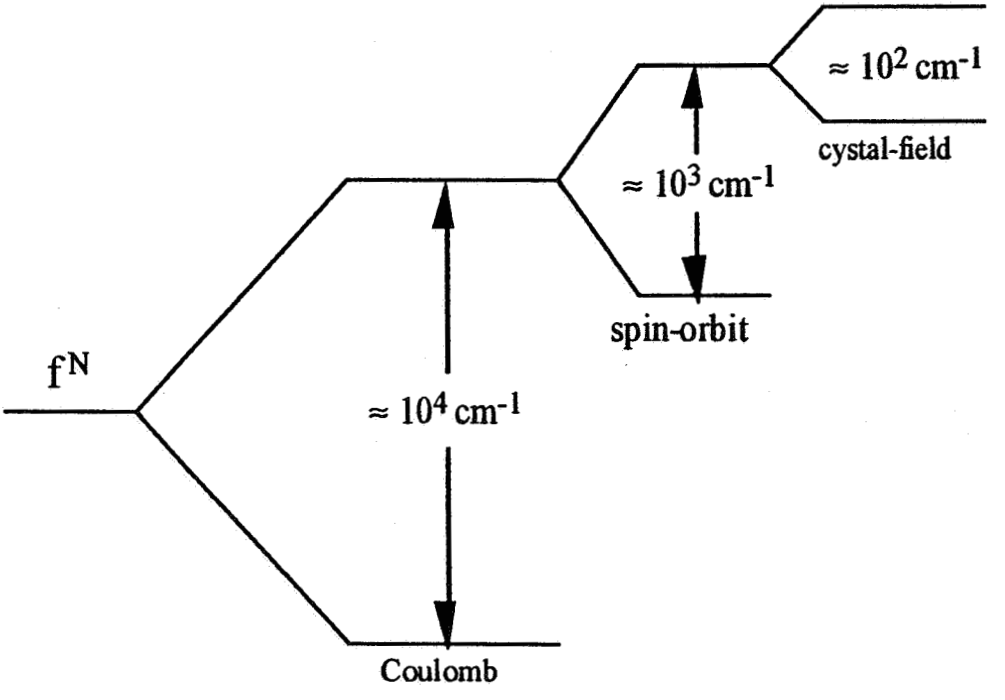

Figure 2-1 Energy Level Splittings Under Various Interactions

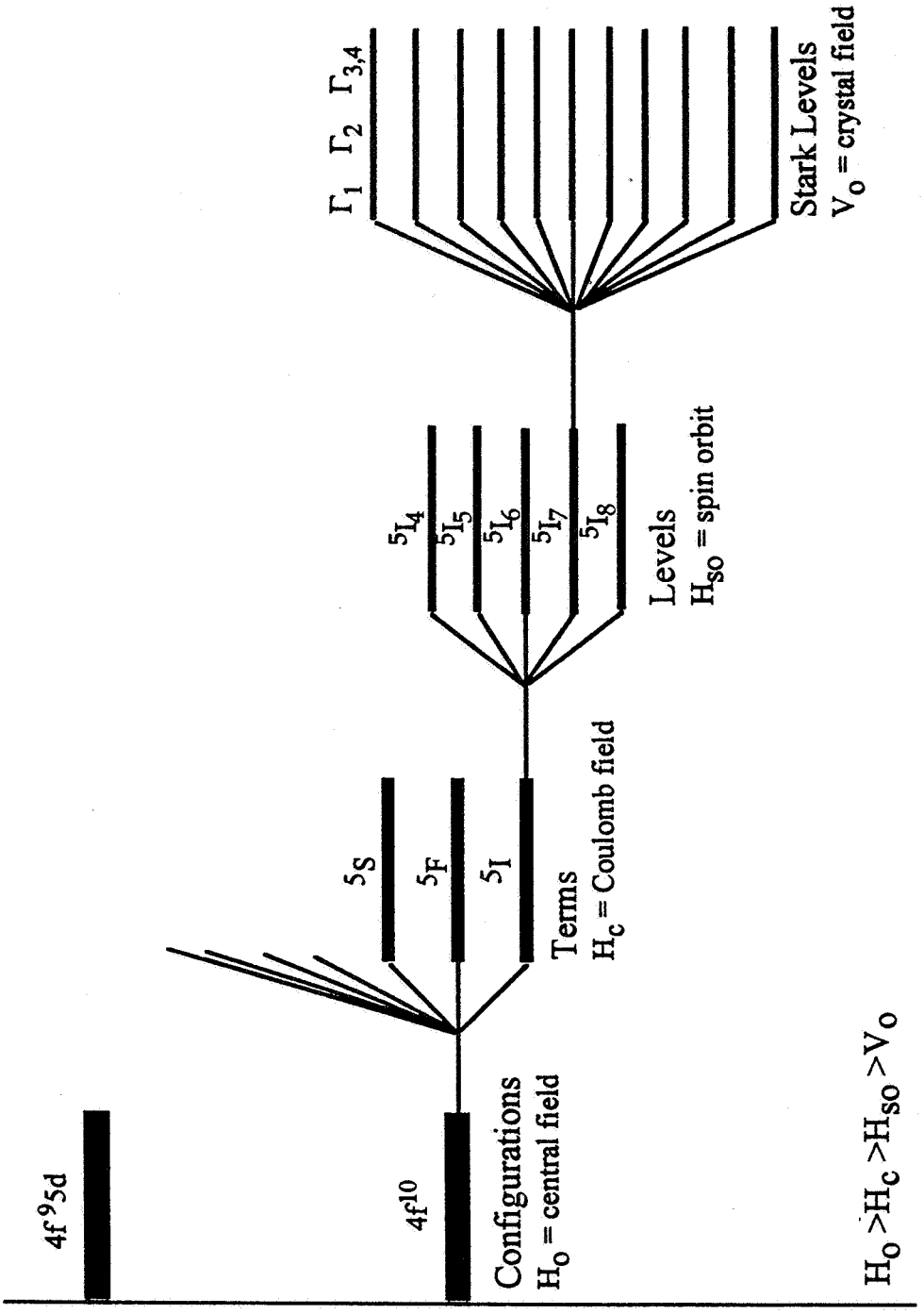

Figure 2-2 Energy Level Scheme of Ho^{3+} $LiYF_4$

2.4 Electron-Phonon Interaction

When the lattice and the ion are treated as a coupled system, optical transitions are considered to occur between vibrational-electronic or vibronic states. Due to this extra dynamical interaction, the Hamiltonian in eq. 2-3 must be modified as:

$$H = H_I + H_P + H_{IP} \qquad (2\text{-}4)$$

where $H_I = H_F + V$ is the energy of the ion (free ion plus static crystal field), H_P is the phonon field energy, and H_{IP} is the interaction energy between the ion and the lattice. This last term is the one responsible for transitions between crystal field levels through creation or annihilation of phonons.

The crystal lattice can vibrate over a range of frequencies, producing relaxation by emission or absorption of phonons in that range of frequencies. These phonons usually have characteristic frequencies less than the energy difference between which the transitions occur, the J states. Several phonons are then required to conserve energy. This multiphonon relaxation is not the only manifestation of the oscillating crystal field. Line broadening, the appearance of vibrational sidebands in the optical spectra, the dependence of linewidth and the position of spectral lines on temperature are some other effects which result from the interaction of the lattice with the ion.

2.5 Intensities of Rare Earth Spectra

The optical spectra of rare earth ions in solids arise primarily from electric and magnetic dipole transitions between Stark split multiplets of the $4f^N$ electronic configuration. Electric dipole transitions are parity forbidden between levels of the $4f^N$ configuration, while those of magnetic dipole origin are allowed. It is known from

experiment, however, that the significant contributions to the intensities of most transitions are electric dipole in nature. This is due to the mixing of opposite parity, higher level energy configurations with the $4f^N$ configuration, such as $4f^{N-1}5d$. This admixing of configurations is caused primarily by the odd-order terms in the crystal Stark field. It should be noted, however, that even though magnetic dipole radiation is about six orders of magnitude smaller than electric dipole radiation in free ions, the electric dipole radiation occurs as a consequence of a perturbation for ions in a crystal. As such, some transitions show a significant magnetic dipole contribution.

Judd [Ju62] and Ofelt [Of62] have shown that the line strength from the initial J manifold $\langle \psi J|$ and the terminal J′ manifold $|\psi' J'\rangle$ can be expressed as a simple sum of the elements of tensor operators and phenomenological Judd-Ofelt parameters, which is given in eq. 2-5.

$$S_{ED} = \sum_{\lambda=2,4,6} \Omega_\lambda \left| \left\langle \psi J \| U^{(\lambda)} \| \psi' J' \right\rangle \right|^2 \tag{2-5}$$

where $\langle \psi J || U^{(\lambda)} || \psi' J' \rangle$ are the doubly reduced matrix elements.

To arrive at this result, let $|\psi J\rangle$ and $|\psi' J'\rangle$ be two states of the $4f^N$ configuration that become slightly admixed with states $\alpha = (\psi'' J'')$ from configurations like $4f^{N-1}5d$. From perturbation theory we get two mixed parity states Ψ_a and Ψ_b given by:

$$\langle \Psi_a | = \langle \psi J | - \sum_\alpha \frac{\langle \psi J | V | \alpha \rangle \langle \alpha |}{E(\psi J) - E(\alpha)} \tag{2-6}$$

$$|\Psi_b\rangle = |\psi' J'\rangle - \sum_\alpha \frac{|\alpha\rangle \langle \alpha | V | \psi' J' \rangle}{E(\psi' J') - E(\alpha)} \tag{2-7}$$

where V is the operator of the crystal interaction energy. The electric dipole operator can be written in a tensor operator form as:

$$P_\rho = -e\sum_i r_i \left(C_\rho\right)_i \tag{2-8}$$

where $\rho = 0$ corresponds to the z-components for absorption or emission of π-polarized light, and $\rho = \pm 1$ gives the $x \pm iy$ components for σ-polarized light. The matrix element of the electric dipole operator to first order in the crystal field perturbation is written as:

$$\langle \Psi_a | P_\rho | \Psi_b \rangle = -\sum_\alpha \frac{\langle \psi J | V | \alpha \rangle \langle \alpha | P_\rho | \psi' J' \rangle}{E(\psi J) - E(\alpha)} - \sum_\alpha \frac{\langle \psi' J' | P_\rho | \alpha \rangle \langle \alpha | V | \psi' J' \rangle}{E(\psi' J') - E(\alpha)} \tag{2-9}$$

This equation does not lend itself to further calculations unless some approximations are made. Judd and Ofelt made two assumptions. The first was to assume that the states $\alpha=(\psi'' J'')$ are completely degenerate, which is equivalent to assigning to them an average energy $E_\alpha = E(\alpha)$. This allows one to remove the terms in the denominator from the sum and invoke the closure relation $\sum |\alpha\rangle \langle\alpha| = 1$. If $|\alpha\rangle = |5d\rangle$ then clearly this assumption constitutes a weak link in the theory since the energies of 5d states span a range of about 50,000 cm^{-1} (from 50,000 cm^{-1} to 100,000 cm^{-1}) encompassing many different states with many different average energies. However, if the 5d configurations are sufficiently complex and encompass many different terms, which when broken into individual sums over closely lying terms produced average energies that were roughly proportional to each other, then the error of this assumption would be reduced. Now, the second assumption is to take:

$$E(\psi J) - E_\alpha = E(\psi' J') - E_\alpha \tag{2-10}$$

This assumption is equivalent to the supposition that the $4f^{N-1}5d$ configurations lie far above the states involved in the transitions. This assumption is fairly well met, but carries with it the error associated with E_α. At any rate, from these assumptions and the use of tensor operator algebra, one arrives at equation 2-5.

The only other point to mention about eq. 2-5 is that the doubly reduced matrix elements vanish for λ odd or $\lambda \geq 6$. The values for the matrix elements can be found in various sources. The most complete set is given by Carnall, Fields and Rajnak [Ca68a]. Experience has shown that the matrix elements vary only by small amounts from host to host, so they can be used regardless of the host materials studied. It should be noted that the expression for one-phonon vibronic transitions has an identical form as that of eq. 2-5 and thus is incorporated into the Judd-Ofelt parameters. An equation similar to eq. 2-5 can also be written for the magnetic dipole contribution to the line strength.

$$S_{MD} = \left(\frac{h}{4\pi mc}\right)^2 \left|\langle \psi J \| L + 2S \| \psi' J' \rangle\right|^2 \qquad (2\text{-}11)$$

Equations 2-5 and 2-11 are related to the spontaneous emission probability.

$$A(\psi J; \psi' J') = \frac{64\pi^4 e^2}{3h(2J+1)\bar{\lambda}^3}\left[n\left(\frac{n^2+2}{3}\right)^2 S_{ED} + n^3 S_{MD}\right] \qquad (2\text{-}12)$$

The connection between eq. 2-12 and experiment is provided by calculating the linestrength from absorption measurements. Specifically, the measured quantities are integrated absorption cross sections, that are related to the experimental linestrength by:

$$S_{ED} = \frac{3hc(2J'+1)}{8\pi^3 e^2 \bar{\lambda}} \cdot n\left(\frac{3}{n^2+2}\right)^2 \int_{\text{manifold}} \sigma(\lambda) d\lambda \qquad (2\text{-}13)$$

The magnetic dipole contribution is given by the equation:

$$S_{MD} = \frac{3h(2J'+1)\bar{\lambda}}{8\pi^2 mc} f_{MD} \qquad (2\text{-}14)$$

where f_{MD} is the magnetic dipole oscillator strength. These have already been calculated for many different transitions in rare-earth ions [Ca68b]. In cases where the magnetic dipole contributes significantly to the line strength it must be subtracted from the electric dipole part.

To evaluate the spontaneous emission probabilities of eq. 2-12, the electric dipole and magnetic dipole line strengths must be calculated. This is easily done for transitions that terminate at the ground state from simple spectroscopy. The advantage of the theory of Judd and Ofelt is that once the set of intensity parameters $\{\Omega_\lambda\}$ are found for a given ion-host combination, they can be used to calculate absorption and emission probabilities between any two f^N levels. They are also useful for calculating radiative lifetimes for any excited manifold since this simply requires summing the transition probabilities of an excited state to every state below it down to the ground state. The way one determines the set of J-O parameters is by performing a least squares fit between the theoretical expression in eq. 2-5 and the expression in eq. 2-13. More about this fitting procedure will be presented in a later chapter when it will be applied Tm^{3+} and Ho^{3+} in YLF.

2.6 Emission Cross Sections

The emission cross section at a given frequency can be determined from one of the forms of the Füchtbauer-Ladenberg formula [Pa92]:

$$\sigma(\nu) = \frac{\lambda^2}{8\pi n^2 \tau_{rad}} g(\nu) \qquad (2\text{-}15)$$

where $g(\nu)$ is the spectral lineshape function, which can be written in terms of the intensity $I(\nu)$ of an emission spectrum as:

$$g(\nu) = \frac{I(\nu)}{\int I(\nu)d\nu} \tag{2-16}$$

It will be useful for purposes later to convert this into an equation involving the wavelength λ. By noting that $I(\nu) = I(\lambda)$ and $d\nu = (c/\lambda^2)d\lambda$ it can be shown that eq. 2-15 can be written as:

$$\sigma(\lambda) = \frac{\lambda^2}{8\pi c n^2 \tau_{rad}} \cdot \frac{I(\lambda)}{\int \frac{I(\lambda)}{\lambda^2} d\lambda} \tag{2-17}$$

It is also possible to obtain the emission cross section from a knowledge of the absorption lineshape and the energy levels of the ground state manifold and an excited state manifold. Equations connecting emission cross sections to absorption cross sections have been derived by McCumber[Mc64] and more recently by Payne et al. [Pa92].

Emission and absorption cross section functions can be written as the sums of individual cross sections between the i^{th} lower and j^{th} upper Stark levels multiplied by their respective probability of occupancy in thermal equilibrium at temperature T.

$$\sigma_{EM}(\nu) = \sum_{ij} f_j \sigma_{ji}(\nu) \tag{2-18a}$$

$$\sigma_{AB}(\nu) = \sum_{ij} f_i \sigma_{ij}(\nu) \tag{2-18b}$$

where, the Boltzmann fractions f_i and f_j can be written as:

$$f_i = \frac{g_i e^{-E_i/kT}}{\sum_m g_m e^{-E_m/kT}} = \frac{g_i}{Z_{gnd}} e^{-E_i/kT} \qquad (2\text{-}19a)$$

$$f_j = \frac{g_j e^{-E_j/kT}}{\sum_m g_m e^{-E_m/kT}} = \frac{g_j}{Z_{gnd}} e^{-E_j/kT} \qquad (2\text{-}19b)$$

where Z_{gnd}, Z_{exc} are the partition functions of the ground, excited states respectively.

Figure 2-3 shows the Stark levels of a ground and excited state. A *zero-line energy* E_{ZL} can be defined as the energy between the lowest Stark levels of the ground and excited manifolds. The energy difference between the lowest Stark level of the excited state and any given Stark level of the excited state can be written in terms of E_{ZL}, E_i, and the transition energy hν. From figure 2-3, clearly:

$$E_j = E_i + h\nu - E_{ZL} \qquad (2\text{-}20)$$

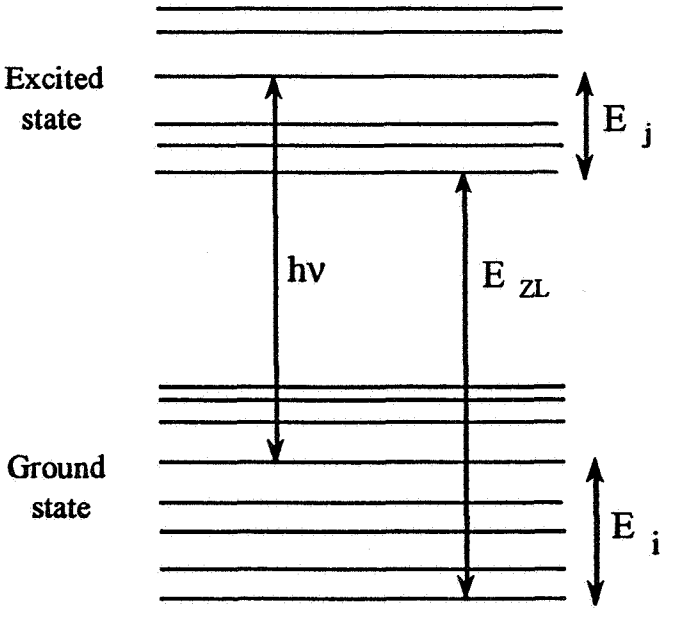

Figure 2-3 Stark Levels of Ground and Excited state

Equation 2-19b can now be written as

$$f_j = \frac{g_j}{Z_{exc}} e^{-E_i/kT} e^{-(E_{ZL}-h\nu)/kT} \tag{2-21}$$

Comparing this with eq. 2-19a, eq. 2-21 can be written in terms of f_i :

$$f_j = f_i \frac{g_j}{g_i} \cdot \frac{Z_{gnd}}{Z_{exc}} e^{-(E_{ZL}-h\nu)/kT} \tag{2-22}$$

Substituting this expression back into 2-18a, the emission cross section becomes:

$$\sigma_{EM}(\nu) = \frac{Z_{gnd}}{Z_{exc}} e^{-(E_{ZL}-h\nu)/kT} \sum_{ij} f_i \frac{g_j}{g_i} \sigma_{ji}(\nu) \tag{2-23}$$

Invoking reciprocity $\sigma_{ij} = (g_j/g_i)\sigma_{ji}$, the summation in eq. 2-23 becomes the absorption cross section. The final result is:

$$\sigma_{EM}(\nu) = \sigma_{AB}(\nu) \frac{Z_{gnd}}{Z_{exc}} e^{-(E_{ZL}-h\nu)/kT} \tag{2-24}$$

2.7 Energy Transfer

When a solid-state material containing optically active ions is exposed to a radiation source, electronic states can be excited if the ions absorb some of the photons in the radiation field. At some later time the electronic states de-excite through the emission of photons, which show up as light, or they can give up phonons to the crystal lattice, which show up as heat. This simple picture works well if the ions can be considered as isolated systems, which would be the case for very small ion concentrations where the

ions are well separated from each other. As the concentration of dopant ions is increased, however, the spacing between ions becomes small enough to allow the ions to interact with each other. It is this interaction between ions that is responsible for the transfer of energy from one excited ion to another. Energy transfer processes can result from various mechanisms. Photoconductivity occurs when the absorption of photons in a material creates electron-hole pairs that can migrate in a solid carrying both energy and charge. This type of mechanism is found mostly in electrical conductivity.

Another mechanism is *radiative energy transfer* in which a photon emitted by an excited ion is absorbed by another. This type of behavior is well understood in terms of the usual emission and absorption processes and will not be discussed here. However, the migration of radiative energy is important and does produce observable effects and cannot always be neglected. Generally this process can be taken into account by realizing that the radiative transfer of energy depends critically on the size of the solid-state sample and experimental geometry, so adjusting the experiment accordingly will minimize the effects.

The type of energy transfer that this thesis will be concerned with is *non-radiative energy transfer*, in which the excitation energy from an ion of one species (the *donor* or *sensitizer*) is transferred to an ion of another species (the *acceptor* or *activator*). This type of energy transfer can be viewed as a quantum mechanical resonance process involving the exchange of a virtual photon and can produce various effects on the luminescence of ions in solids (sensitized luminescence, fluorescence quenching, self-quenching, etc.) Non-radiative energy transfer can be a resonant one if the energy levels of the absorbing ions (donor) overlap the energy levels where emission occurs in the acceptors. The transfer can also be non-resonant if the phonons in the lattice are of sufficient energy to assist the transfer of energy by the creation or annihilation of phonons from the lattice such that the energy mismatch is compensated.

The mechanism of energy transfer between donor and acceptor was initially studied by Förster [Fo46,Fo48] and Dexter [De53] for the multipole and exchange interactions. The Hamiltonian describing the coupling between the electrons of the donor (D) and the electrons of the acceptor (A) due to the Coulomb interaction is:

$$H_{DA} = \frac{1}{\kappa}\sum_{i,j}^{N}\frac{e^2}{|\vec{r}_i - \vec{r}_j|} \tag{2-25}$$

where κ is the dielectric constant and i and j are the electrons of the donor and acceptor respectively. This is the Van der Waals' interaction between ions in solution or solid. The initial and final states of the system can be described by a superposition of properly symmetrized single ion states. Förster calculated the transition rate using the Fermi's Golden Rule:

$$w_{DA}(E) = \frac{2\pi}{\hbar}|\langle\Psi_i|H_{DA}|\Psi_f\rangle|^2\rho(E) \tag{2-26}$$

The Coulomb Hamiltonian in eq. 2-25 can be expanded in a Taylor series about the vector representing the separation between the donor and acceptor. This leads to an expression for the transition rate as a sum of multipole interactions:

$$w_{DA} = \frac{C^{DD}}{R^6} + \frac{C^{DQ}}{R^8} + \frac{C^{QQ}}{R^{10}} + \cdots \tag{2-27}$$

where C^{DD}, C^{DQ}, and C^{QQ} represents the strength of the dipole-dipole, dipole-quadrupole, and quadrupole-quadrupole interactions respectively. R is the distance separating the donor and acceptor ions. A large amount of experimental work based on the Förster-

Dexter model has been done in the past few decades. In particular, the Förster-Dexter theory has been used to determine which multipolar terms dominate in energy transfer and luminescence quenching processes, and to calculate values for the respective interaction parameters (C^{DD} ,C^{DQ} ,C^{QQ}, etc.).

To extract relevant information about the microscopic interactions between acceptor and donor ions, a statistical analysis of the donor-acceptor distances in real, macroscopic crystals is necessary to account for the distribution of environments seen by different donor ions. Such an approach was originally taken by Förster [Fo49] and later generalized by Inokuti and Hirayama [InHi65]. The general expression of the donor decay for any order of multipole interaction derived in [InHi65] can be written as:

$$n_D(t) = n_0(t)\exp\left[-\frac{t}{\tau} - \frac{4}{3}\pi\Gamma\left(1-\frac{3}{q}\right)N_A(C_{DA}t)^{3/q}\right] \qquad (2\text{-}28)$$

where τ is the lifetime of the donor in the absence of transfer, $\Gamma(x)$ is the gamma function, N_A is the acceptor ion density, C_{DA} is an "*interaction microparameter*" for the donor to acceptor transfer, and q is the order of the multipole process (q=6 for dipole-dipole, q=8 for dipole-quadrupole, and q=10 for quadrupole-quadrupole). In practice, this relation can be used to determine the order of the multipole process by fitting it with the experimental data. In reality, however, the similarity of the decay functions for q = 6, 8, 10 and the uncertainty inherent in the experimental data makes this approach inconclusive. Unless it is known that electric dipole transitions are forbidden, experimental decay data are usually fit with q=6 assuming a prevalent dipole-dipole process.

There have been some objections to the applicability of eq. 2-28 in the interpretation of energy transfer. Grant [Gr71], in a paper that approached the macroscopic case of energy transfer with the use of rate equations, showed that the

concentration dependence of energy transfer is a result of the assumption that transfer occurs primarily between nearest neighbors. Grant points out that it is not clear why this is justifiable in principle, but probably does not introduce much of an error for small concentrations. Fong and Diestler [FoDi71], on statistical considerations, came to the conclusion that the dependence of transfer probability on concentration does not reflect multipole behavior, but is due to many body processes that reflect the number of ions participating in the process. More recently, Rotman [Ro89] has shown evidence for the correlated placement of ions in Nd:YAG, where energy transfer takes place between nonuniformly distributed ions in which a donor has an enhanced or excluded number of acceptors to interact with.

Despite the objections made to it, eq. 2-28 has been found to describe the decay of donor ions quite well in many systems with low donor ion concentration. When the donor ion concentration is increased, the distance between donor ions decreases and it becomes more likely for excitation to migrate or hop to a near neighbor. Excitation energy may then be able to migrate among the donor ions before it is passed to an acceptor ion. With diffusion, excitation energy is transferred to an acceptor ion more efficiently by diffusing through the donors to interact with an acceptor at a much shorter distance, rather than interacting over a larger distance. The process of diffusion also leads to spatial equilibrium among the donor ions by averaging out the variation in environment as seen by the donors. For high concentrations of donors, the diffusion rate will be much faster than the D->A transfer rate and the average donor-acceptor interaction distance will be roughly the same over the entire system. This results in D->A transfer rates that are effectively the same over the entire ensemble of ions. The rate limiting step for the donor relaxation then becomes either the donor-acceptor transfer rate or the acceptor relaxation rate. The outcome is an exponential decay rather than the $t^{1/2}$ exhibited by eq. 2-28. This is the case

for fast diffusion and is ideal for a treatment with rate equations where the spatial variations in donor environments are not an inherent property of rate equations.

Experimentally, it is very common to see decays that exhibit non-exponential behavior at early times and then a longer exponential tail. For moderate concentrations the rate of energy diffusion within the donor system may not be sufficient to maintain a uniform excitation of donors. In this case, certain donor sites will interact with acceptors over a larger distance than others that see enhanced rates of interaction due to diffusion. The decay of the donor system is then composed of competing processes. This is the case of diffusion-limited relaxation and has been treated by Yokota and Tanimoto [YoTa65]. They solved the diffusion equation of the form:

$$\frac{dn}{dt} = -D\nabla^2 n - \frac{n}{\tau} - n\sum_i \frac{C_{DA}}{|\vec{r}-\vec{r}_i|} \qquad (2\text{-}29)$$

where the first term is the rate of change due to diffusion with diffusion constant D, the second term is the natural lifetime (radiative + nonradiative) in the absence of cross relaxation and diffusion, and the third term is the interaction with i acceptors at position r_i, with the dipole-dipole interaction parameter C_{DA}. Using the method of Padé approximants they found the following solution:

$$n(t) = n(0)\exp\left[-\frac{t}{\tau} - bt^{1/2}\left(\frac{1+10.87x+15.5x^2}{1+8.743x}\right)^{3/4}\right] \qquad (2\text{-}30)$$

where $b = \frac{4}{3}\pi^{3/2} N_A \sqrt{C_{DA} t}$ and $x = DC_{DA}^{-1/3} t^{2/3}$

When D->0, eq. 2-30 reduces to eq. 2-28 for a dipole-dipole case (q = 6).

At early times, $t<<D^{-3/2}C_{DA}^{1/2}$, the diffusion is unimportant and the decay is non-exponential as in eq. 2-28. As $t->\infty$, the donors will decay exponentially at a rate determined by the migration. As the migration becomes faster the boundary between these two types of behavior shifts to shorter times until the decay appears to be purely exponential. This changing time dependent decay is a distinguishing characteristic of diffusion limited relaxation. At very long times, the fluorescence decay can be written as [YoTa67]:

$$n(t) = n(0)\exp\left[-\frac{t}{\tau} - \frac{t}{\tau_D}\right] \tag{2-31}$$

where,

$$\frac{1}{\tau_D} = 0.51\left(4\pi N_A C_{DA}^{1/4} D^{3/4}\right) \tag{2-32}$$

So, at later times in the decay stage, the donors with accessible acceptor environments have all transferred their energy to the acceptors. Further decay is limited until migration brings the donor excitation close enough to some acceptors to facilitate transfer. The decay is then seen to be limited by the diffusion rate. It is exponential and proceeds at the rate given by eq. 2-32. This regime of the decay is most easily investigated because analyzing decay curves at longer times is easier since they become exponential and generally comprises a substantial portion of the decay profile.

References to Chapter 2

[Ca68a] W.T. Carnall, P.R. Fields, K. Rajnak,"Electronic energy levels in the trivalent lanthanide ions I. Pr^{3+} ,Nd^{3+} ,Pm^{3+} ,Sm^{3+} ,Dy^{3+} Ho^{3+}, Er^{3+} and Tm^{3+}," J. Chem. Phys. **49**, 4424 (1968)

[Ca68b] W.T. Carnall, P.R. Fields, K. Rajnak,"Spectral Intensities of the trivalent lanthanides and actinides in solution II. Pm^{3+} ,Sm^{3+} ,Eu^{3+}, Gd^{3+} ,Tb^{3+} Dy^{3+}, and Ho^{3+}," J. Chem. Phys. **49**, 4412 (1968)

[De53] D.L. Dexter, "A Theory of Sensitized Luminescence in Solids," J. Chem. Phys. **21**, 836 (1953)

[Fo46] Th. Förster, Naturwissenschaften **33**, 166 (1946)

[Fo48] Th. Förster, Ann. Phys. **21**, 55 (1948)

[FoDi71] F.K. Fong, D.J. Diestler, "Many-Body Processes in Nonradiative Energy Transfer between Ions in Crystals," J. Chem. Phys. **56**, 2875 (1971)

[Gr71] W.J.C. Grant, "Role of Rate Equations in the Theory of Luminescent Energy Transfer," Phys. Rev. **B4**, 648 (1971)

[InHi65] M. Inokuti, F. Hirayama, "Influence of Energy Transfer by the Exchange Mechanism on Donor Luminescence," J. Chem. Phys **43**, 1978 (1965)

[Ju62] B.R. Judd,"Optical intensities of rare-earth ions," Phys. Rev. **127**, 750 (1962)

[Mc64] D.E. McCumber, "Einstein relations connecting broadband emission and absorption spectra," Phys. Rev. **136**, A954-A957 (1964)

[Of62] G.S. Ofelt,"Intensities of crystal spectra of rare-earth ions," J. Chem. Phys. **37**, 511 (1962)

[Pa92] S. Payne, L.L. Chase, L.K. Smith, W.L. Kway and W.F. Krupke,"Infrared cross-section measurements for crystals doped with Er^{3+} ,Tm^{3+} and Ho^{3+}," IEEE J. Quantum Elec. **28**, 11, 2619-2629 (1992)

[Ru56] W.A Runciman, Phil. Mag. (8) **1**, 1075 (1956)

[Ro89] S.R. Rotman, "Nonradiative energy transfer in Nd:YAG - evidence for the correlated placement of ions,"Appl. Phys. Lett. **54**, 2053 (1989)

[Va37] J.H. Van Vleck,"The puzzle of rare-earth spectra in solids," J. Phys. Chem. **41**, 67-80 (1937)

[YoTa67] M. Yokota and O. Tanimoto,"Effects of diffusion on energy transfer by resonance," J. Phys. Soc. Japan **22**, 779-784 (1967)

CHAPTER 3
$LiYF_4$ (YLF) as Host Lattice

God has put a secret art into the forces of Nature so as to enable it to fashion itself out of chaos into a perfect world system.

Immanuel Kant
Universal Natural History and Theory of the Heavens

3.1 Structure of Solids: the Crystal Lattice

A crystal can be described as a collection of atoms or molecules arranged in a periodic pattern. This periodic pattern extends over an interval that is large compared to the unit of periodicity, the so-called *unit cell*. The structure of any crystal can be described by defining a set of basis vectors along the crystallographic axes. In this way a lattice can be generated from a given point by repeated application of the three basis vectors, $\hat{x}$ with magnitude a, $\hat{y}$ with magnitude b, and $\hat{z}$ with magnitude c. The points of the lattice defined in this way do not have to correspond to actual positions of atoms, but are meant to indicate that the environment about any one lattice point is identical to that around any other lattice point. The position of the point lattice can be chosen so that each point corresponds with the positions of one of the kinds of atoms which make up the crystal. Once the placement and number of atoms within a unit cell are known, the entire structure of the crystal is determined by translational periodicity.

The entire problem of determining the structure of a crystal is reduced to finding the positions of a relatively few number of atoms within a unit cell. The entire crystal is then visualized as made up of multiple unit cells, sharing edges, corners or faces. Crystallographic axes are chosen in a way that shows the symmetry of the lattice.

3.2 Symmetry in Crystal Systems

By considering the underlying symmetry of crystal systems, the classification and detailed description of various types of crystals is greatly facilitated. The point lattice system described above serves as a basis of classification of crystals into one of seven systems (Triclinic, Monoclinic, Orthorhombic, Tetragonal, Cubic, Hexagonal, and Rhombohedral). This classification can be extended by considering unit cells that contain lattice points in addition to those at the corners. For example, consider a simple cube. This is the primitive cubic. A cube with a lattice point at its center is a body-centered cubic system, and a cube with a lattice point in the center of each face of the cube is a face centered cubic system. Each of these classifications is known as a *Bravais lattice*, of which there are fourteen. The reader is referred to a book on solid state physics [AsMe76] for more details.

The point here is that an examination of the characteristics of well-formed crystals may reveal certain elements of symmetry that can be exploited with the powerful methods of group theory. An object is said to possess symmetry if an operation such as rotation, or reflection about a particular axis transforms the object into a configuration indistinguishable from the original. It turns out that there are 32 crystal classes that can be obtained by considering the symmetry operations that transform the crystal lattice to its original configuration with one of the lattice points remaining fixed. These are known as the 32 point groups since they refer to the symmetry about a single lattice site. Further, translatory movements of the lattice in a given direction and subsequent symmetry considerations of the new arrays obtained lead to a set of 230 *space groups*. All crystals must belong to one of the 230 space groups. Knowledge of the presence of symmetry within the unit cell, and X-ray diffraction methods are useful in determining the number of atoms and their relative positions within a given crystal lattice.

3.3 The Structure of $LiYF_4$

Lithium Yttrium Fluoride, $LiYF_4$ (YLF) is a simple fluoride crystal with a tetragonal scheelite structure (space group $C_{4h}^6 - I4_1/a$, number 88) [Th61], [Sh69].The crystal structure of YLF is pictured in figure 3-1.

Rare earth impurities introduced into YLF replace the Yttrium ions substitutionally. The point group symmetry at the site of the Yttrium ions is S_4. This means that while the overall symmetry of YLF is tetragonal, the symmetry at the site of the ions in the crystal is S_4, so called because there exists a 4-fold rotation-reflection axis. A 4-fold rotation-reflection axis is one in which a rotation about it equal to $\pi/2$ followed by a reflection in the plane perpendicular to the axis produces no change. This seemingly technical detail is very important in determining selection rules for dipole-dipole transitions in laser crystals.

It can be seen from figure 3-1 that the crystallographic directions in YLF are not equivalent. There exists two equivalent directions (the a-axes), and one independent of the other two (the c-axis). Crystals that exhibit this property are called *anisotropic*. YLF is an example of a uniaxial anisotropic crystal, as opposed to a biaxial crystal that has three independent directions.

Trivalent rare-earth ions replace, substitutionally, Yttrium (Y^{3+}) ions in YLF with little change in lattice parameters since rare-earth ions and Yttrium have nearly the same atomic radii. The lattice constants for YLF have been measured from x-ray diffraction data [BlSa79], where they are reported to be a = 5.166 Å and c = 10.733 Å.

Using these lattice constants, table 3-1 shows the calculated distances from reference ion 0 (see figure 3-1) to neighboring Yttrium ions, and the corresponding number of nearest neighbors of types 1,2,3 and 4.

Table 3-1 Nearest Neighbor Distances in $LiYF_4$ (YLF)

Ion Type	Distance from Ion 0 (Å)	# nearest neighbors
1	3.7247	4
2	5.1668	4
3	6.3694	8
4	6.9420	8
2	7.3069	4
1	8.2015	4
2	8.4541	4
3	9.6934	8
4	9.7744	16
2	9.9080	8

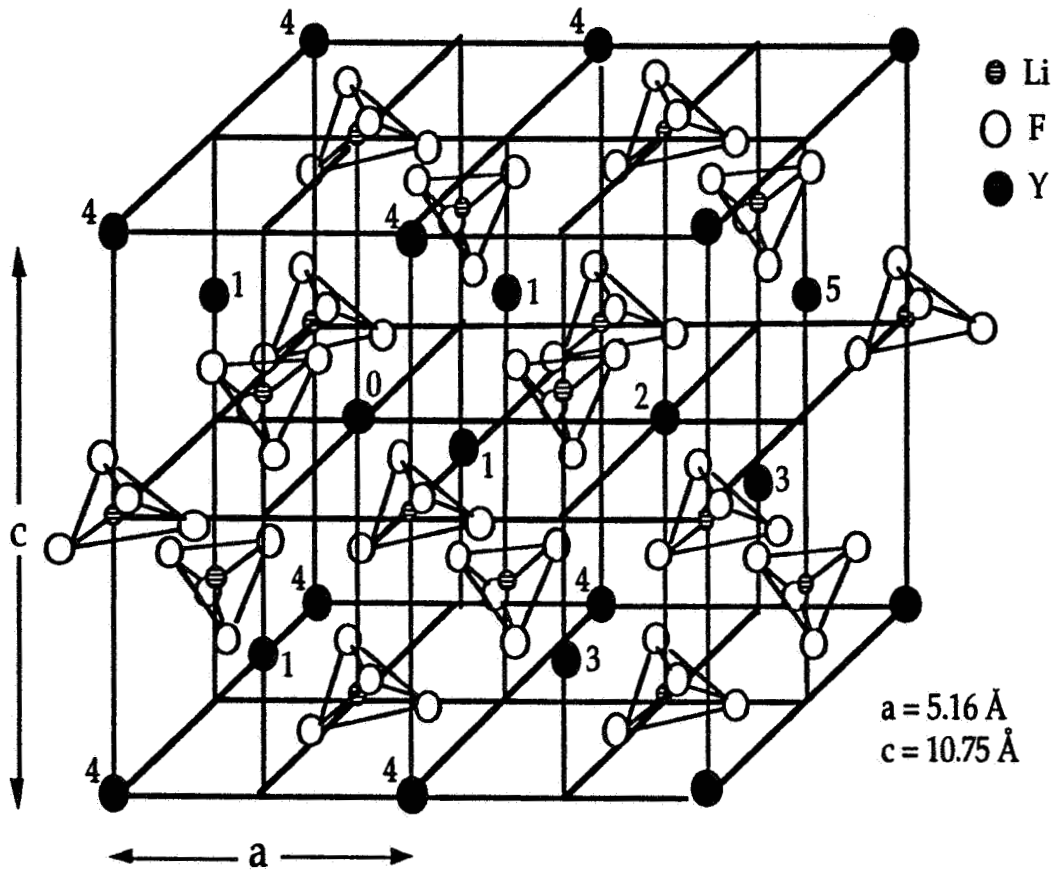

Figure 3-1 Crystal Structure of $LiYF_4$ (YLF)

3.4 Index of Refraction of $LiYF_4$

The index of refraction of YLF crystals has been measured previously [CaLi75] for both ordinary and extraordinary waves in the wavelength range 0.225μm to 2.6μm. The data reported in this reference is listed in table 3-2 and presented graphically in figure 3-2. The data in table 3-2 has been fit by the method of least squares to the Sellmeier equation:

$$n^2 = A + \frac{B\lambda^2}{(\lambda^2 - C)} + \frac{D\lambda^2}{(\lambda^2 - E)} \qquad (3\text{-}1)$$

The Sellmeier coefficients were found to be:

ordinary (n_O): A=1.35272, B=0.70757, C=0.00893, D=0.49161, E=124.992

extraordinary (n_e): A=1.35743, B=0.80225, C=0.00916, D=0.59253, E=145.892

The units on C, and E are μm^2, while A, B and D are unitless. The root mean square deviation for the fit of the refractive index data to eq. 3-1 was $\sigma = 0.000040$. The temperature dependence of the refractive index of YLF in the visible region of the spectrum has also been done previously [BaGe80], where it was found that n decreases by small amounts at lower temperatures. The small negative variation of the refractive index tends to minimize thermal-focusing effects in solid-state laser rods, which can cause degradation of laser beam quality by reducing the TEMoo mode radius, allowing higher-order modes to oscillate.

It should be pointed out that the terms ordinary and extraordinary index of refraction refer to the direction of the propagating electric field with respect to the c-axis of the crystal. Ordinary refers to an electric field perpendicular to the c-axis, and extraordinary refers to an electric field parallel to the c-axis.

Table 3-2 Refractive Index Values in $LiYF_4$ (YLF)

Wavelength (μm)	n_e	n_o
2.600	1.4602	1.4381
2.400	1.4617	1.4397
2.200	1.4632	1.4411
2.000	1.4645	1.4424
1.800	1.4658	1.4437
1.600	1.4670	1.4449
1.400	1.4681	1.4460
1.200	1.4693	1.4471
1.000	1.4708	1.4485
0.900	1.4716	1.4492
0.800	1.4726	1.4502
0.700	1.4741	1.4516
0.600	1.4962	1.4502
0.500	1.4796	1.4567
0.450	1.4822	1.4590
0.400	1.4822	1.4624
0.350	1.4913	1.4674
0.300	1.5001	1.4754
0.250	1.5156	1.4895
0.225	1.5287	1.5014

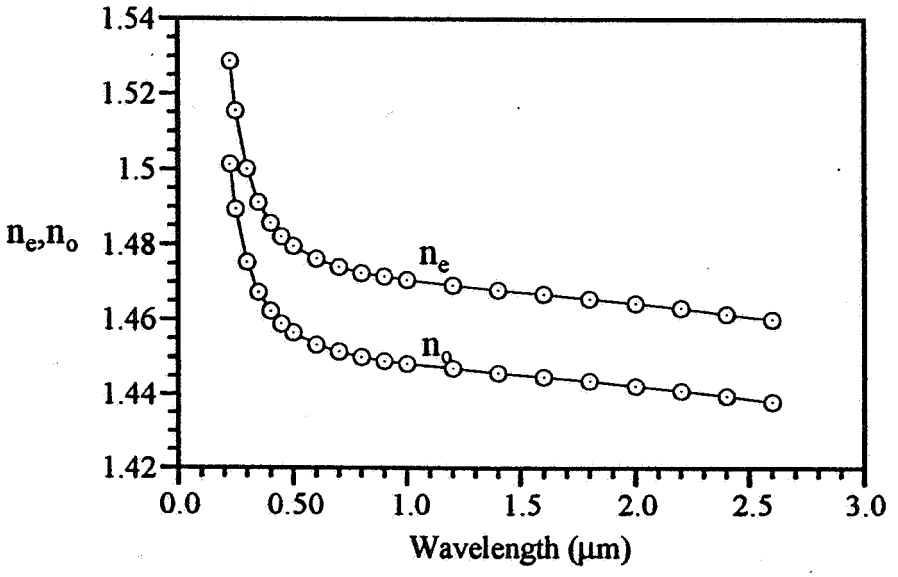

Figure 3-2 Refractive Index vs. Wavelength in $LiYF_4$ (YLF)

3.5 Mechanical Properties of $LiYF_4$

The mechanical properties of YLF have been taken from various sources in the literature. They are listed below in table 3-3

Table 3-3 Mechanical Properties of $LiYF_4$ (YLF)

Young's modulus	$B = 8.0 \times 10^{10}$ N/m^2	ref. [BlSa79]
Volume compressibility	$\beta_v = 12.5 \times 10^{-12}$ N/m^2	ref. [BlSa79]
Linear compressibility	$\beta_z = 3.4 \times 10^{-12}$ N/m^2 $\beta_{xy} = 3.4 \times 10^{-12}$ N/m^2	ref. [BlSa79]
Density	$\rho = 3.99$ gm/cm^3	ref. [BlSa79]
Poisson's ratio	$\nu = 0.33$	ref. [Ko92]
Strength	3.3×10^{-7} N/m^2	ref. [Ko92]
Hardness (Knoop)	260-325 kg/mm^2	ref. [ChFo73]
Hardness (Mohs)	4 -5	ref. [Ko92]

3.6 Thermal Properties of $LiYF_4$

The thermal properties have also been taken from various sources in the literature. They appear in table 3-4. It should be mentioned that the phonon energies for YLF in table 3-4 represent the high frequency energies of the phonons of the effective modes involved in multiphonon nonradiative transitions. The range of phonons observed from Raman spectra [MiRa70], [CaRa75] is 140 - 560 cm^{-1}, but due to their small mass the Lithium atoms are expected to vibrate at their highest frequencies for a given mode. The mode assignment labels for the phonons given in the above references are for C_{4h} symmetry not S_4. The phonon modes and their corresponding highest frequency phonons are given in table 3-5.

Table 3-4 Thermal Properties of $LiYF_4$ (YLF)

Thermal Conductivity	$k = 1.5 \times 10^{-2}$ cal./cm-sec-°C	ref. [ChFo73]
Coeff. of Linear expansion (0-100°C), ΔT=100°C	a-axis: $a = 13.8 \times 10^{-6}$ °C^{-1} c-axis: $a = 9.0 \times 10^{-6}$ °C^{-1}	ref. [ChFo73]
Melting Point	$T_m = 825$°C	ref. [Ko92]
Debye Energy	$\theta_D = 279$ cm^{-1}	ref. [BlSa79]
Phonon Energy	$E_p = 424 - 566$ cm^{-1}	ref. [MiRa70]
dn_o/dt	-0.54×10^{-6} (@435.8 nm) -0.67×10^{-6} (@546.1 nm) -0.91×10^{-6} (@578.0 nm)	ref. [BaGe80]
dn_e/dt	-2.44×10^{-6} (@435.8 nm) -2.30×10^{-6} (@546.1 nm) -2.86×10^{-6} (@578.0 nm)	ref. [BaGe80]

Table 3-5 Phonon Modes and Phonon Energies in $LiYF_4$ (YLF)

Mode	Highest frequency phonon
A_g	425 cm^{-1}
B_g	427 cm^{-1}
E_g	446 cm^{-1}
A_u	490 cm^{-1}
E_u	566 cm^{-1}

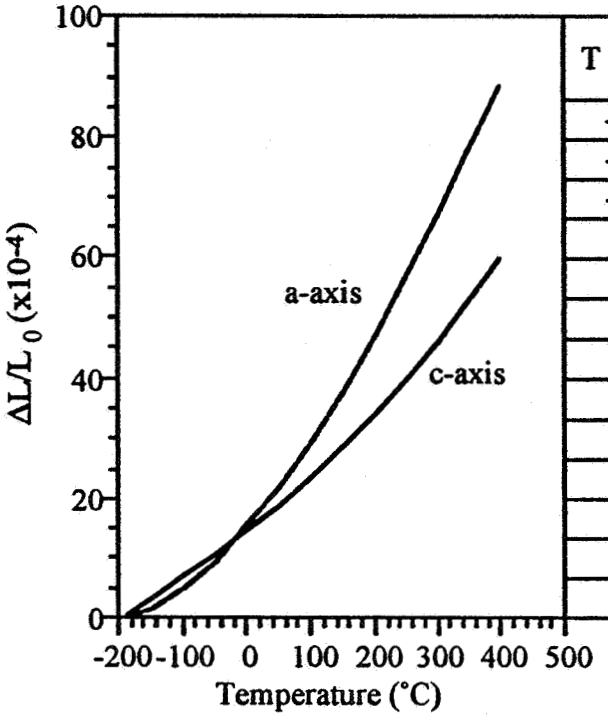

T (°C)	a-axis $\Delta l/l_0 x10^{-4}$	c-axis $\Delta l/l_0 x10^{-4}$
-196	0	0
-150	1.5	3.3
-100	4.8	6.9
-50	9.5	10.6
0	15.3	14.5
50	21.8	18.8
100	29.1	23.5
150	37.8	28.7
200	47.1	34.1
250	57.0	39.8
300	67.5	46.1
350	78.0	52.8
400	88.5	59.6

Figure 3-3 Linear Thermal Expansion of YLF

Figure 3-3 shows a graph of the linear thermal expansion of YLF. The coefficient of linear expansion can be calculated from the data in table 3-3. It is defined as:

$$\alpha = \frac{1}{\Delta T} \cdot \frac{\Delta L}{L_o} \tag{3-2}$$

The coefficient of linear expansion for the a-axis and c-axis in YLF appears in table 3-4 for a temperature range $\Delta T = 100$ °C.

References to Chapter 3

[AsMe76] N.W. Ashcroft, ND. Mermin: Solid State Physics (W.B. Saunders Company) 1976

[BaGe80] N.P. Barnes, D.S.Gettemy,"Temperature variation of the refractive indices of Yttrium Lithium Fluoride," J. Opt. Soc. Am. **70**, 10, 1244 (1980)

[BlSa79] P. Blanchfield, G.A. Saunders, "The elastic constants and acoustic symmetry of $LiYF_4$," J. Phys. C: Solid State Phys. **12**, 4673-4689 (1979)

[CaLi75] D.E. Castleberry, A. Linz, "Measurement of the refractive indices of $LiYF_4$," Applied Optics **14**, 9, 2056 (1975)

[CaRa75] H.H. Caspers, H.E. Rast, "Electronic and vibronic spectra of Pr^{3+} in $LiYF_4$," J. Lumin. **10**, 347-369 (1975)

[ChFo73] E.P. Chiklis et al.,"Development of multiply sensitized Ho:YLF as a laser material," Tech. Rept. ECOM-0013-F (1973)

[GaHa68] D. Gabbe, A.L. Harmer,"Scheelite structure fluorides: The growth of pure and rare earth doped $LiYF_4$,"J. Crystal Growth **3**, 4,544 (1968)

[Ko92] W. Koechner: Solid-State Engineering, 3rd ed., (Springer-Verlag 1992) p.61

[MiRa70] S.A. Miller, H.E. Rast, H.H. Caspers,"Lattice vibrations of $LiYF_4$," J. Chem Phys. **52**, 8, 4172-4175(1970)

[Sh69] W.A. Shand, "Single crystal growth and some properties of $LiYF_4$," J. Crystal Growth **5**, 143-146 (1969)

[Th61] R.E. Thoma et al., J. Phys. Chem. **65**, 1096 (1961)

CHAPTER 4
Experimental Apparatus and Samples

In considering the intent for which a clock has been designed, I can say that it is false to its nature when it does not correctly indicate the time.

René Descartes
Meditations on First Philosophy

4.1 Absorption Measurements

Absorption measurements were made with a Perkin-Elmer Lambda9 UV/Vis/NIR Spectrophotometer. The Lambda9 incorporates two juxtaposed monochromators. Each one of them is equipped with two large gratings, a photomultiplier and, a PbS (lead sulfide) detector. The range of wavelengths extended from 190-3200 nm. The schematic of the optical system is shown in figure 4-1.

The excitation sources included a deuterium lamp for the UV range and a Tungsten-Halogen lamp for the visual and infrared regions. The instrument resolution was .05 nm due to limitations on the data acquisition software. Careful selection of various control parameters on the Lambda9 allowed a compromise to be made between spectral resolution and signal to noise ratio.

A double depolarizer/polarizer assembly was used since the crystals analyzed in this study were uniaxial. Uniaxial crystals exhibit varying degrees of transmission for different orientations and polarizations. The double depolarizer/polarizer assembly is a complete sample compartment that fits into the Lambda9 as one unit. The depolarizer mounts in the optical path between the entrance slit and the crystal. This depolarizer was necessary since light dispersed from a grating is partially polarized. The depolarization effect, however, is not a true depolarization, but a statistical mixing of all polarizations

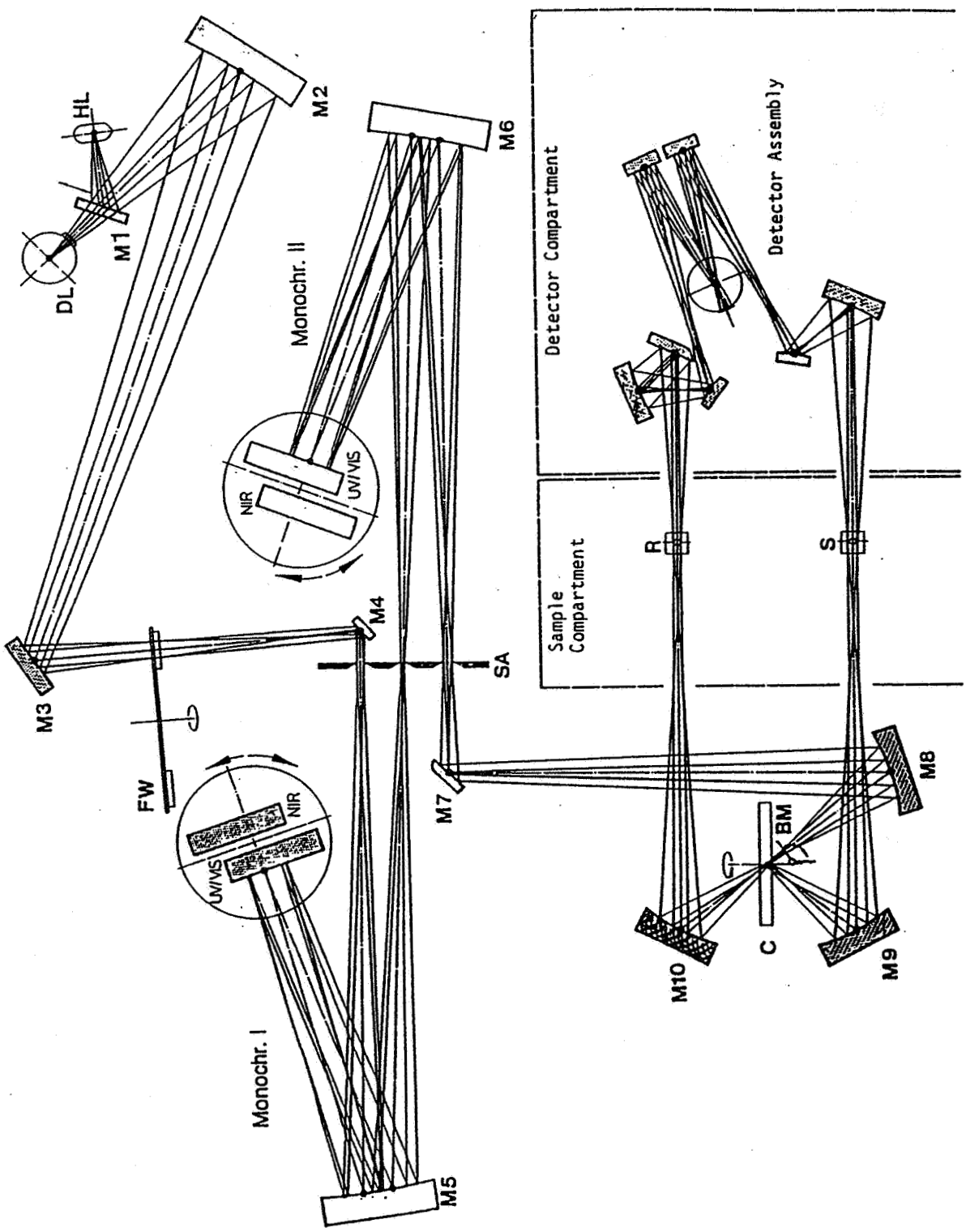

Figure 4-1 Schematic of Absorption Spectrophotometer Optical System

within the cross-section of the radiation beam. The double polarizer mounts between the crystal and the exit slit leading to the detector. It consists of two wedge-shaped Glan-Thompson prisms that can be rotated between 0 and 180 degrees by a mechanical drive located outside the sample compartment.

The crystals were placed in the sample compartment with the c-axis of the crystal oriented in a vertical direction perpendicular to the optical path of the excitation beam. By orienting the mechanical drive to 0°, the π-polarized (electric field of the optical beam parallel to the c-axis) transmission spectra was measured. By orienting the mechanical drive to 90° the σ-polarized (electric field of the optical beam perpendicular to the c-axis) transmission spectra was measured. See figure 4-2 for orientation configurations.

Due to the optical materials used in the depolarizer/polarizer the measurable wavelength range was 300-2600 nm. The transmission spectra were corrected for Fresnel losses at the crystal faces and converted to absorption spectra.

4.2 Continuous Luminescence Measurements

The apparatus used for continuous luminescence measurements consisted of an excitation system, a collection system, a detection/ amplification system, and a processing/recording system (see figure 4-3 for details).

4.2.1 The Excitation System

The excitation source used was a SONY model SLD 303XT-1 GaAlAs double-hetero laser diode. The laser diode assembly consisted of the photodiode, which had a thin active GaAlAs layer .05μm thick, a built in TE cooler for wavelength tuning, and a thermistor for temperature monitoring. The current for the lasers operation was provided by a Spectra Diode Labs SDL800 Laser Driver. The SDL800 had a current controller that

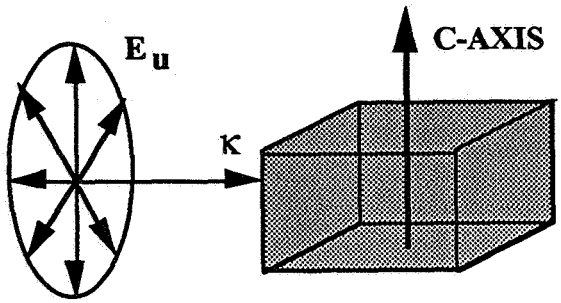

In the absorption measurements, the optical beam is depolarized before passing through the crystal resulting in a randomly directed E-field vector. Polarization select is made by orienting a polarizer ir the desired direction after the bea is attenuated upon passage throug the crystal. See below.

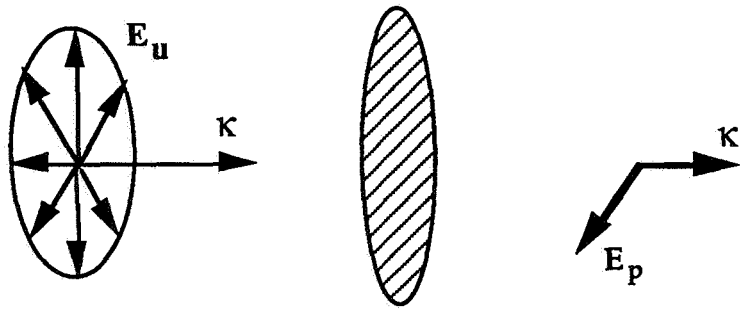

After the beam passes through a horizontal polarizer, the vertical component of the E-field is eliminated. The measured field is denoted as σ-polarized. (Note that **E** is perpendicular to the c-axis.)

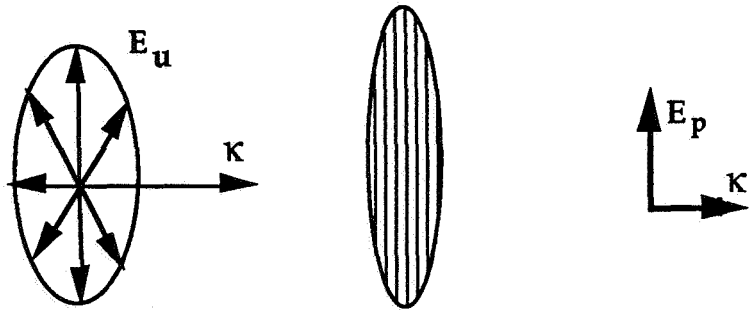

After the beam passes through a vertical polarizer, the horizontal component of the E-field is eliminated. The measured field is denoted as π-polarized. (Note that **E** is parallel to the c-axis.)

Figure 4-2 Polarized Absorption Measurements

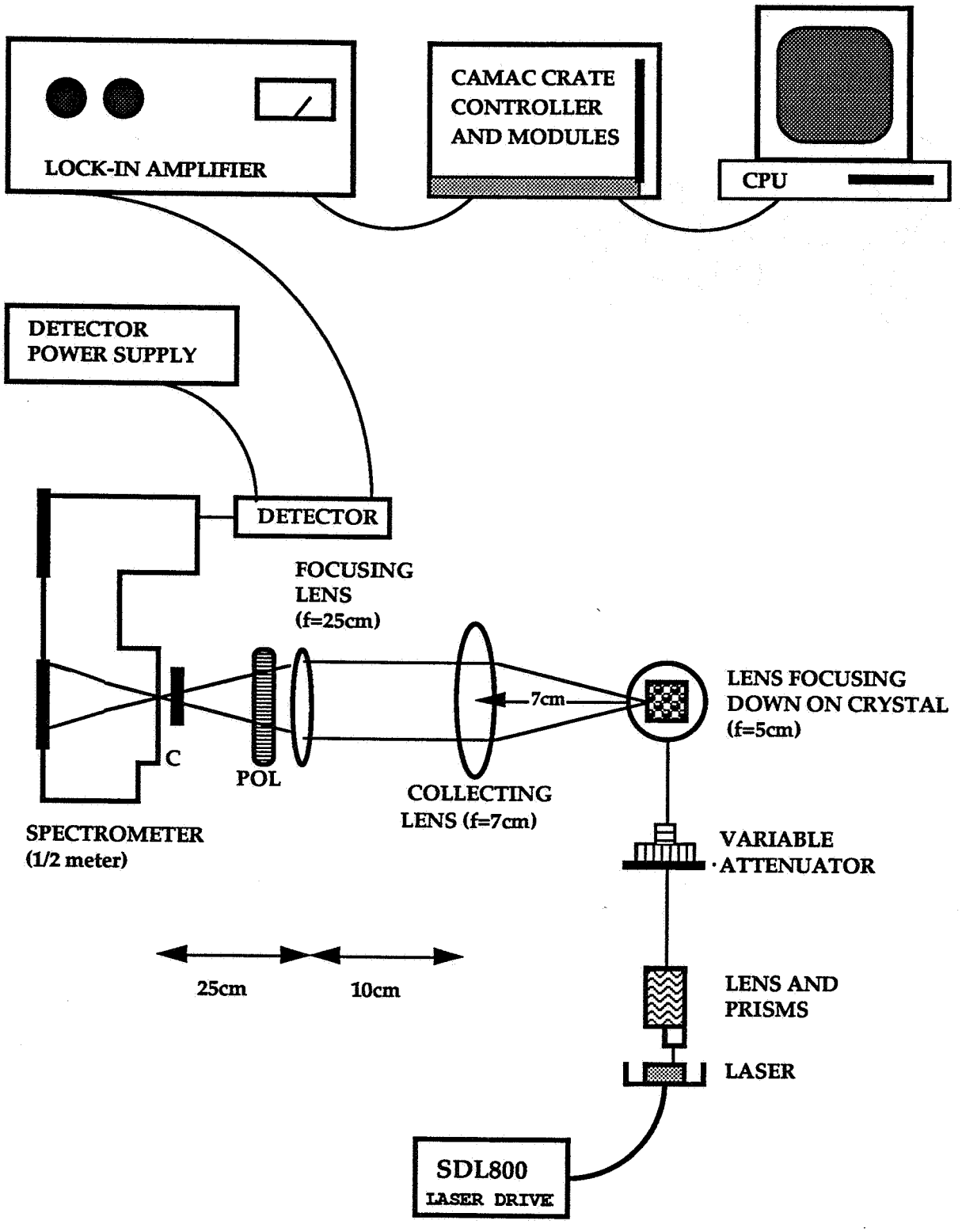

Figure 4-3 Continuous Luminescence Apparatus

was limited to 1 ampere, and a temperature controller to tune the wavelength in the range 785 ± 15 nm. The current limit was set to 980 mA and the setpoint temperature to 6.8°C for an operating wavelength of 785.5 nm and an output power of 350mW.

Laser diode beams are highly divergent, making it difficult to collect and collimate the beam. To overcome this an 8mm Melles-Griot lens was used in conjunction with an anamorphic prism pair to collect and collimate the laser radiation into a circular region with a 5mm diameter. The loss of diode light was kept at a minimum by using coated optics and by careful positioning of the lens/prism unit. This circular beam was then reflected from a mirror and focused onto the crystal with a 5 cm plano-convex calcium fluoride lens. This produced an excitation along the c-axis of the crystal after focus to a spot size measured to be 140μm x 260μm in diameter.

4.2.2 Optical Collection System

The luminescence from the crystal was collected by a 6 cm diameter (f=7cm) convex lens placed at a distance of 7 cm from the crystal to form a collimated beam, which was then focused by a 25 cm focal length lens onto the entrance slit of the spectrometer.

The spectrometer used for wavelength selection of the luminescence signal was a 0.5 meter McPherson model 216.5. The gratings used were a 1200 grooves/mm blazed @500 nm for measurements in the visible (300-850 nm), and a 600 grooves/mm blazed @1.6μm for measurements in the IR (850-2100 nm). Power dependence of these measurements was done by placing a variable attenuator between the laser and reflecting mirror. Polarization measurements were done by placing a polarizer between the focusing lens and the entrance slit of the spectrometer. The entrance and exit slits were kept at 50μm in the visible and 500μm in the infrared. Figure 4-4 illustrates the polarized emission measurements.

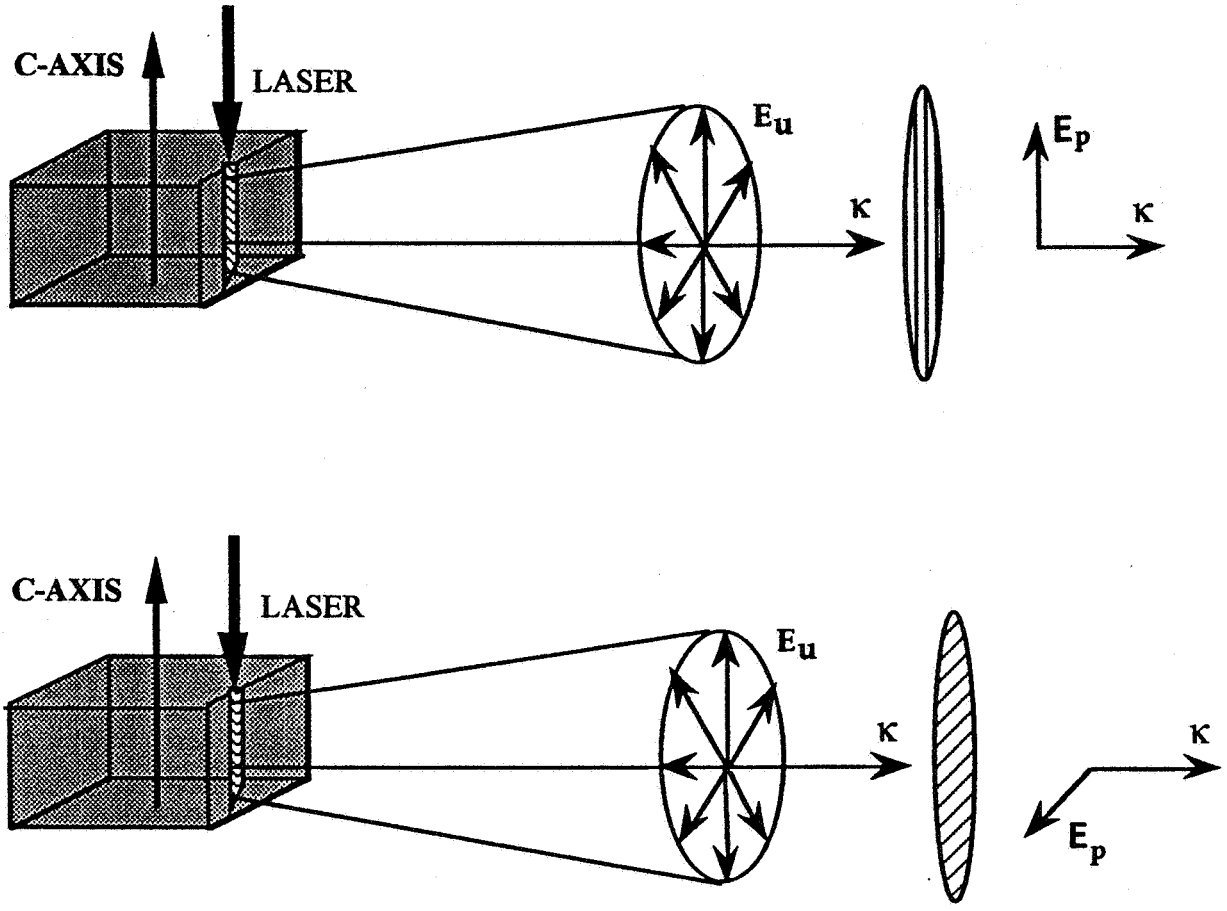

In the case of polarized emission studies pictured above, the laser pumps along the c-axis of the crystal ,exciting optically active ions in the crystal. While the laser is a coherent source with a definite polarization, the luminescence from the crystal is not. The incoherent radiation produced by spontaneous emission is unpolarized and spreads in all directions. Polarization selection is made by orienting a polarizer in the path of the collected luminescencse. The top diagram is an example of π-polarization (E is parallel to the c-axis of the crystal.) The bottom diagram is an example of σ-polarization (E is perpendicular to the c-axis of the crystal.) It should be noted that the the important aspect is the direction of the polarized E-field, and the propagation vector κ relative to the c-axis.

Figure 4-4 Polarized Luminescence Measurements

4.2.3 Detection and Amplification System

The detectors used at the exit slit of the spectrometer were a Perkin-Elmer photomultiplier for visible wavelengths and an Electro-Optical Systems liquid nitrogen cooled Indium Antimonide detector for IR wavelengths.

Signal amplification was performed by a PAR (Princeton Applied Research) model HR-8 lock-in amplifier in conjunction with a PAR model 125 mechanical chopper. The high voltage supply used for the photomultiplier was an EMI Gencom model 3000R. A voltage of 1250V was used in this experiment. The IR detector was powered with two 6V batteries.

4.2.4 The Processing and Recording System

The analog signal from the lock-in amplifier was processed through connection to a DSP Technologies Crate System. The signals from the lock-in and chopper were transformed by passing them through a CAMAC module 1030 Amplifier. This provided the necessary voltage couplings (AC or DC), voltage offsets and signal attenuation for passage to a CAMAC module 2012 transient digitizer. The 2012 module sampled the analog signal and converted it to a digital number by sampling a given number of pre-trigger signals. The digital signal was then sent from the CAMAC module 6001 crate controller through an RS-232 connection to a Gateway 2000 computer system. A computer program was written to display the output data. Controls of the scanning parameters were entered at the keyboard and sent to the crate controller for initialization.

4.3 Pulsed Luminescence Measurements

Two laser sources were used for pulsed excitation measurements. Both of these

lasers were pumped with an Nd:YAG laser. The first was a 532 nm Nd:YAG pumped Ti:Al_2O_3 (Titanium Sapphire). The optical schematic of this laser is shown in figure 4-5. The Ti:Al_2O_3 laser was tunable over the wavelength range of 600 - 900 nm. The tuning was achieved with a prism in the laser cavity. When the laser was tuned to 780 nm the observed pulse duration was <100 ns and the peak output power was 25 mJ. The second laser source was a 1.33 μm Nd:YAG pumped $CoMgF_2$ (Cobalt Magnesium Fluoride). The optical schematic of this laser is shown in figure 4-6. The $CoMgF_2$ laser was tunable over the wavelength range 1.7 - 2.1 μm. The tuning was achieved with a Brewster's angle two-plate birefringent filter in the laser cavity. When the laser was tuned to 1.75 μm the observed pulse duration was 240 ns at HWHM and the peak output power was approximately 6 mJ. The size of the beam was measured with a knife edge technique [Bi85]. The beam was found to have a spot size of 200 x 250 μm.

Wavelength selection of the fluorescence was achieved with a 0.75m Spex 1702/04 spectrometer equipped with 1200 grooves/mm grating for the visible region of the spectrum. Narrow band filters were used for wavelength selection in the IR spectral region.

The luminescence signals after wavelength selection were monitored with a Hamamatsu GaAs photocathode photomultiplier in the visible region of the spectrum and an EG&G Optoelectronics Indium Antimonide detector in the IR region of the spectrum. The Hamamatsu PMT was housed in a Products for Research, Inc. housing that could be cooled with water to 40°C below ambient temperatures. The EG&G detector was liquid nitrogen cooled to 77 K°.

The voltage signals from the detectors were recorded with a LeCroy CAMAC 6810 waveform recorder. The Catalyst software package for the LeCroy CAMAC was

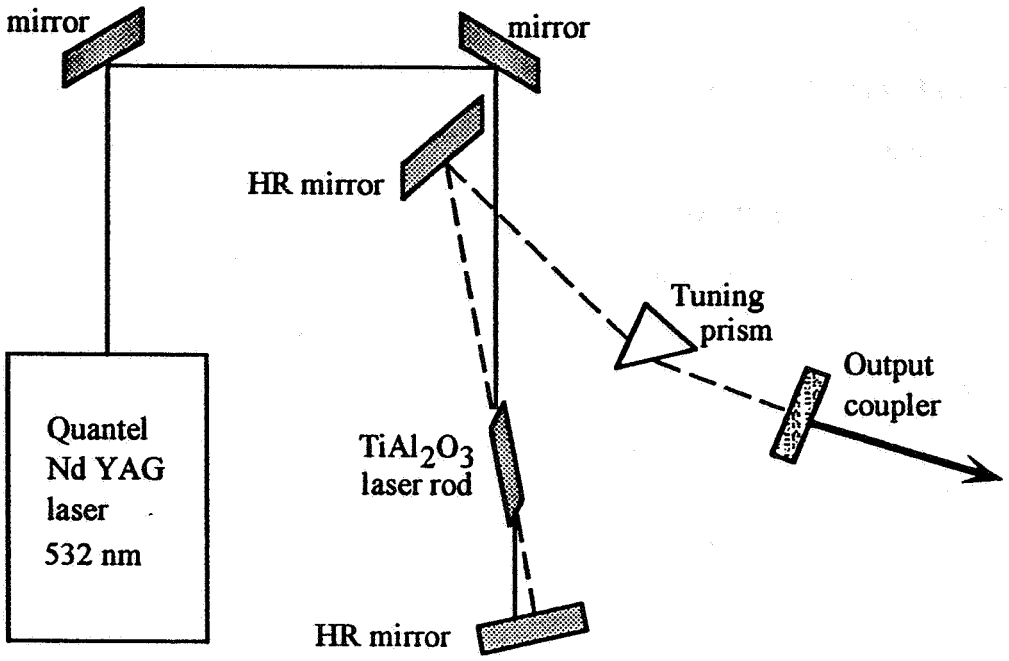

Figure 4-5 Pumping System and Optical Schematic of the Ti:Al_2O_3 Laser

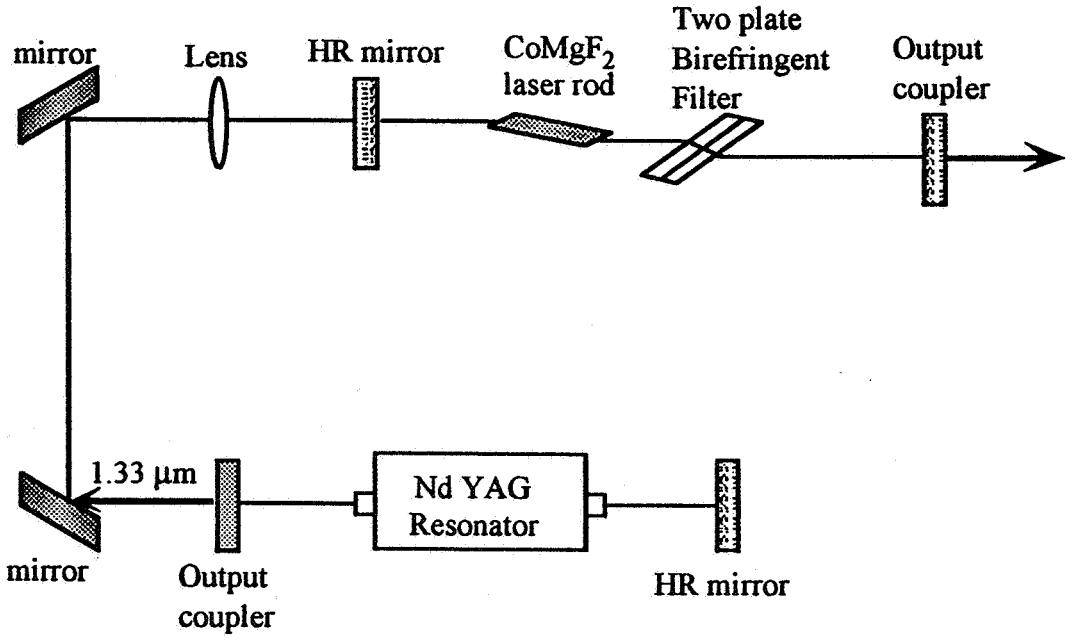

Figure 4-6 Pumping System and Optical Schematic of the $CoMgF_2$ Laser

used to perform an on screen average of the digitized signal waveform. In this way, fluctuations from background noise could be eliminated by averaging over say 500 or 1000 waveforms. No preamplifiers were used to boost the signal level and the inputs from the detectors were terminated with a 50Ω resistor to eliminate distortions of the signal waveform by transients in the equipment circuitry.

4.4 Temperature Controls

The temperature controlling system used consisted of four interconnected units: an RMC Cryosystems coldhead, an RMC Cryosystems model EC-2 compressor, a Veeco VS-9 vacuum pumping station, and a Lakeshore 320 Autotuning Temperature Controller. The apparatus is shown in figure 4.5.

The vacuum pumping station serves to remove air and other impurities from the coldfinger cavity to better than 10^{-3} Torr. This is necessary to minimize convective heat conduction and achieve cryogenic temperatures less than 70K°.

The cryogenic system operates as a closed-cycle refrigeration unit using compressed helium gas that expands inside the coldhead. The heat is removed by passing the helium through a heat exchanger to cool the crystal below ambient temperatures.

The temperature inside the coldfinger was monitored with a Lakeshore 320 temperature controller, which contained a silicon diode. The Lakeshore unit was autotuning down to about 23°K where the accuracy was rated at 23°K ± .5°K. The unit was able to control down to 10°K with a reduced accuracy of ± 1°K.

4.5 Spectroscopic Samples

The spectroscopic samples used in this study were crystals of Lithium Yttrium Fluoride, $LiYF_4$ (YLF), doped with triply ionized rare earth ions of Thulium (Tm^{3+}) and

Holmium (Ho^{3+}). Both singly doped and co-doped samples were used. A list of the samples available for study and the corresponding percent concentrations of the dopant ions is given below.

a.) Tm(4%)Ho(0.5%) YLF
b.) Tm(4%)Ho(1.0%) YLF
c.) Tm(4%)Ho(1.5%) YLF
d.) Tm(5%)Ho(0.2%) YLF
e.) Tm(6%)Ho(1%) YLF
f.) Tm(12%)Ho(1%) YLF
g.) Tm(0.2%)Ho(12%) YLF
h.) Tm(0.5%) YLF
i.) Tm(3%) YLF
j.)Tm(12%) YLF

Samples a, b, c, d, f, g, i, and j were acquired from Oklahoma State University and were grown by the Bridgman method. Sample e came from Optical Lightning Corporation (growth method unknown). Sample h was from M.I.T and was grown using the Czochralski method. All the samples were compared to each other for accuracy of their dopant concentrations. It was found that samples f, g, and j, were in error from what the manufacturer specified. They were compared to samples whose dopant concentrations were known accurately, and corrected accordingly. The corrected values are the same as those given above. Throughout this thesis samples a-k will be referred to without the percentage sign. For example Tm(4%)Ho(0.5%) will be referred to simply as Tm(4)Ho(.5).

References to Chapter 4

[Bi85] H.R. Bilger and T. Habib, "Knife-edge scanning of an astigmatic Gaussian Beam," Appl. Optics **24**, 686-690 (1985)

CHAPTER 5
YLF: Ho - Results and Interpretation

The views of space and time which I lay before you have sprung from the soil of experimental physics, and therin lies their strength.

Hermann Minkowski
Space and Time

5.1 Energy Levels of YLF: Ho

The energy levels for Ho^{3+} in $LiYF_4$ have previously been measured and are reported in [KaWo76]. In this thesis the experimental set of energy levels found in this reference will be used exclusively. On the basis of these energy levels, an energy level diagram was constructed. This is pictured in figure 5-1.

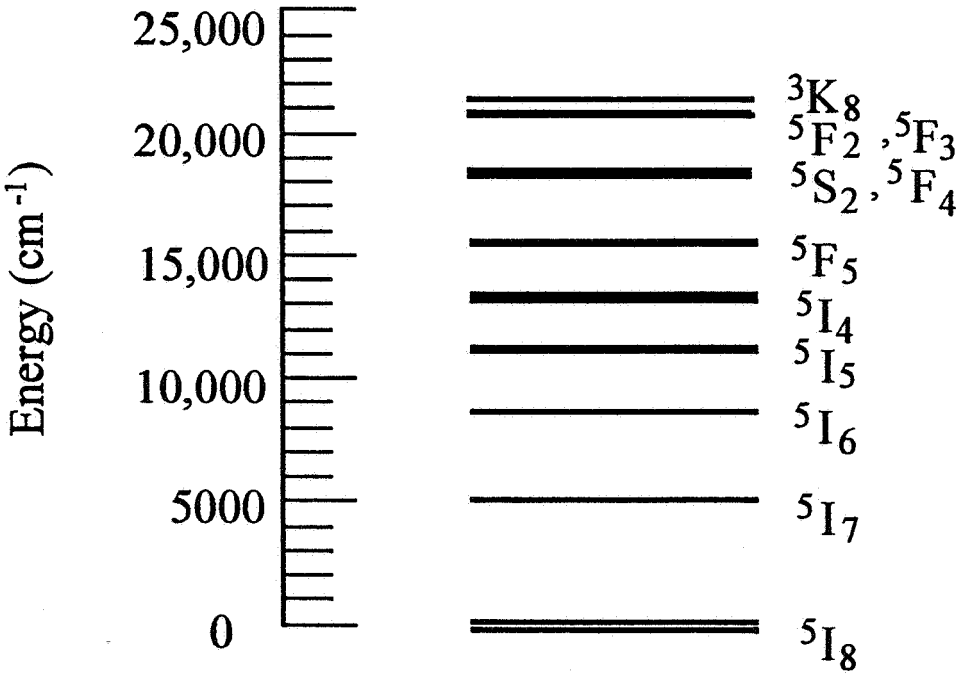

Figure 5-1 Energy Level Diagram of YLF:Ho

Tables for the upper and lower transition wavelengths (table 5-1a) and energies (table 5-1b) for a given manifold in YLF:Ho have been made from the energy levels given in [KaWo76]. These tables are useful when looking for a resonance between a given pair of manifolds.

Table 5-1a Range of Transitions (nm) in YLF: Ho

	5I8	5I7	5I6	5I5	5I4	5F5	5S2	5F4	5F3	5F2..
5I8	0	1889	1136	882	738	638	539	534	481	471
	0	2066	1196	915	777	659	550	546	492	480
5I7	-	0	2744	1618	1193	952	747	737	640	622
	-	0	2961	1681	1267	981	758	751	652	631
5I6	-	-	0	3755	2056	1431	1014	996	827	797
	-	-	0	4091	2278	1494	1032	1020	845	811
5I5	-	-	-	0	4363	2265	1372	1339	1050	1002
	-	-	-	0	5402	2408	1399	1376	1075	1021
5I4	-	-	-	-	0	4048	1872	1810	1320	1245
	-	-	-	-	0	5120	2021	1973	1409	1318
5F5	-	-	-	-	-	0	3290	3103	1897	1745
	-	-	-	-	-	0	3541	3395	2010	1830
5S2	-	-	-	-	-	-	0	43668	4391	3656
	-	-	-	-	-	-	0	133333	4750	3855
5F4	-	-	-	-	-	-	-	0	4638	3825
	-	-	-	-	-	-	-	0	5202	4147
5F3	-	-	-	-	-	-	-	-	0	17123
	-	-	-	-	-	-	-	-	0	27548

Table 5-1b. Range of Transitions (cm^{-1}) of YLF: Ho

	5I8	5I7	5I6	5I5	5I4	5F5	5S2	5F4	5F3	5F2..
5I8	0	5293	8796	11333	13532	15654	18524	18707	20755	21213
	0	4838	8355	10925	12869	15170	18163	18284	20314	20803
5I7	-	0	3643	6180	8379	10501	13371	13554	15602	16060
	-	0	3377	5947	7891	10192	13185	13306	15336	15825
5I6	-	-	0	2663	4862	6984	9854	10037	12085	12543
	-	-	0	2444	4388	6689	9682	9803	11833	12322
5I5	-	-	-	0	2292	4414	7284	7467	9515	9973
	-	-	-	0	1851	4152	7145	7266	9296	9785
5I4	-	-	-	-	0	2470	5340	5523	7571	8029
	-	-	-	-	0	1953	4946	5067	7097	7586
5F5	-	-	-	-	-	0	3039	3222	5270	5728
	-	-	-	-	-	0	2824	2945	4975	5464
5S2	-	-	-	-	-	-	0	229	2277	2735
	-	-	-	-	-	-	0	75	2105	2594
5F4	-	-	-	-	-	-	-	0	2156	2614
	-	-	-	-	-	-	-	0	1922	2411
5F3	-	-	-	-	-	-	-	-	0	584
	-	-	-	-	-	-	-	-	0	363

5.2 Judd-Ofelt Analysis of YLF:Ho

The Judd-Ofelt theory has become a standard tool for the calculation of radiative transition probabilities of rare earth ions in solids. The basic principals and relevant equations of this theory have already been given in chapter 2. The application of this theory to YLF:Ho will be presented in this section.

Absorption measurements were made on a sample of YLF doped with 0.5% Holmium - Ho(.5). Since YLF is an anisotropic crystal that exhibits different absorption intensities for different polarizations, two sets of spectra were collected over the wavelength range 300 - 2300 nm. The absorption spectra for π-polarization appear in figures 5-2, and the absorption spectra for σ-polarization appear in figures 5-3.

The measured quantities in the Judd-Ofelt theory are the integrated absorption profiles over a given manifold, but since there are two polarizations to consider, they must be suitably averaged to find the total integrated absorption. Toward this end, a modified Beer-Lambert law for absorption attenuation can be written as (Appendix A):

$$I(\lambda) = I_o\left\{\frac{1}{3}\exp[-\sigma_\pi(\lambda)N\ell] + \frac{2}{3}\exp[-\sigma_\sigma(\lambda)N\ell]\right\} \qquad (5\text{-}1)$$

A spatially averaged Beer-Lambert law can be written as $I(\lambda) = I_o\exp[-\bar{\sigma}(\lambda)N\ell]$ such that the spatially averaged cross section is:

$$\bar{\sigma}(\lambda) = -\frac{1}{N\ell}\ln\left\{\frac{1}{3}\exp[-\sigma_\pi(\lambda)N\ell] + \frac{2}{3}\exp[-\sigma_\sigma(\lambda)N\ell]\right\} \qquad (5\text{-}2)$$

Integrating eq. 5-2 over the entire manifold gives the integrated cross section:

$$\bar{\Gamma} = -\frac{1}{N\ell}\int_{\text{manifold}}\ln\left\{\frac{1}{3}\exp[-\sigma_\pi(\lambda)N\ell] + \frac{2}{3}\exp[-\sigma_\sigma(\lambda)N\ell]\right\}\,d\lambda \qquad (5\text{-}3)$$

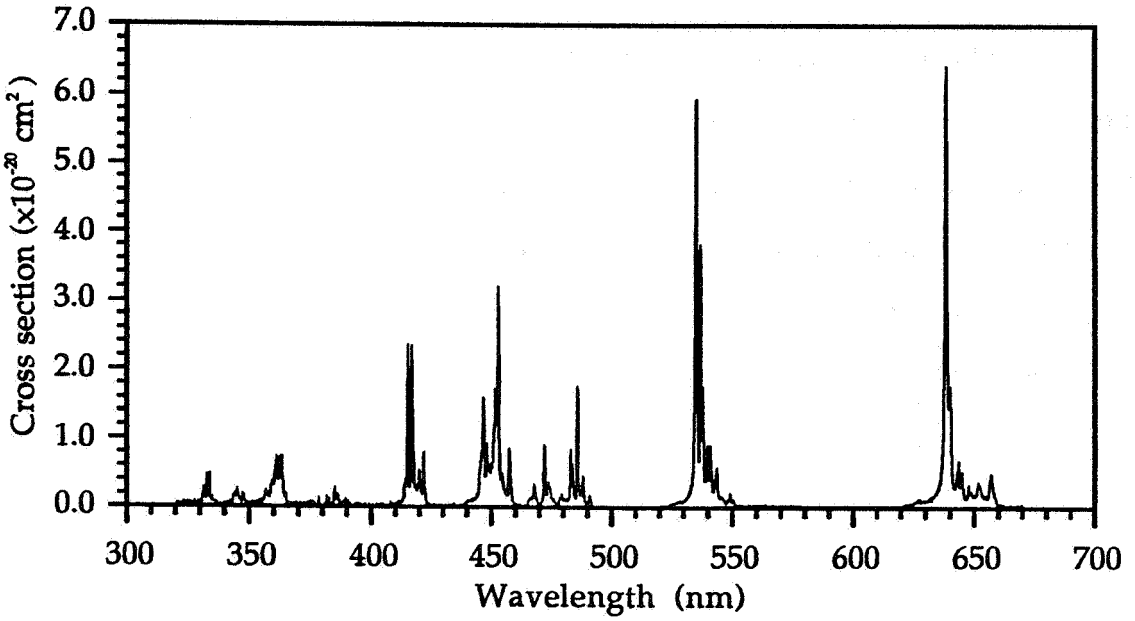

Figure 5-2a Visible Absorption Spectrum in YLF:Ho π-polarization

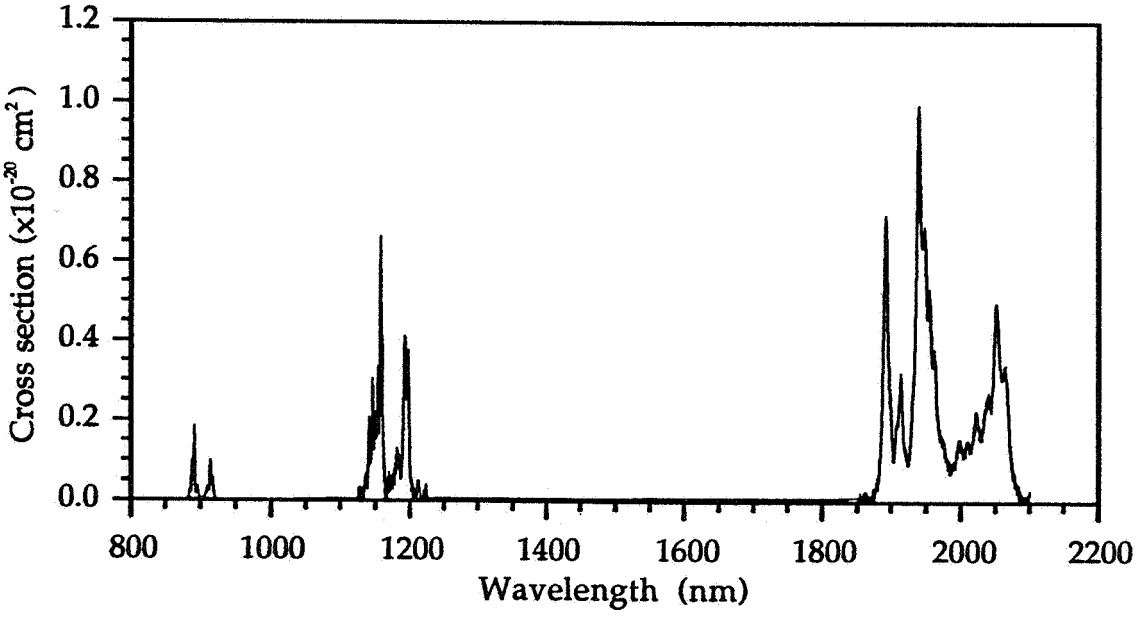

Figure 5-2b Infrared Absorption Spectrum in YLF:Ho π-polarization

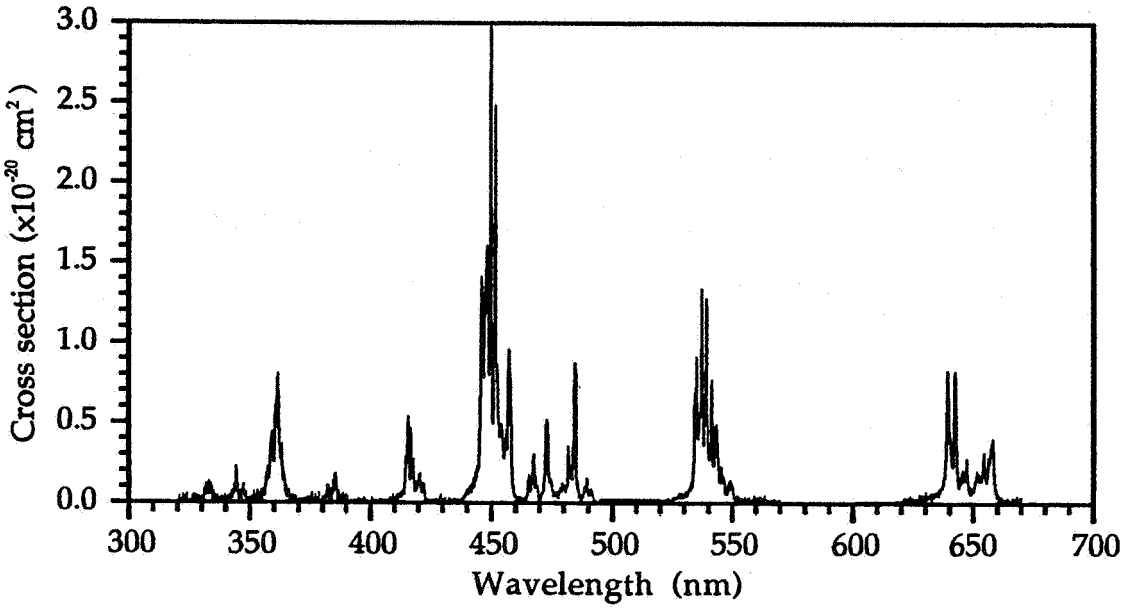

Figure 5-3a Visible Absorption Spectrum in YLF:Ho σ-polarization

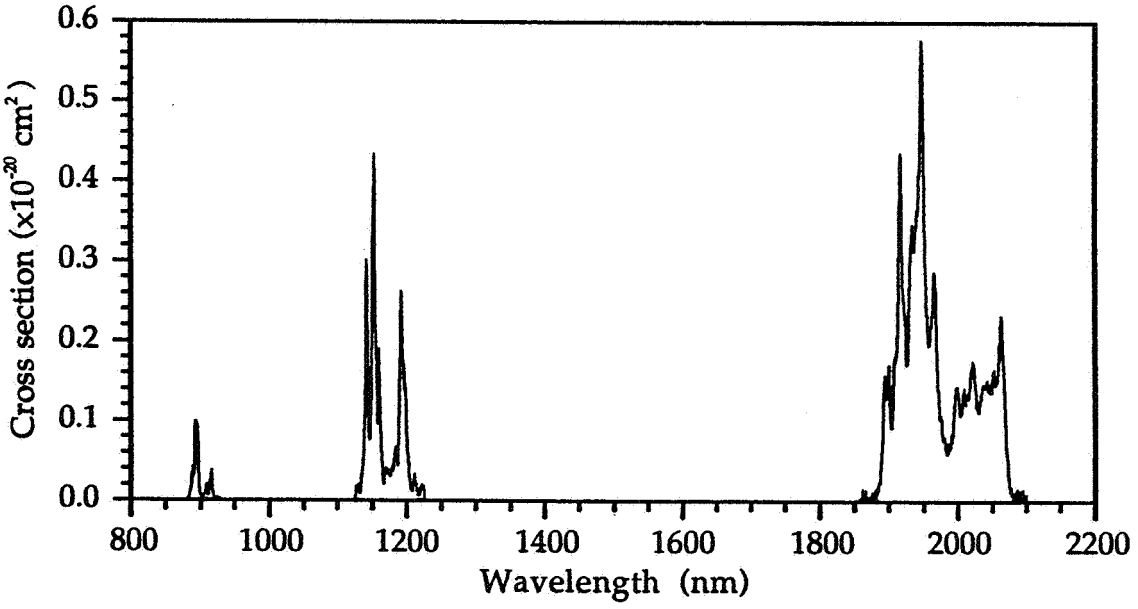

Figure 5-3b Infrared Absorption Spectrum in YLF:Ho σ-polarization

Equation 5-3 was used for the calculation of integrated absorption profiles. These were then substituted into eq. 2-13, along with the other constants and parameters appearing in that equation, to find the experimental electric dipole line strengths.

A computer program was written to perform a least squares fit between the experimental linestrengths found using eq. 2-13, and the theoretical linestrengths of eq. 2-5. The object is to vary the Judd-Ofelt intensity parameters until the difference in the squares of the experimental and theoretical line strengths is minimized. The procedure is the same as that outlined by Krupke [Kr71]. If the three Judd-Ofelt parameters are made to form a column vector Ω, and the doubly reduced matrix elements form an n x m matrix **M**, where n is the number of transitions to fit, and m is the number of parameters to vary in the fit (in this case m=3 corresponding to the 3 Judd-Ofelt parameters), then the theoretical line strength then be written as a 1 x n column vector. This can be expressed as:

$$\mathbf{S} = \mathbf{M}\Omega \tag{5-4}$$

The set of Judd-Ofelt parameters that minimizes the sum of the squares of the differences between the theoretical and experimental line strengths is found from matrix algebra to be (Appendix B):

$$\Omega^{o} = (\mathbf{M}^{\dagger}\mathbf{M})^{-1}\mathbf{M}^{\dagger}\mathbf{S}^{E} \tag{5-5}$$

where $\mathbf{M}^{\dagger}$ is the adjoint of matrix **M** and $(\mathbf{M}^{\dagger}\mathbf{M})^{-1}$ is the inverse matrix of $\mathbf{M}^{\dagger}\mathbf{M}$. The measure of the quality of the fit is given by the root mean square deviation, expressed as:

$$\text{RMS } \Delta S = [\ \Sigma(\Delta S)^{2}/(\#\text{ Transitions to fit} - \#\text{ of parameters to fit})]^{1/2}$$

This procedure was also carried out by hand to ensure that the computer program was giving correct results. The Judd-Ofelt parameters for YLF:Ho were found to be:

$$\Omega_2 = 0.7483 \times 10^{-20}\ cm^2$$
$$\Omega_4 = 1.6168 \times 10^{-20}\ cm^2$$
$$\Omega_6 = 1.2269 \times 10^{-20}\ cm^2$$

This set of parameters were utilized to calculate the manifold to manifold spontaneous emission probabilities $A(\psi J,\psi' J')$ using eq. 2-5 and eq. 2-12. From the discussion in chapter 2, it is recalled that J refers to the initial state and J' refers to the final state. The radiative lifetime is found by summing over the inverse of the transition probabilities for all states below the one under consideration. This is expressed as:

$$\tau_{rad} = \frac{1}{\sum_i A(\psi J,\psi' J')} \tag{5-6}$$

The branching ratio for a given transition probability can be written as:

$$\beta_{ji} = \frac{A(\psi J,\psi' J')}{\sum_i A(\psi J,\psi' J')} \tag{5-7}$$

The results of the Judd-Ofelt analysis are presented in table 5-2. The first part of the table shows the manifolds used in the fit, their corresponding square matrix elements and the measured and theoretical values for the electric dipole linestrength. The $^5I_7$ manifold was excluded from the fit due to its strong magnetic dipole contribution. The second part of the table shows the values found for the transition probability (A_{ED}) from the initial J state to the final J' state, the branching ratio for the given transition, and the radiative lifetime from the J' state to the ground state found from eq. 5-6.

Table 5-2 Judd-Ofelt Fit for YLF: Ho

Transition from 5I8	$[U^{(2)}]^2$	$[U^{(4)}]^2$	$[U^{(6)}]^2$	λ(nm)	S meas. $x10^{-20}$ cm^2	S theor. $x10^{-20}$ cm^2
3K6+3F4	0.0026	0.1262	0.0073	334	0.1421	0.2146
3L9+5G3	0.0185	0.0052	0.1669	345	0.2118	0.2275
3D2+3H6+5G5	0.2155	0.1969	0.1679	360	0.9189	0.6858
3K7+5G4	0.0058	0.0361	0.0697	385	0.1796	0.1483
3G5	0	0.5338	0.0002	418	0.9251	0.8620
5F1+5G6	1.5201	0.8410	0.1411	448	2.6378	2.6704
3K8	0.0208	0.0334	0.1535	467	0.2814	0.2583
3F2	0	0	0.2041	473	0.2789	0.2510
3F3	0	0	0.3464	486	0.4729	0.4260
5F4+5S2	0	0.2392	0.9339	540	1.6620	1.5348
5F5	0	0.4250	0.5687	645	1.2203	1.3856
5I5	0	0.0100	0.0936	886	0.0550	0.1312
5I6	0.0084	0.0386	0.6921	1175	0.8090	0.9198

Judd-Ofelt Parameters: $\Omega_2 = 0.7483x10^{-20}$ $\Omega_4 = 1.6168x10^{-20}$ $\Omega_6 = 1.2269x10^{-20}$

Root Mean Square deviation: $\delta = 0.10909x10^{-20}$

Transition J->J'	wavelength λ(nm)	S theor. $x10^{-20}$ cm^2	A_{ED} (sec^{-1})	A_{MD} (sec^{-1})	branching ratio β	τ_{rad} (μs)
5F4 - 5S2	67567.7	0.030	0.00		0.000	
5F4 - 5F5	3173.6	0.305	2.03		0.001	
5F4 - 5I4	1887.5	0.356	11.58		0.005	
5F4 - 5I5	1386.8	0.786	73.99		0.033	442
5F4 - 5I6	985.8	0.626	144.52		0.064	
5F4 - 5I7	737.9	0.361	199.62		0.088	
5F4 - 5I8	536.1	1.258	1832.72		0.809	
5S2 - 5F5	3330.0	0.022	0.23		0.000	
5S2 - 5I4	1941.7	0.390	20.94		0.016	
5S2 - 5I5	1353.9	0.138	21.95		0.016	
5S2 - 5I6	1000.4	0.223	88.55		0.067	751
5S2 - 5I7	746.0	0.504	485.35		0.365	
5S2 - 5I8	540.4	0.279	714.38		0.537	
5F5 - 5I4	4657.7	0.015	0.02		0.000	
5F5 - 5I5	2281.5	0.252	3.77		0.003	
5F5 - 5I6	1430.0	0.818	50.31		0.041	820
5F5 - 5I7	961.4	1.080	219.84		0.180	
5F5 - 5I8	645.0	1.390	944.96		0.775	
5I4 - 5I5	4472.3	1.342	3.05		0.056	
5I4 - 5I6	2063.6	0.864	21.44		0.396	
5I4 - 5I7	1211.5	0.198	24.57		0.454	18496
5I4 - 5I8	748.7	0.009	5.01		0.093	
5I5 - 5I6	3831.4	1.013	3.08		0.039	
5I5 - 5I7	1661.7	1.132	44.24		0.553	12502
5I5 - 5I8	899.3	0.131	32.66		0.408	
5I6 - 5I7	2934.3	1.384	8.15		0.086	
5I6 - 5I8	1175.1	0.919	86.46		0.914	10570
5I7 - 5I8	1960.0	2.107	36.67	21.4	1.000	17500

5.3 Emission Cross Sections in YLF:Ho

The methods of obtaining emission cross sections have already been discussed in chapter 2. The emission cross sections for YLF:Ho can be obtained directly from eq. 2-17. Since YLF is an anisotropic crystal, eq. 2-17 must be rewritten to account for the different polarizations of the measured luminescence spectrum. This is easily done by weighting the lineshape function as 2/3 σ-pol. and 1/3 π-pol. Equation 2-16 for a uniaxial crystal becomes :

$$g^{\alpha}(\nu) = \frac{3I_{\alpha}(\lambda)}{\int \frac{2I_{\sigma}(\lambda) + I_{\pi}(\lambda)}{\lambda^2} d\lambda} \tag{5-8}$$

where α denotes a given polarization (π or σ).

Equation 2-17 now becomes:

$$\sigma^{\alpha}(\lambda) = \frac{\lambda^2}{8\pi c n^2 \tau_{rad}} \cdot \frac{3I_{\alpha}(\lambda)}{\int \frac{2I_{\sigma}(\lambda) + I_{\pi}(\lambda)}{\lambda^2} d\lambda} \tag{5-9}$$

Emission spectra were taken for singly doped YLF:Ho. Since Holmium shows no absorption in the range accessible by our diode laser (785 nm), the crystal was pumped with a 35mW Helium-Neon laser operating at 635 nm. This wavelength corresponds to the $^5F_5$ manifold in YLF:Ho (see figure 5-1). Emission spectra were taken over both polarizations in the wavelength range 800 - 2200 nm, and then corrected for grating efficiency and detector response with a tungsten lamp source operating at 2854°K. Calibrating the spectra is a very important procedure because over a given wavelength range the grating has a given efficiency curve for the scattering of light and the detector used has a response curve associated with it. As a result, the luminescence spectra

collected do not always reflect the relative intensities of the peaks in a wavelength range encompassing a manifold. This procedure seems to be one which is passed along to researchers through experience. I was not able to find the procedure in print anywhere. Therefore, for the benefit of researchers who are unaware of this technique, it is included in Appendix C.

Emission cross sections were calculated from eq. 2-24 using absorption cross section data (see figures 5-2 and 5-3), and calculated partition functions from energy level data [KaWo76]. Table 5-3 contains Boltzmann fractions for the Stark levels of the four lowest manifolds in YLF:Ho. The partition functions for each manifold appear at the bottom of the tables. The emission cross section was determined independently from the modified Füchtbauer-Ladenberg equation (eq. 5-9) by adjusting the radiative lifetime such that values for the emission cross section were in best agreement with those obtained from eq. 2-24. In this way a set of radiative lifetimes for the manifolds studied in YLF:Ho were determined. The results of this procedure are presented in figures 5-4, 5-5, and 5-6. The radiative lifetimes for the manifolds studied are given in table 5-4. The branching ratios for the appropriate manifolds were found from the Judd-Ofelt results in table 5-2. The radiative lifetime found for the $^5I_7$ manifold in YLF:Ho is in good agreement with the value 14.2 ms found by [Pa92].

5.4 Luminescence Decay in YLF:Ho

A crystal of singly doped YLF:Ho with 0.5% Ho concentration was excited using a Ti:Al_2O_3 (Titanium Sapphire) laser operating at 25 mJ with 100 ns pulses. The wavelength of the laser was tuned to 892 nm, which corresponds to the $^5I_5$ manifold of YLF:Ho (see figure 5-1). Emission was monitored with a Hewlett-Packard 54504A digitizing oscilloscope at the wavelengths 537nm ($^5S_2$), 658 nm ($^5F_5$), and 912 nm ($^5I_5$). The data were collected with the Labview software package.

Table 5-3 Boltzmann Fractions in YLF:Ho @300K

Level#	Ho 5I8 Energy (cm^{-1})	Ho 5I8 Boltz. frac.	Ho 5I7 Energy (cm^{-1})	Ho 5I7 Boltz. frac.	Ho 5I6 Energy (cm^{-1})	Ho 5I6 Boltz. frac.	Ho 5I5 Energy (cm^{-1})	Ho 5I5 Boltz. frac.
1	0	0.10871	5153	0.08760	8670	0.09298	11240	0.10460
2	0	0.10871	5157	0.08635	8671	0.09253	11240	0.10460
3	7	0.10512	5157	0.08635	8680	0.08862	11240	0.10460
4	23	0.09735	5164	0.08310	8680	0.08862	11245	0.10212
5	48	0.08635	5175	0.07771	8686	0.08561	11248	0.10066
6	56	0.08310	5185	0.07514	8686	0.08561	11248	0.10066
7	72	0.07696	5185	0.07514	8687	0.08570	11252	0.09875
8	72	0.07696	5207	0.06794	8696	0.08208	11298	0.07920
9	217	0.03839	5229	0.06114	8701	0.08013	11327	0.06891
10	270	0.02978	5229	0.06114	8768	0.05811	11327	0.06891
11	270	0.02978	5233	0.05912	8783	0.05407	11333	0.06696
12	276	0.02893	5291	0.04498	8783	0.05407		
13	283	0.02798	5293	0.04476	8796	0.05081		
14	290	0.02705	5293	0.04476				
15	303	0.02542	5293	0.04476				
16	303	0.02542						
17	315	0.02400						
Part. func.	Z= 9.1990		Z= 11.4150		Z= 10.7550		Z= 9.5601	

Table 5-4 Radiative Lifetimes From Emission Cross Sections

Transition	Branching ratio β	τ_{rad}/β	τ_{rad}
$^5I_5 \rightarrow {}^5I_8$	$\beta_{58} = 0.408$	16.1 ms	6.56 ms
$^5I_6 \rightarrow {}^5I_8$	$\beta_{68} = 0.914$	6.20 ms	5.66 ms
$^5I_7 \rightarrow {}^5I_8$	$\beta_{78} = 1.000$	14.0 ms	14.0 ms

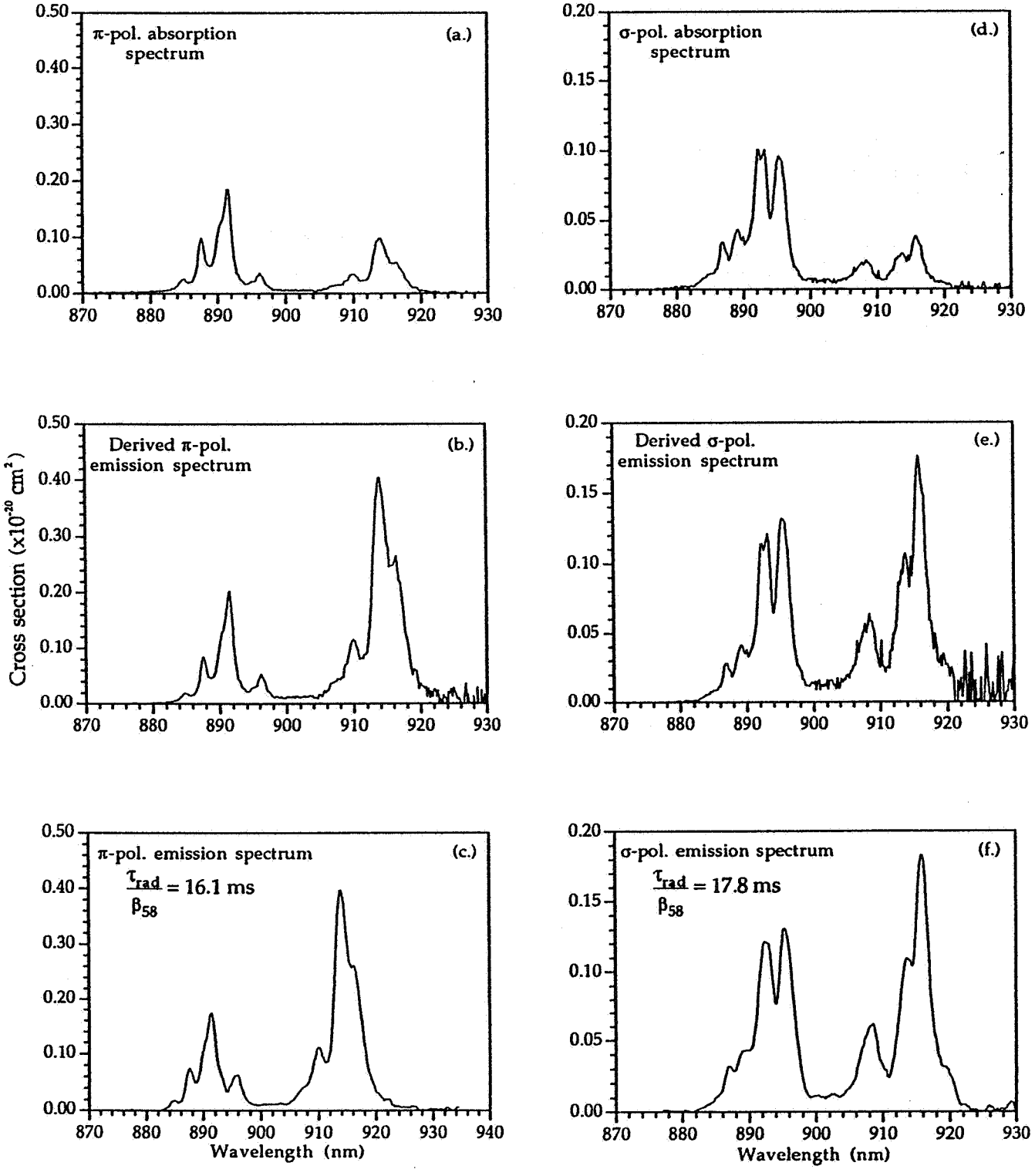

Figure 5-4 Cross Sections of the $^5I_5$ Manifold in YLF:Ho

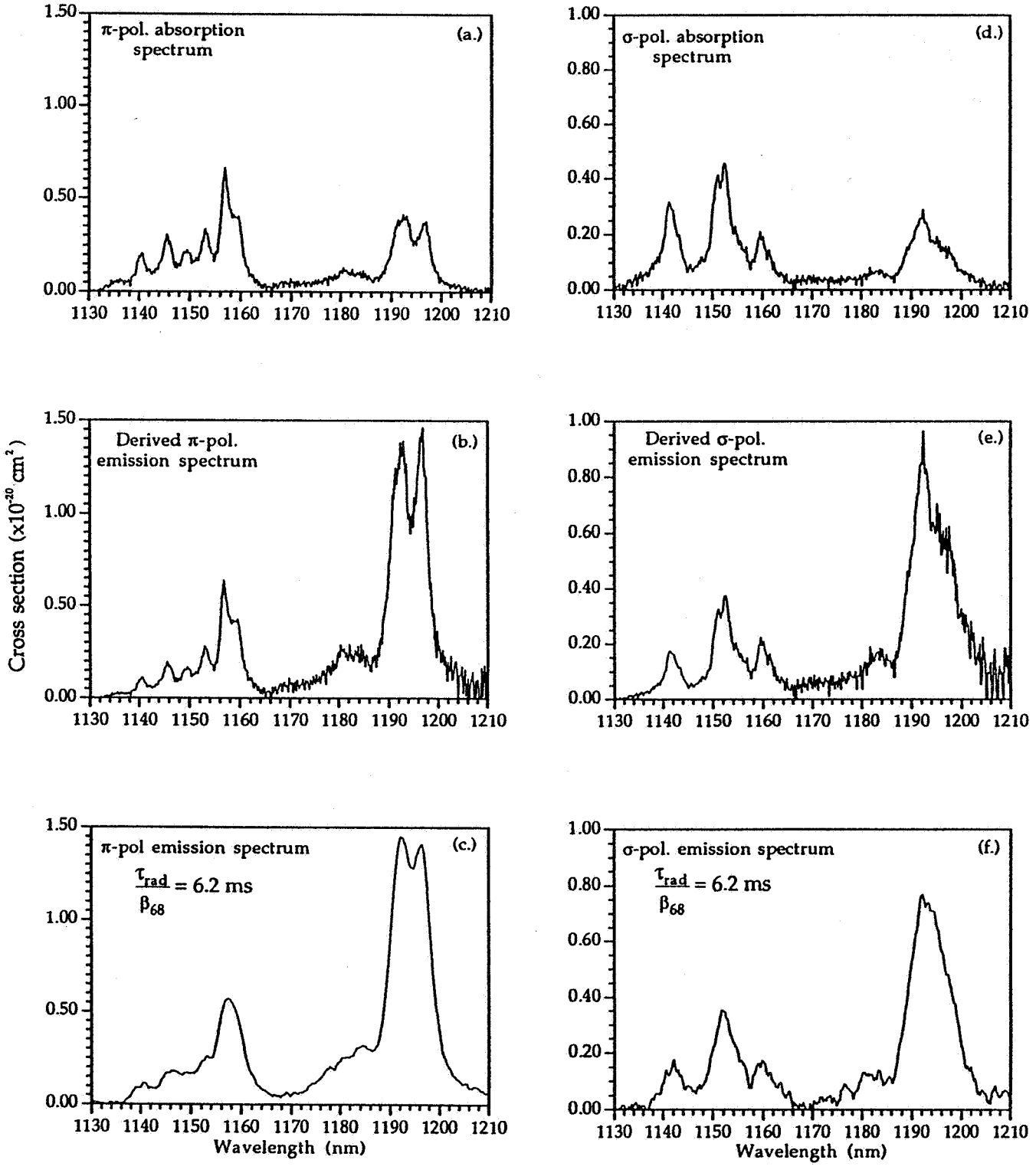

Figure 5-5 Cross Sections of the $^5I_6$ Manifold in YLF:Ho

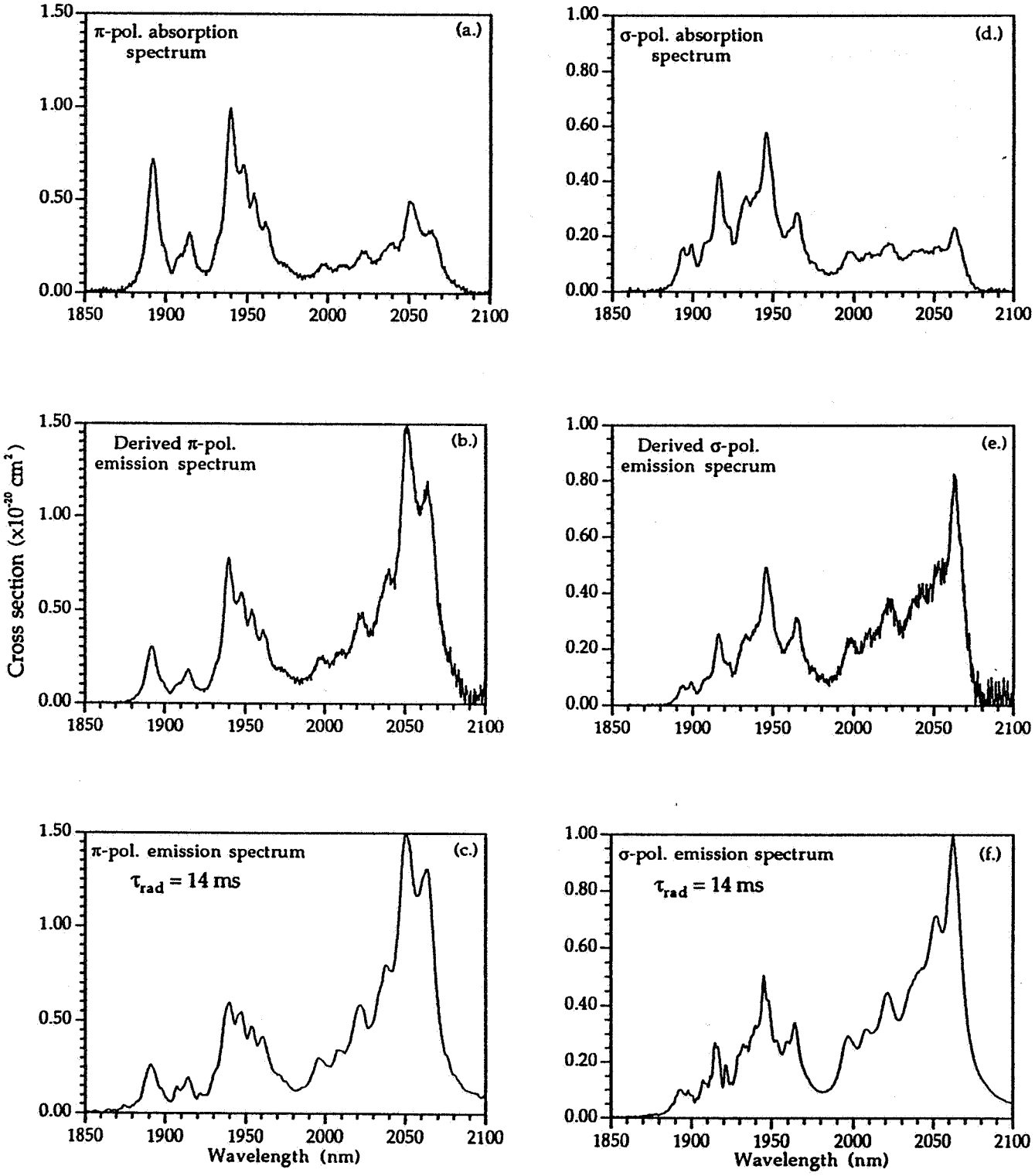

Figure 5-6 Cross Sections of the $^5I_7$ Manifold in YLF:Ho

The decay curves are shown in figure 5-7. Figure 5-7a shows the decay from the $^5I_5$ manifold at 912 nm. This manifold showed only one exponential decay with a decay time of 20μs. Figure 5-7b shows the decay from the $^5F_5$ manifold at 658 nm. This manifold showed an exponential rise with a rise time of 27μs and an exponential decay with a decay time of 105μs. Figure 5-7c shows the decay from the $^5S_2$ manifold at 537 nm. This manifold showed an exponential decay with a decay time of 105μs. From these data, luminescence lifetimes at room temperature (295K°) can be assigned. The lifetime of the $^5I_5$ manifold is 20μs. The lifetime of the $^5F_5$ manifold is 27μs and shows up as a rise time in Fig. 5-7b since this level if fed by a higher lying level, namely the $^5S_2$. The lifetime of the $^5S_2$ manifold is 105μs which show up as a decay in both figures 5-7b and 5-7c. It should be pointed out that the mechanism by which the $^5S_2$ manifold becomes populated when pumping the lower energy $^5I_5$ manifold is not clear at this time. At any rate, these assignments of lifetimes are consistent with measurements conducted by exciting the $^5S_2$ manifold and the $^5F_5$ manifold directly using a tunable dye laser. Table 5-5 is a tabulation of these results.

Table 5-5 Lifetimes Observed Under Different Excitation Wavelengths

Pump manifold	Emission from	$^5S_2$	$^5F_5$	$^5I_5$
$^5S_2$ @535 nm	Rise time (μs):	-----	27.3	32.0
	Decay time (μs):	100	115	100
$^5F_5$ @635 nm	Rise (μs):	5.16	-----	32.0
	Decay (μs):	103	32.4	18.9
$^5I_5$ @890 nm	Rise (μs):	fast	27.3	32.0
	Decay (μs):	105	105	20.0

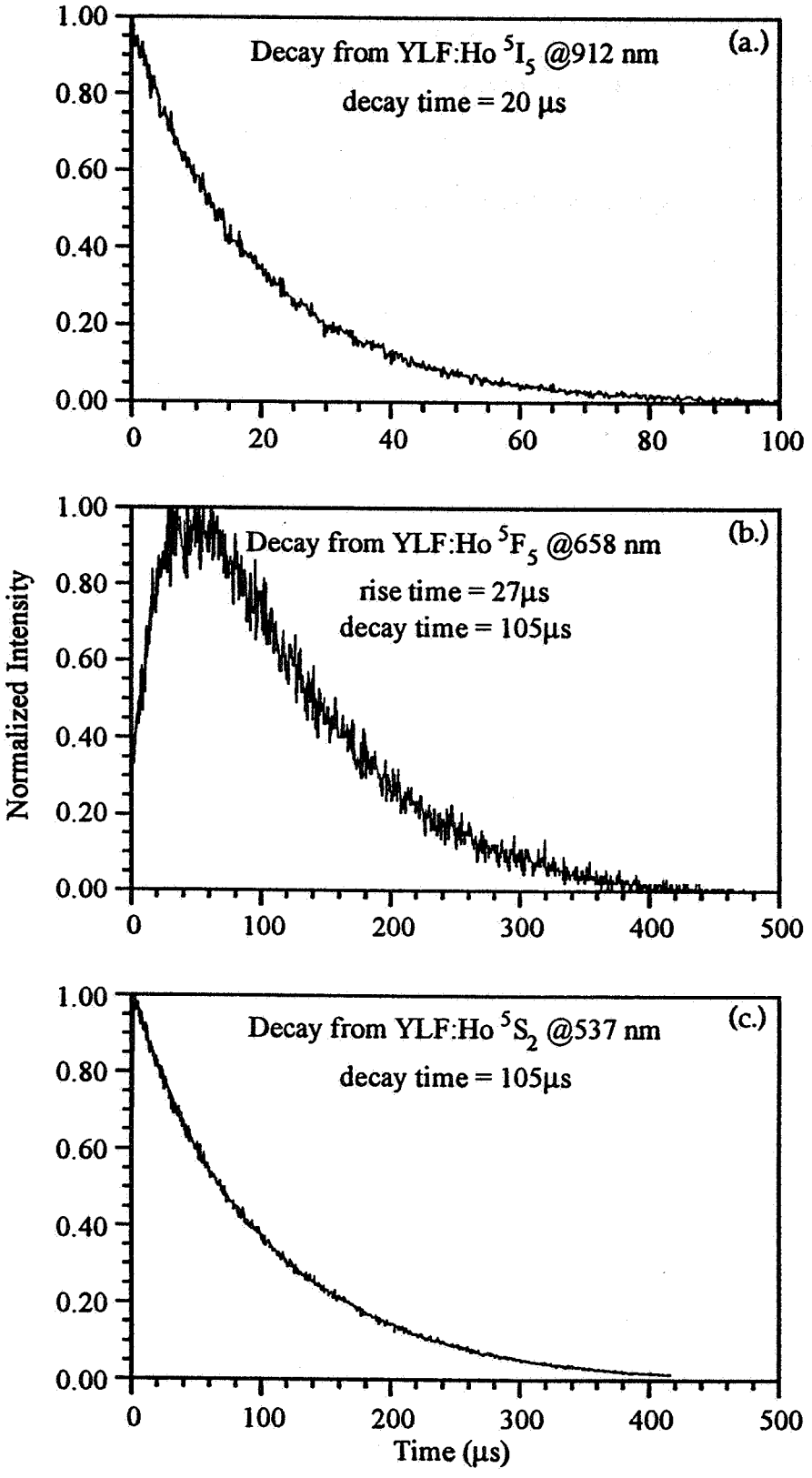

Figure 5-7 Decay Curves in YLF:Ho Exciting the $^5I_5$ Manifold @892 nm

Lifetime measurements have also been conducted on the same YLF:Ho sample using as an excitation source a $CoMgF_2$ (Cobalt Magnesium Fluoride) laser tuned to 1.96μm to directly excite the $^5I_7$ manifold of YLF:Ho. The emission from this manifold was monitored at 2.05μm. The decay curve is shown in figure 5-8. The $^5I_7$ manifold showed a single exponential decay with a decay time of 16.5 ms.

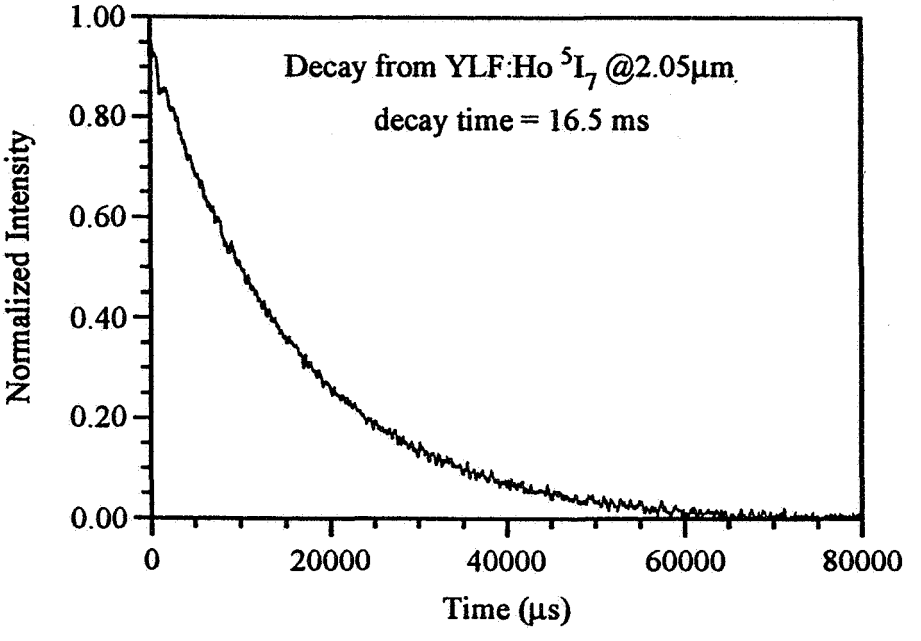

Figure 5-8 Decay from YLF:Ho Exciting the $^5I_7$ Manifold @1.96μm

References to Chapter 5

[KaWo76] N. Karayianis, D.E. Wortman and H.P. Jenssen, "Analysis of the optical spectrum of Ho^{3+} in $LiYF_4$,". Phys. Chem. Solids **37** ,675-682 (1976)

[Kr71] W.F. Krupke, "Radiative transition probabilities within the $4f^3$ ground configuration of Nd:YAG," IEEE J. Quantum Elec. **QE-7**, 153-159 (1971)

[Pa92] S. Payne, L.L. Chase, L.K. Smith, W.L. Kway and W.F. Krupke,"Infrared cross-section measurements for crystals doped with Er^{3+} ,Tm^{3+} and Ho^{3+}," IEEE J. Quantum Elec. **28**, 11, 2619-2629 (1992)

CHAPTER 6
YLF: Tm - Results and Interpretation

We dance round in a ring and suppose,
but the Secret sits in the middle and knows.

Robert Frost
The Secret Sits

6.1 Energy Levels of YLF: Tm

The energy levels for Tm^{3+} in $LiYF_4$ have previously been measured and are reported in [Je71] and [Du91]. The energy levels presented in these two references show some differences. Our low temperature absorption measurements made on YLF:Tm show better agreement with [Du91], so the experimental set of energy levels there will be used exclusively. An energy an energy level diagram of YLF:Tm is shown in fig. 6-1.

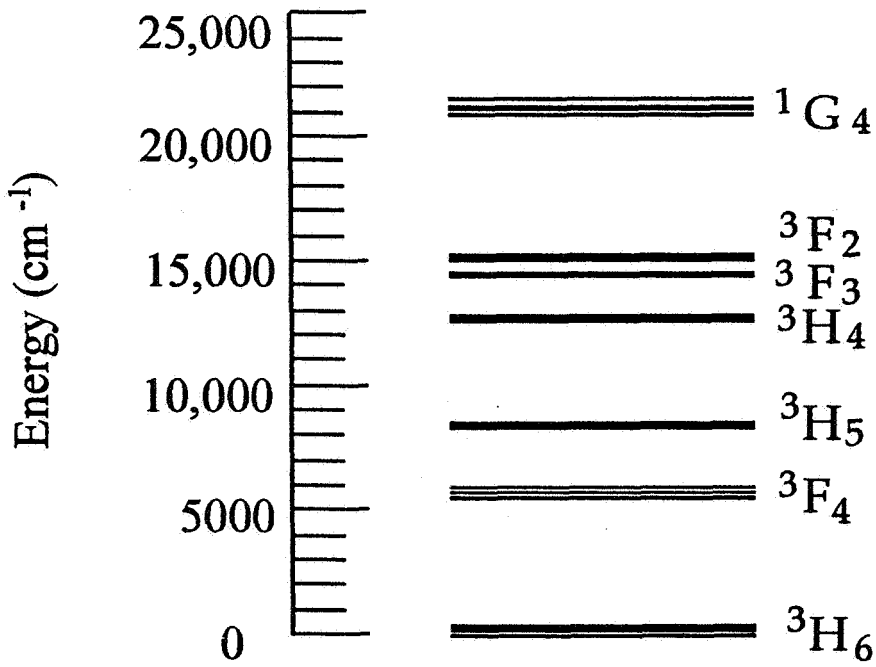

Figure 6-1 Energy Level Diagram of YLF:Tm

A set of tables for the upper and lower transition wavelengths and energies for a given manifold were made from the energy levels reported in [Du91]. The transition wavelengths in nm are given in table 6-1a , and for transition energy in cm^{-1} in table 6-1b.

Table 6-1a Range of Transitions (nm) in YLF: Tm

	3H6	3F4	3H5	3H4	3F3	3F2	1G4	1D2	1I6
3H6	0	1674	1171	775	685	654	463	356	285
	0	1930	1271	821	709	681	486	363	291
3F4	–	0	3405	1371	1111	1033	626	444	340
	–	0	4325	1508	1169	1096	666	454	347
3H5	–	–	0	2170	1584	1430	753	505	374
	–	–	0	2460	1670	1524	803	514	381
3H4	–	–	–	0	5005	3736	1115	646	446
	–	–	–	0	6138	4539	1237	663	457
3F3	–	–	–	–	0	13245	1420	737	488
	–	–	–	–	0	20120	1568	748	496
3F2	–	–	–	–	–	0	1546	770	502
	–	–	–	–	–	0	1755	788	514
1G4	–	–	–	–	–	–	0	1408	713
	–	–	–	–	–	–	0	1562	759
1D2	–	–	–	–	–	–	–	0	1421
	–	–	–	–	–	–	–	0	1502
1I6	–	–	–	–	–	–	–	–	0
	–	–	–	–	–	–	–	–	0

Table 6-1b. Range of Transitions (cm^{-1}) of YLF: Tm

	3H6	3F4	3H5	3H4	3F3	3F2	1G4	1D2	1I6
3H6	0	5972	8535	12891	14597	15275	21562	28075	34998
	0	5180	7865	12180	14101	14675	20554	27542	34310
3F4	–	0	2936	7292	8998	9676	15963	22476	29399
	–	0	2312	6627	8548	9122	15001	21989	28757
3H5	–	–	0	4607	6313	6991	13278	19791	26714
	–	–	0	4064	5985	6559	12438	19426	26194
3H4	–	–	–	0	1998	2676	8963	15476	22399
	–	–	–	0	1629	2203	8082	15070	21838
3F3	–	–	–	–	0	755	7042	13555	20478
	–	–	–	–	0	497	6376	13364	20132
3F2	–	–	–	–	–	0	6468	12981	19904
	–	–	–	–	–	0	5698	12686	19454
1G4	–	–	–	–	–	–	0	7102	14025
	–	–	–	–	–	–	0	6399	13167
1D2	–	–	–	–	–	–	–	0	7037
	–	–	–	–	–	–	–	0	6654
1I6	–	–	–	–	–	–	–	–	0
	–	–	–	–	–	–	–	–	0

6.2 Judd-Ofelt analysis of YLF:Tm

A theoretical discussion of the Judd-Ofelt theory has been given in chapter 2, and its application was described in chapter 5 for YLF:Ho. The result of the Judd-Ofelt analysis for YLF:Tm is given here.

Absorption measurements were made on a sample of Tm YLF doped with 0.5% thulium. Spectra were taken for both polarizations in the wavelength range 300 - 2300 nm. The absorption spectra for π-polarization appear in figures 6-2, and the absorption spectra for σ–polarization appear in figures 6-3.

As was discussed in the last chapter, equation 5-3 was used for the calculation of integrated absorption profiles, the values of which were then substituted into eq. 2-13 to find the experimental electric dipole linestrengths.

The method of least squares was applied in the same way as was done for YLF:Ho in chapter 5. The Judd-Ofelt intensity parameters were found for YLF:Tm to be:

$$\Omega_2 = 1.6673 \times 10^{-20} \text{ cm}^2$$
$$\Omega_4 = 1.9184 \times 10^{-20} \text{ cm}^2$$
$$\Omega_6 = 1.0897 \times 10^{-20} \text{ cm}^2$$

These intensity parameters were used to calculate the manifold to manifold spontaneous emission probabilities. The results are presented in table 6-2. The meaning of this table is the same as discussed in chapter 5. The $^3H_5$ was excluded from the fit due to its strong magnetic dipole contribution. It should be expected that the error associated with the spontaneous emission probabilities for YLF:Tm will be larger than that for YLF:Ho. There are a couple of reasons why this is believed to be true. The first concerns the width of the manifolds in Tm (e.g., the energy difference between the highest stark level and lowest stark level). The use of eq. 2-12 involves the use of an average wavelength for a given manifold. Since the widths of the manifolds are about twice as large

as those in Holmium, then there could possibly be more error associated with the calculations. The second reason has to do with the number of manifolds available for the least squares fit. As can be seen from table 6-2 there were only five manifolds available for a fit in which three parameters were being varied. This is a disadvantage since it requires more accuracy in the measured values to obtain a good set of fitting parameters.

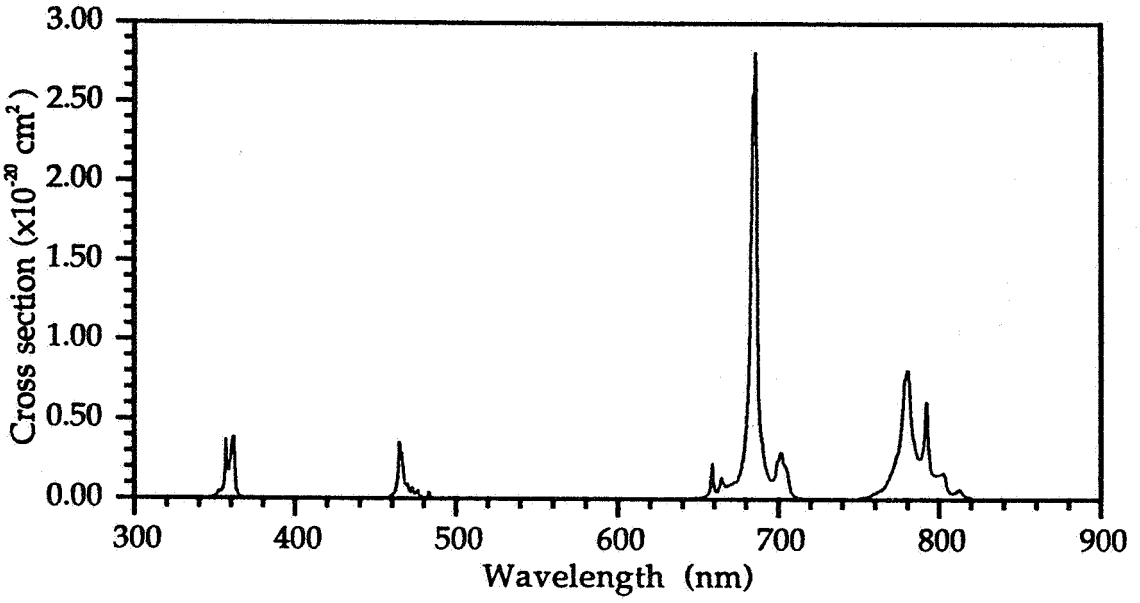

Figure 6-2a Visible Absorption Spectrum in YLF:Tm π-polarization

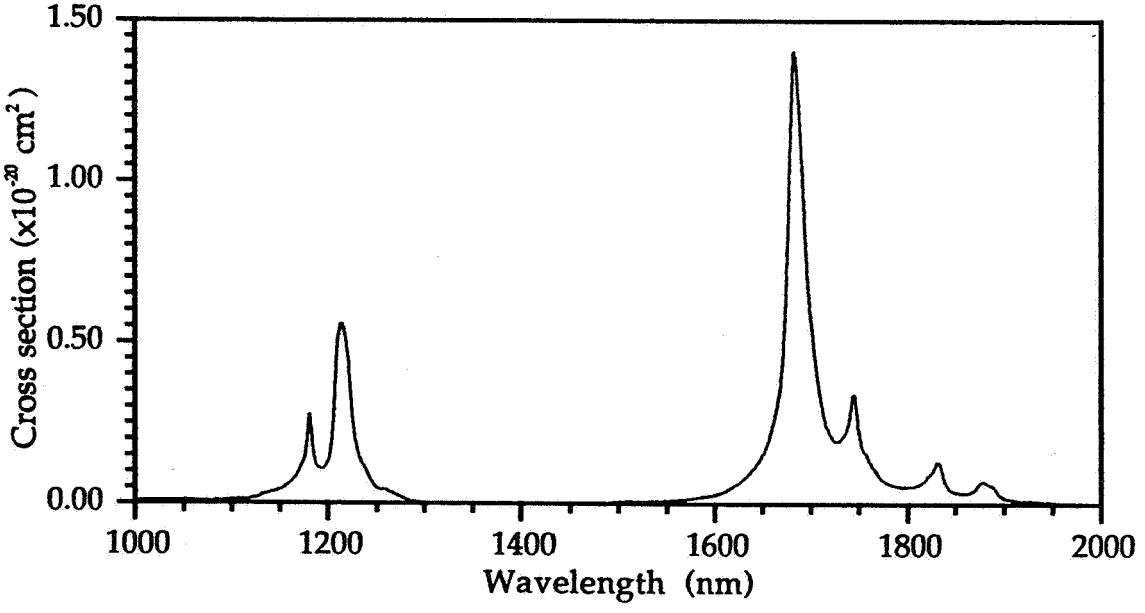

Figure 6-2b Infrared Absorption Spectrum in YLF:Tm π-polarization

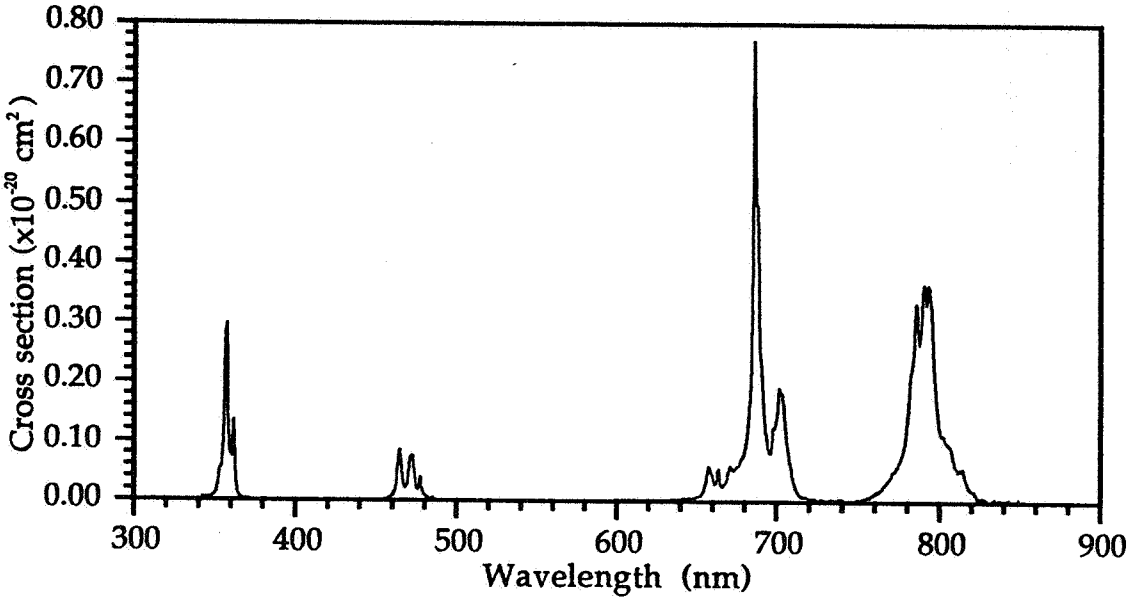

Figure 6-3a Visible Absorption Spectrum in YLF:Tm σ-polarization

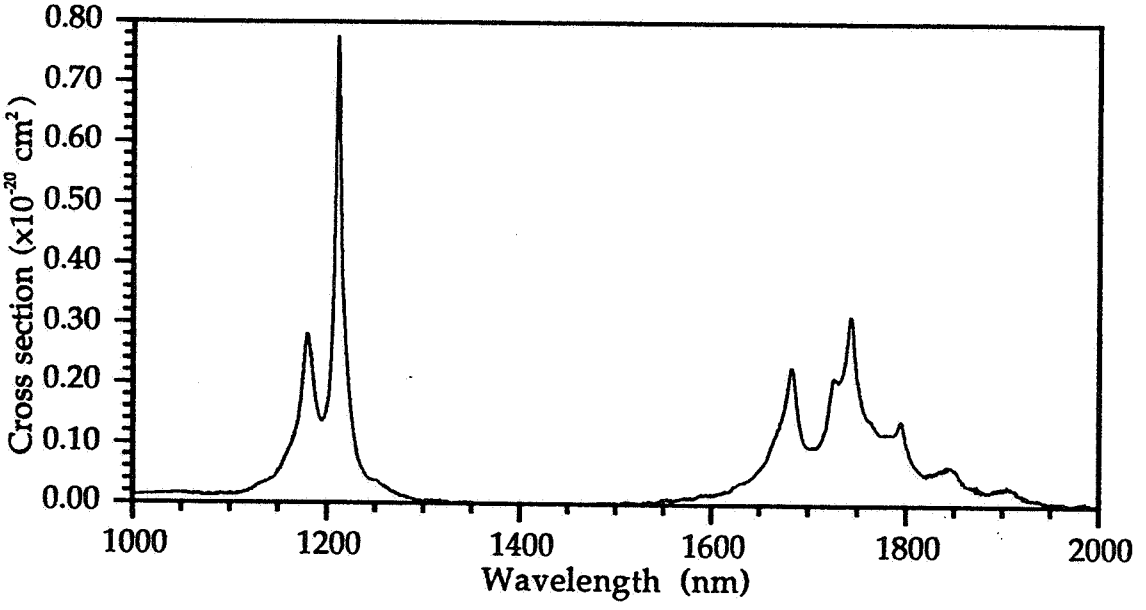

Figure 6-3b Infrared Absorption Spectrum in YLF:Tm σ-polarization

Table 6-2 Judd-Ofelt Fit for YLF:Tm

Transition from 5I8	$[U^{(2)}]^2$	$[U^{(4)}]^2$	$[U^{(6)}]^2$	λ(nm)	S meas. $x10^{-20}$ cm^2	S theor. $x10^{-20}$ cm^2
$^1D_2$	0	0.3156	0.0928	357	0.7209	0.7065
1G4	0.0483	0.0748	0.0125	469	0.2693	0.2371
3F2+3F3	0	0.3164	1.0992	672	1.7981	1.8047
3H4	0.2373	0.1090	0.5947	784	1.2633	1.2504
3F4	0.5375	0.7261	0.2382	1725	2.5347	2.5433

Judd-Ofelt Parameters: $\Omega_2 = 1.6673x10^{-20}$ $\Omega_4 = 1.9184x10^{-20}$ $\Omega_6 = 1.0897x10^{-20}$
Root Mean Square deviation: $\delta = .026938x10^{-20}$

Transition J->J'	wavelength λ(nm)	S theor. $x10^{-20}$ cm^2	A_{ED} (sec^{-1})	A_{MD} (sec^{-1})	branching ratio β	τ_{rad} (μs)
1D2 - 1G4	1486.3	0.675	79.18		0.006	
1D2 - 3F2	788.3	0.693	587.65		0.044	
1D2 - 3F3	745.2	0.401	387.33		0.029	
1D2 - 3H4	657.0	0.473	669.11		0.050	75
1D2 - 3H5	504.1	0.023	71.49		0.005	
1D2 - 3F4	450.4	1.143	5092.22		0.384	
1D2 - 3H6	357.1	0.702	6373.78		0.481	
1G4 - 3F2	1633.7	0.211	10.63		0.007	
1G4 - 3F3	1494.3	0.528	34.75		0.022	
1G4 - 3H4	1177.4	0.113	15.27		0.010	
1G4 - 3H5	762.8	0.755	377.59		0.244	645
1G4 - 3F4	646.2	0.729	602.71		0.389	
1G4 - 3H6	470.1	0.235	509.51		0.329	
3F2 - 3F3	17513.1	0.151	0.02		0.000	
3F2 - 3H4	4215.9	0.869	4.30		0.006	
3F2 - 3H5	1431.0	1.192	160.91		0.207	1289
3F2 - 3F4	1069.1	0.671	218.25		0.281	
3F2 - 3H6	660.0	0.281	392.29		0.506	
3F3 - 3H4	5552.5	1.082	1.49		0.001	
3F3 - 3H5	1558.4	1.708	127.39		0.084	
3F3 - 3F4	1138.6	0.185	35.61		0.023	660
3F3 - 3H6	685.9	1.532	1351.08		0.891	
3H4 - 3H5	2166.4	0.943	20.21		0.030	
3H4 - 3F4	1432.3	0.701	52.46		0.078	1480
3H4 - 3H6	882.5	1.302	603.06		0.892	
3H5 - 3F4	4226.5	1.373	3.06		0.023	
3H5 - 3H6	1225.0	1.316	129.05	46.0	0.977	5614
3F4 - 3H6	1725.0	2.499	106.66		1.000	9375

6.3 Emission Cross Sections in YLF:Tm

Emission spectra were taken for singly doped YLF:Tm. Thulium shows strong absorption in the range accessible by our diode lasers. The crystal was pumped with a 300mW diode laser operating at 785 nm. This wavelength corresponds to the $^3H_4$ manifold in YLF:Tm (see figures 5-2 and 5-3). Emission spectra were taken over both polarizations in the wavelength range 400 - 2200 nm, and then corrected for grating efficiency and detector response with a tungsten lamp source operating at 2854 °K.

The emission cross sections for YLF:Tm were calculated in the same way as was done for YLF:Ho (see chapter 5, section 3 for details). The energy level data needed for the calculation of the partition functions was found from [Du91]. Table 6-3 contains Boltzmann fractions for the Stark levels of the four lowest manifolds in YLF:Tm. The partition functions for each manifold appear at the bottom of the table. No fluorescence was detected from the $^3H_5$ manifold, so only the results for the $^3H_4$ and $^3F_4$ manifolds are presented in figures 6-4 and 6-5.

Table 6-3 Boltzmann Fractions in YLF:Tm @300K

Level#	Tm 3H6 Energy (cm^{-1})	Tm 3H6 Boltz. frac.	Tm 3F4 Energy (cm^{-1})	Tm 3F4 Boltz. frac.	Tm 3H5 Energy (cm^{-1})	Tm 3H5 Boltz. frac.	Tm 3H4 Energy (cm^{-1})	Tm 3H4 Boltz. frac.
1	0	0.19203	5599	0.29133	8284	0.16844	12599	0.18981
2	30	0.16630	5757	0.13655	8300	0.15600	12624	0.16836
3	30	0.16630	5757	0.13655	8300	0.15600	12643	0.15370
4	56	0.14680	5765	0.13141	8319	0.14241	12643	0.15370
5	270	0.05260	5820	0.10094	8501	0.05949	12745	0.09424
6	305	0.04447	5942	0.05623	8501	0.05949	12804	0.07101
7	319	0.04158	5968	0.04963	8519	0.05457	12835	0.06120
8	334	0.03870	5972	0.04869	8531	0.05152	12835	0.06120
9	334	0.03870	5972	0.04869	8534	0.05078	12891	0.04678
10	372	0.03225			8534	0.05078		
11	407	0.02727			8535	0.05054		
12	407	0.02727						
13	419	0.02574						
Part. func.	Z= 5.2074		Z= 3.4326		Z= 5.9369		Z= 5.2684	

C-2

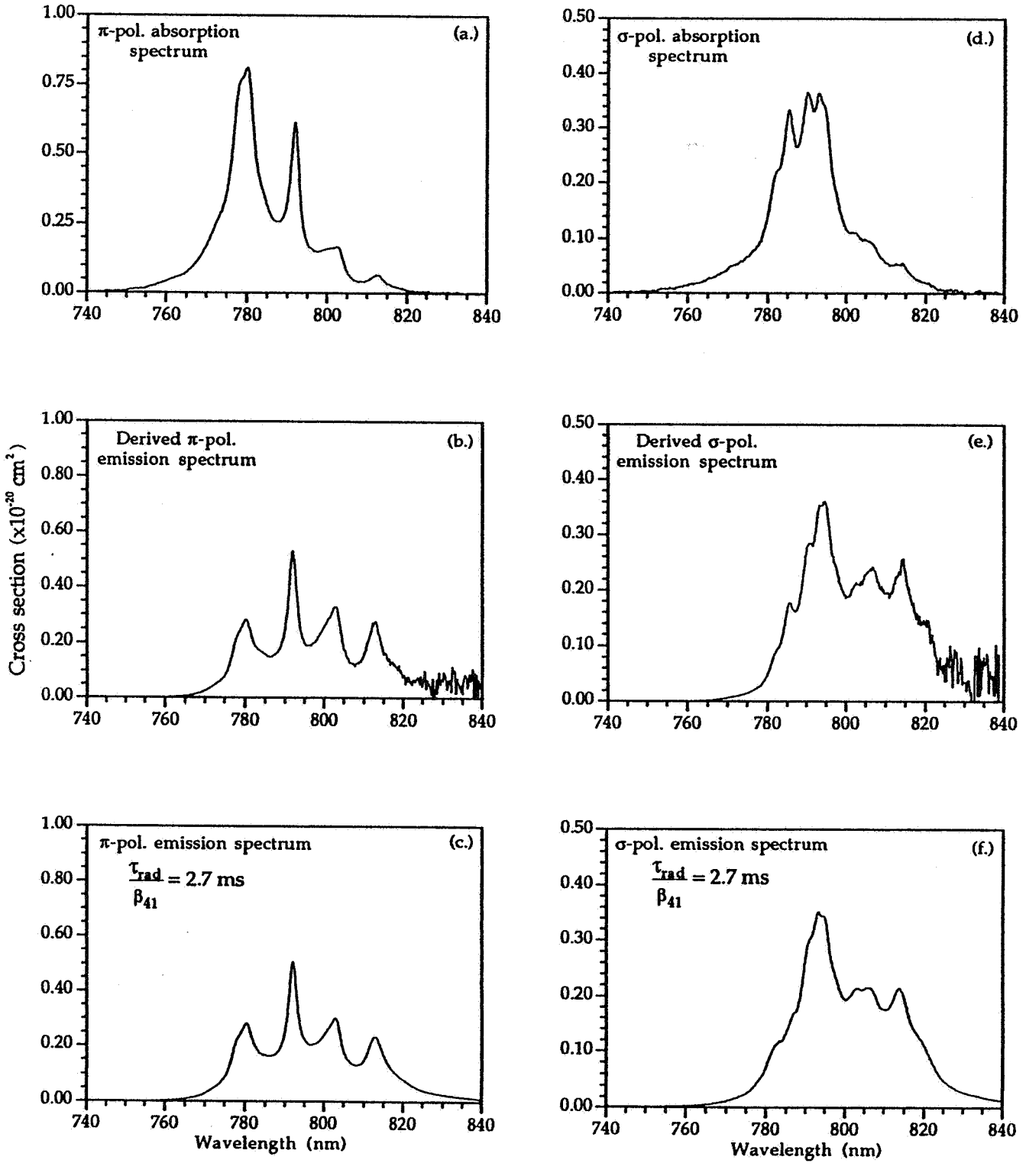

Figure 6-4 Cross Sections of the $^3H_4$ Manifold in YLF:Tm

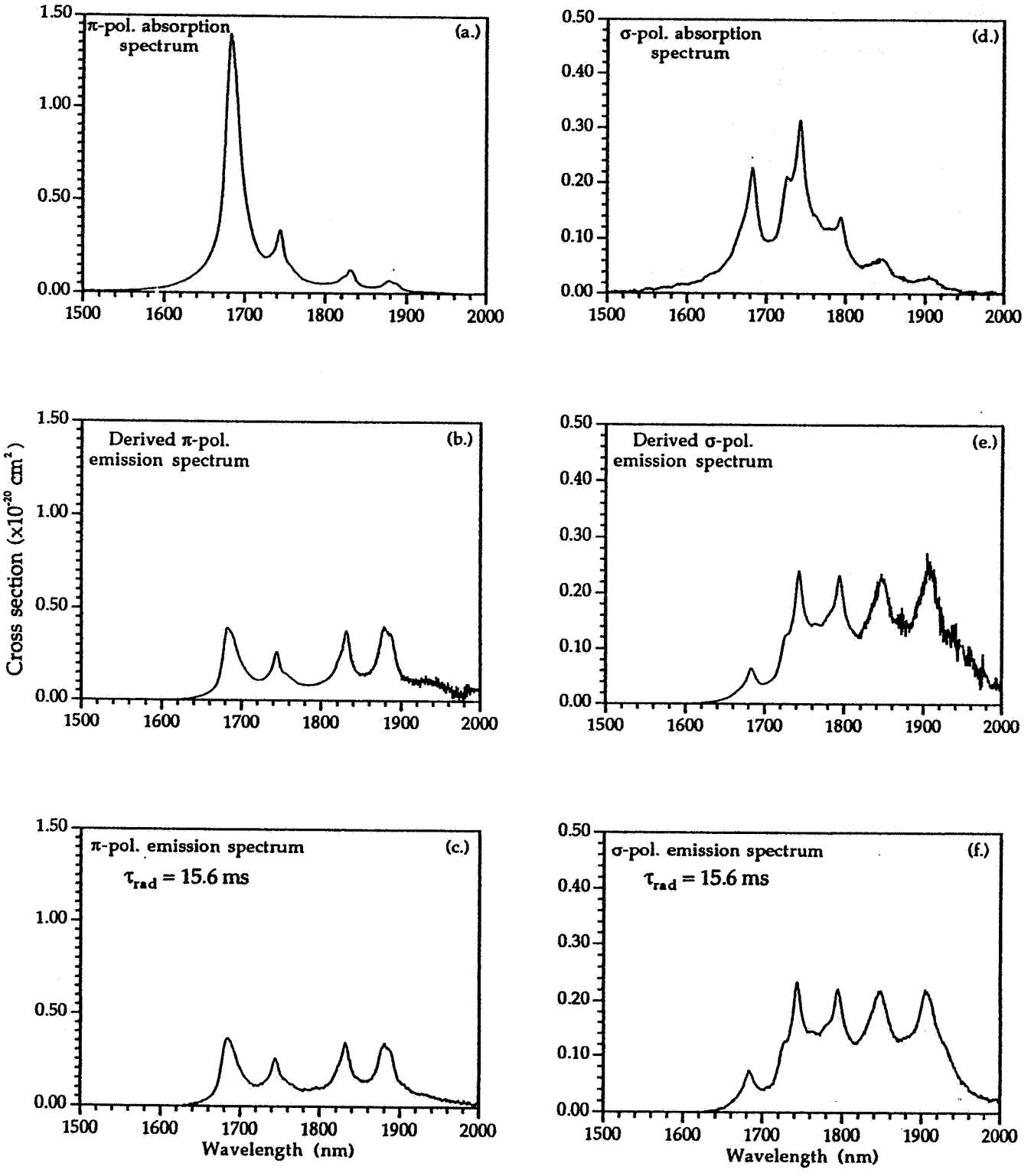

Figure 6-5 Cross Sections of the $^3F_4$ Manifold in YLF:Tm

6.4 Luminescence Decay in YLF:Tm

Crystals of singly doped YLF:Tm were excited using a Ti:Al_2O_3 (Titanium Sapphire) laser tuned to 780 nm, corresponding to the $^3H_4$ manifold (see figure 6-1). Emission was monitored with a Hewlett-Packard 54504A digitizing oscilloscope at 812 nm. The data was collected with the Labview software package. Emission was also monitored with a LeCroy CAMAC at 1.7μm for excitation at 780nm and 1.7μm. This data was collected with the LeCroy Catalyst software package. The details of the experimental apparatus used for these experiments was given in chapter 4.

The decay of Tm ions from the $^3H_4$ manifold exhibit a non-exponential decay behavior that strongly shortens with increasing Tm concentration. The shortening of the decay with increasing Tm concentration is a result of quenching via cross-relaxation. In this process an ion excited into the $^3H_4$ manifold interacts with a nearby ground state ion in $^3H_6$ and undergoes an exchange of energy, resulting in two ions in the $^3F_4$ manifold. The cross-relaxation mechanism, interpreted as the transfer Tm($^3H_4$ -> $^3F_4$);Tm($^3H_6$ -> $^3F_4$), is a phonon assisted transfer in the case of YLF since the gaps $^3H_4$ - $^3F_4$ = 5972 cm^{-1} and $^3F_4$ - $^3H_6$ = 6627 cm^{-1} exhibit no overlap.

Measurements of the decay from the $^3H_4$ manifold of Tm after excitation of the $^3H_4$ with a Ti:Al_2O_3 laser tuned to 780 nm were made on samples of Tm(.5) YLF, Tm(3) YLF, and Tm(12) YLF. The Tm(.5) YLF sample exhibited exponential decay with a decay time of 2000μs. The Tm(3) YLF and Tm(12) YLF samples were non-exponential in behavior and exhibited increasingly faster decay with increasing Tm concentration. The shortening of the decay is a result of the cross-relaxation process just discussed. In considering this process, we must also consider that the cross-relaxation can be enhanced by migration among the Tm $^3H_4$ ions described by the process Tm($^3H_4$ -> $^3H_6$);Tm($^3H_6$ -> $^3H_4$). The migration is usually treated as a diffusion process or a hopping process. In the diffusion process, the excitation makes many jumps between donors before being

deactivated by an acceptor. On the other hand, in the hopping process, the excitation makes a single jump in the vicinity of an acceptor and is subsequently deactivated by the acceptor. The diffusion approach is warranted if the average transfer time between donors is much greater than the transfer time between the donor and acceptor, whereas the hopping approach is warranted if the donor-donor transfer time is less than or equal to the donor-acceptor transfer time. These statements can be quantified in terms of the microscopic interaction parameters as: $C_{DD} << C_{DA}$ for diffusion migration and $C_{DD} \geq C_{DA}$ for hopping migration [Bo81]. In general, at low concentrations of active ions in the crystal the concept of defining a diffusion constant becomes problematic because of the variation of ion-ion transfer rates in different environments. In other words, the problem becomes more discrete in nature and the diffusion gradient cannot be defined. In such cases, the hopping model can be used.

The dopant ion concentrations used in this study are not extremely large, so the hopping mechanism is a likely choice for the interpretation of migration enhanced cross-relaxation. Before proceeding with this line of thought, however, there is a simple way to check whether the hopping interpretation is applicable in this case. The microscopic interaction parameters for the D->A and D->D transfer can be calculated easily using Dexter's theory [De53]. It should pointed out that the donors and acceptors in this case are the same ion, namely Tm, but we will still write the interaction parameters as C_{DA} to refer to cross-relaxation and C_{DD} to refer to migration.

The interaction parameter for energy transfer in Dexter's theory is:

$$C_{DX} = \frac{3\hbar^4 c^4 Q_X}{4\pi n^4 \tau_D} \int \frac{g_D^{em}(E) g_X^{abs}(E)}{E^4} dE \qquad (6\text{-}1)$$

where X=A for cross-relaxation and X=D for migration. The other terms in this equation have the usual meaning.

Calculating the overlap integral and integrated absorption cross section in eq. 6-1, we found the interaction parameters for the Tm-Tm cross-relaxation and migration to be:

$$C_{DA} = 3.7083 \times 10^{-47}\ cm^6/\mu s$$

$$C_{DD} = 1.2624 \times 10^{-45}\ cm^6/\mu s$$

Clearly, these values satisfy the relation $C_{DD} \geq C_{DA}$. So, our reasoning for the use of the hopping mechanism over diffusion is validated. We can now proceed to interpret the luminescence decay from the Tm $^3H_4$ in terms of a hopping migration assisted cross-relaxation model.

Burshtein [Bu72] is usually attributed with the initial development of the hopping mechanism of energy transfer, however, Artamonova's paper [Ar72] appeared in the same journal as Burstein's paper, but two months earlier. The paper by Artamanova is more lucid, so we will refer to his paper in the discussion that follows.

In the hopping model, the time dependence of the donor decay can be described by the equation:

$$\frac{n_D(t)}{n_D(0)} = \exp\left[-\frac{t}{\tau_0} - \gamma t^{1/2} - \overline{W}t\right] \qquad (6\text{-}2)$$

where τ_0 is the donor lifetime (radiative + nonradiative), γ is a term describing the Tm-Tm cross-relaxation, and $\overline{W}$ is a term describing the migration enhanced cross relaxation. The γ term for dipole-dipole interaction between ions is the same term that appears in the Förster-Dexter, Inokuti-Hirayama theories [De53, InHi65]. It is given by:

$$\gamma = \frac{4}{3}\pi^{3/2} N_A (C_{DA})^{1/2} \qquad (6\text{-}3)$$

The term describing the migration enhancement of the cross-relaxation was first derived in [Bu72, Ar72]. Under the assumption of a dipole-dipole interaction in the hopping mechanism this term is:

$$\overline{W} = \pi\left(\frac{2\pi}{3}\right)^{5/2} N_A N_D (C_{DA})^{1/2} (C_{DD})^{1/2} \qquad (6\text{-}4)$$

The addition of a term which takes into account the migration among donors provides a way for the excitations in the Tm $^3H_4$ to redistribute themselves randomly at some hopping rate τ_h^{-1}. This causes an enhancement of the cross-relaxation because excitations which are relatively isolated can migrate until they find a quenching center.

Equation 6-1 was fit to the experimental decay curves of the $^3H_4$ in samples of Tm(3)YLF and Tm(12)YLF. The results appear in table 6-4 along with the values found from Dexter's theory for comparison.

Table 6-4 Values of C_{DA} and C_{DD} in Tm YLF

	C_{DA} ($cm^6/\mu s$)	C_{DD}($cm^6/\mu s$)	C_{DD}/C_{DA}
Tm(3)YLF	$(3.7591\pm.0924)\times10^{-47}$	$(2.9091\pm.0100)\times10^{-45}$	0.0129
Tm(12)YLF	$(6.7532\pm.0268)\times10^{-47}$	$(4.0010\pm.0193)\times10^{-45}$	0.0168
Dexter Theory	3.7083×10^{-47}	1.2624×10^{-45}	0.0293

The fluorescence quantum efficiency can be found from the experimental decay curves by:

$$\eta_f = \frac{1}{\tau_r}\int_0^\infty [n_D(t)/n_D(0)]dt \qquad (6\text{-}5)$$

where τ_r is the radiative lifetime, taken to be 2400μs as found in section 6.3. Caird, et al. [Ca91] has integrated eq. 6-5 using eq. 6-2 as the integrand. The fluorescence quantum efficiency was found to be:

$$\eta_f = \frac{1/\tau_r}{(1/\tau_0 + \overline{W})}\left\{1 - \pi^{1/2} x \exp(x^2)[1 - \mathrm{erf}(x)]\right\} \qquad (6\text{-}6)$$

where τ_r is the radiative lifetime, τ_0 is the lifetime in the absence of cross-relaxation (radiative + nonradiative), and $x = \gamma / 2\sqrt{(1/\tau_0 + \overline{W})}$. The values for γ and $\overline{W}$ can be calculated from equations 6-3 and 6-4 using the values of the interaction parameters found in table 6-4. The value for τ_0 is taken to be 2000μs, the decay time in the low concentration Tm(.5)YLF sample. Based on the values calculated from the quantum efficiency, we can estimate the cross-relaxation time, since the quantum efficiency reflects the ratio of the mean decay time and the radiative time of decay. That is, we can write:

$$\tau_{cr} = \frac{\eta_f}{\left[\frac{1}{\tau_r} - \frac{\eta_f}{\tau_0}\right]} \qquad (6\text{-}7)$$

A tabulation of the results appears in table 6-5. Unfortunately, we do not have enough singly doped YLF:Tm samples to make an assessment of the concentration dependence of the cross-relaxation.

Table 6-5 Fluorescence Quantum Efficiencies in Tm YLF

	γ ($\mu s^{-1/2}$)	$\overline{W}$ (μs^{-1})	η_f	τ_{cr} (μs)
Tm(3)YLF	0.0188	0.0011	0.2388	803μs
Tm(12)YLF	0.0101	0.0284	0.0114	27.7μs

In contrast to YLF:Tm, crystals of YAG:Tm do not seem to exhibit migration enhancement of the cross-relaxation. The decay of the Tm $^3H_4$ manifold in YAG is well described by eq. 6-2 with $\overline{W} = 0$. This is the case of static cross-relaxation described in the Förster-Dexter, Inokuti-Hirayama theories. The interaction parameter for YAG:Tm was found to be on the order of 10^{-45} $cm^6/\mu s$. This is two orders of magnitude greater than in YLF:Tm, indicating that the interaction between ions for cross-relaxation is much stronger in YAG than in YLF. This is supported by observation of the decay curves of the Tm $^3H_4$ manifold in YAG and YLF. The lifetime in YAG quenches much faster with increasing Tm concentration than YLF. It seems to be the case, then, that migration among Tm ions can be neglected in YAG, but must be considered in YLF in order to correctly model the decay behavior.

References to chapter 6

[Ar72] M.V. Artamonova, CH. M. Briskina, A.I Burshtein, L.D. Zusman, and A.G. Skleznev, "Time Variation of Nd^{3+} Ion Luminescence and an Estimation of Electron Excitation Migration Among the Ions in Glass," Sov. Phys. JETP, **35** 457 (1972)

[Bo81] I.A. Bondar, et al. "Investigation of the processes of relaxation of electron excitation in crystals for arbitrary relationships between interaction parameters and concentrations of energy donors and acceptors," Sov. Phys. JETP **54**, 45 (1981)

[Br89] A. Brenier, J. Rubin, R. Moncorge and C. Pedrini, "Excited-state dynamics of the Tm^{3+} ions and Tm^{3+} -> Ho^{3+} energy transfers in $LiYF_4$," J. Phys. France **50**, 1463 (1989)

[Bu72] A.I. Burshtein,"Hopping Mechanism of Energy Transfer," Sov. Phys. JETP **35**, 882 (1972)

[Ca91] J.A. Caird, A.J. Ramponi, and P.R. Staver, "Quantum efficiency and excited-state relaxation dynamics in neodymium-doped phosphate laser glasses," J. Opt. Soc. **8**, 1391 (1991)

[De53] D.L. Dexter, "A Theory of Sensitized Luminescence in Solids," J. Chem. Phys. **21**, 836 (1953)

[Du92] M. Dulick, G.E. Faulkner, N.J. Cockroft and D.C. Nguyen, "Spectroscopy and dynamics of upconversion in Tm^{3+} YLF," J. Lumin. **48**, 517 (1992)

[InHi65] M. Inokuti, F. Hirayama, "Influence of Energy Transfer by the Exchange Mechanism on Donor Luminescence," J. Chem. Phys **43**, 1978 (1965)

[Je71] H.P. Jenssen, A. Linz, R.P. Leavitt, C.A. Morrison and D.E. Wortman, "Analysis of the optical spectrum of Tm^{3+} in $LiYF_4$," Phys. Rev. **B11**, 92 (1975)

CHAPTER 7
YLF: Tm,Ho - Results and Interpretation

Nature uses only the longest threads to weave her patterns, so that each small piece of her fabric reveals the organization of the entire tapestry.

Richard Feynman
The Character of Physical Law

7.1 Sensitized Luminescence in YLF: Tm,Ho

In the previous two chapters the focus centered on the spectroscopy and excitation dynamics of YLF crystals singly doped with either Thulium ions or Holmium ions. This chapter will concentrate on YLF systems co-doped with both Thulium and Holmium ions. Sensitized luminescence involves the initial excitation of a set of ions, termed sensitizers or donors (D), followed by the transfer of energy to other ions termed activators or acceptors (A), and the subsequent emission of light by acceptor ions. This description is very general, but represents many possible processes responsible for the transfer of energy from donor to acceptor. These include resonant transfer, non-resonant transfer, cross relaxation and upconversion. The 2.0μm laser emission from diode pumped Thulium sensitized Holmium has been the subject of numerous studies for various crystal hosts. Two of the most popular host materials studied have been $Y_3Al_5O_{12}$ (YAG) [Fa87, Fa88, Km94], and $LiYF_4$ (YLF) [He89, Es90, Bu92, St93]. It is, therefore, useful to examine some of the spectroscopic features of diode pumped YLF:Tm,Ho.

YLF:Tm,Ho crystals were excited with a diode laser operating at 785 nm, corresponding to the $^3H_4$ manifold in Thulium. Emission from the crystals was monitored from 300-2300 nm. The transitions that were observed under these excitation conditions is pictured in Figure 7-1. The striking feature of this figure is the plethora of transitions that result from pumping one manifold in Thulium. Based on the values for the range of

transitions of YLF:Ho in Table 5-1a and YLF:Tm in Table 6-1a, the following assignments of the numbered transitions in figure 7-1 were made. Figure 7-2 shows the scaled emission spectra depicting the relative strengths of these transitions.

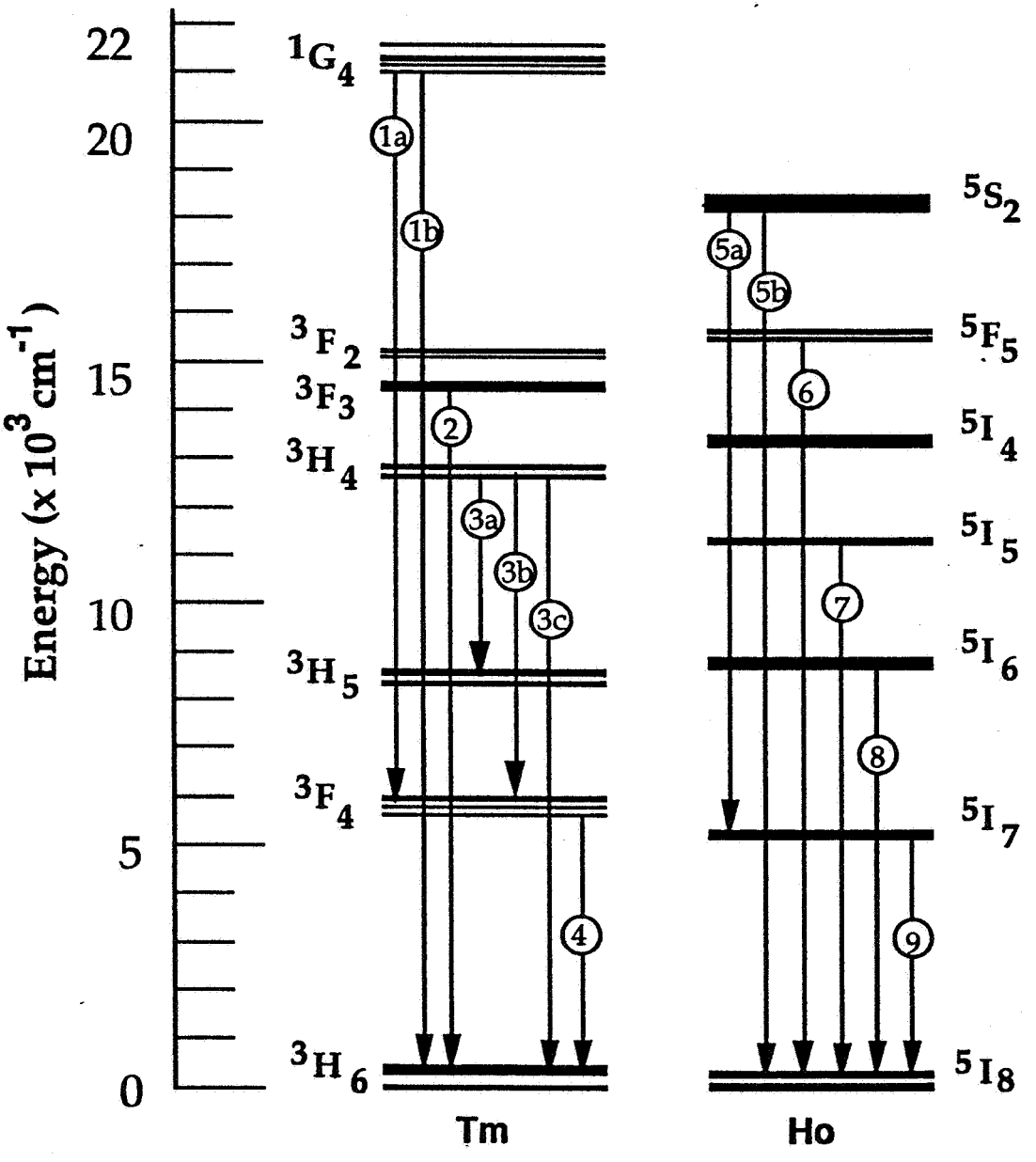

Figure 7-1 Observed Transitions in YLF:Tm,Ho Exciting the Tm $^3H_4$ @785 nm

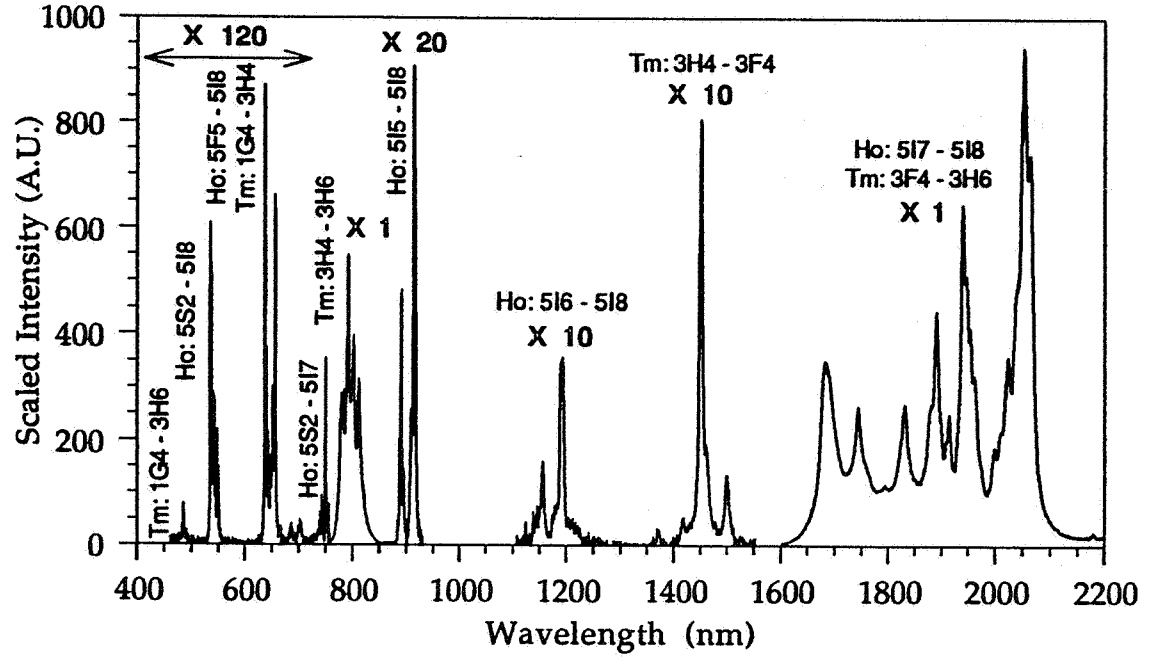

Figure 7-2a π-pol. Emission Spectra of YLF:Tm,Ho Exciting Tm $^3H_4$ @785 nm

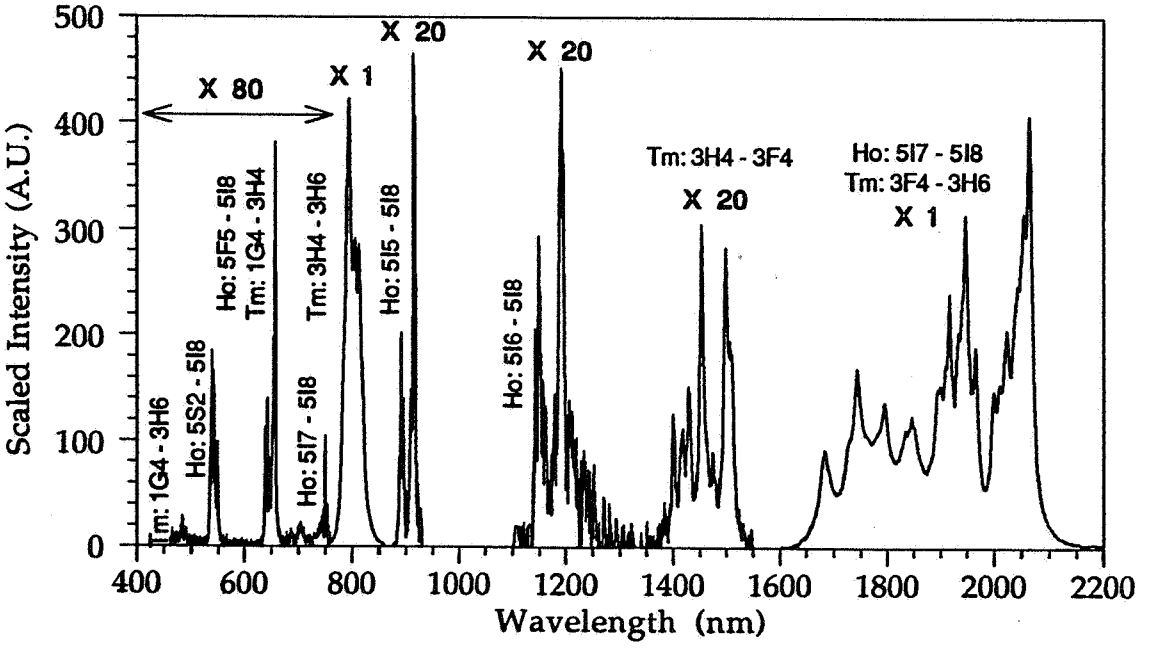

Figure 7-2b σ-pol. Emission Spectra of YLF:Tm,Ho Exciting Tm $^3H_4$ @785 nm

1a.) Tm: $^1G_4$ -> $^3F_4$ (626-666 nm)
1b.) Tm: $^1G_4$ -> $^3H_6$ (463-486 nm)
2.) Tm: $^3F_3$ -> $^3H_6$ (684-708 nm)
3a.) Tm: $^3H_4$ -> $^3H_5$ (2170-2460 nm)
3b.) Tm: $^3H_4$ -> $^3F_4$ (1371-1508 nm)
3c.) Tm: $^3H_4$ -> $^3H_6$ (779-818 nm)
4.) Tm: $^3F_4$ -> $^3H_6$ (1889-2066 nm)
5a.) Ho: $^5S_2$ -> $^5I_7$ (730-750 nm)
5b.) Ho: $^5S_2$ -> $^5I_8$ (539-550 nm)
6.) Ho: $^5F_5$ -> $^5I_8$ (638-659 nm)
7.) Ho: $^5I_5$ -> $^5I_8$ (882-915 nm)
8.) Ho: $^5I_6$ -> $^5I_8$ (1136-1196 nm)
9.) Ho: $^5I_7$ -> $^5I_8$ (1693-1924 nm)

It is obvious from these observations that the YLF:Tm,Ho system presents a formidable problem toward understanding the modes of excitation and interaction of the various manifolds. The complexity of some of these processes precludes a rigorous analysis of the available experimental data. When this is the case, a more prudent approach to the interpretation of the data is to resort to a descriptive study of the phenomena. No attempt will be made here to entirely explain all of the observed features, but given a set of suitably designed experiments some insight can be gained toward this goal. It will be helpful to make some descriptive observations concerning Figure 7-1.

The transitions pictured in figure 7-1 for YLF:Tm,Ho were the only ones observed in the range 300-2300 nm. The only two manifolds that were found to show no luminescence were the Ho $^5I_4$ and the Tm $^3H_5$. In the case of the Ho $^5I_4$ this can be explained by its very small electric dipole transition probability (see table 5-2) and the small energy gap to the next lower lying manifold. Its primary channel of de-excitation is nonradiative and no optical radiation would be expected. In the case of the $^3H_5$ the most likely explanation is the following. The energy gap from the $^3H_4$ to the $^3H_5$ is large, precluding any substantial excitation of the $^3H_5$ from nonradiative decay of the $^3H_4$. The

feeding of the $^3H_5$ from the $^3H_4$ through optical means accounts for only 3% of the total $^3H_4$ luminescence, as can be seen from the branching ratio in table 6-2. The low population in the $^3H_5$ in conjunction with a small energy gap to the next lower lying manifold, and a moderately large radiative lifetime would lead to very little luminescence. This situation is exacerbated further at higher Tm concentrations where de-excitation of the $^3H_4$ manifold is dominated by cross relaxation to $^3F_4$. This explanation assumes that the $^3H_5$ is not substantially populated by any energy transfer processes.

One striking feature about Figure 7-1 is that more than half of the observed transitions originate above the pump manifold. This is indicative of upconversion processes. This conclusion is supported by observing the change in intensity of the transitions in these manifolds as a function of pump power. Exciting the $^3H_4$ manifold with a diode laser operating at 785 nm, the intensity of the Ho $^5S_2$ @550 nm, Ho $^5I_5$ @890 nm, Ho $^5I_7$ @2.06 μm, and Tm $^1G_4$ @ 485 nm, Tm $^3H_4$ @812 nm, Tm $^3F_4$ @1.7 μm were measured as a function of absorbed power by varying the laser diode pump power from100% to 5%. The results of these measurements for a Tm(4)Ho(.5) YLF crystal are shown in figure 7-3.

Three types of behavior were seen. The intensity followed either linear, super linear, or sublinear change with absorbed power. Referring to figure 7-3, it can be seen that the Ho $^5S_2$, Ho $^5I_5$, and Tm $^1G_4$ exhibit super linear behavior, the Tm $^3H_4$ exhibits linear behavior, and the Ho $^5I_7$, Tm $^3F_4$ exhibit sublinear behavior. The Tm $^3H_4$ behavior is as expected since the pump band reflects only the linear change in intensity with pump power. The change in intensity of the Ho $^5S_2$, Ho $^5I_5$, and Tm $^1G_4$ with absorbed power reflect a gain in the population as a result of upconverted energy into the manifold. The Ho $^5I_7$ and Tm $^3F_4$ reflect a loss in the population with absorbed power as a result of a depletion of energy, suggesting that these manifolds give up energy to support direct energy transfer processes and upconversion processes.

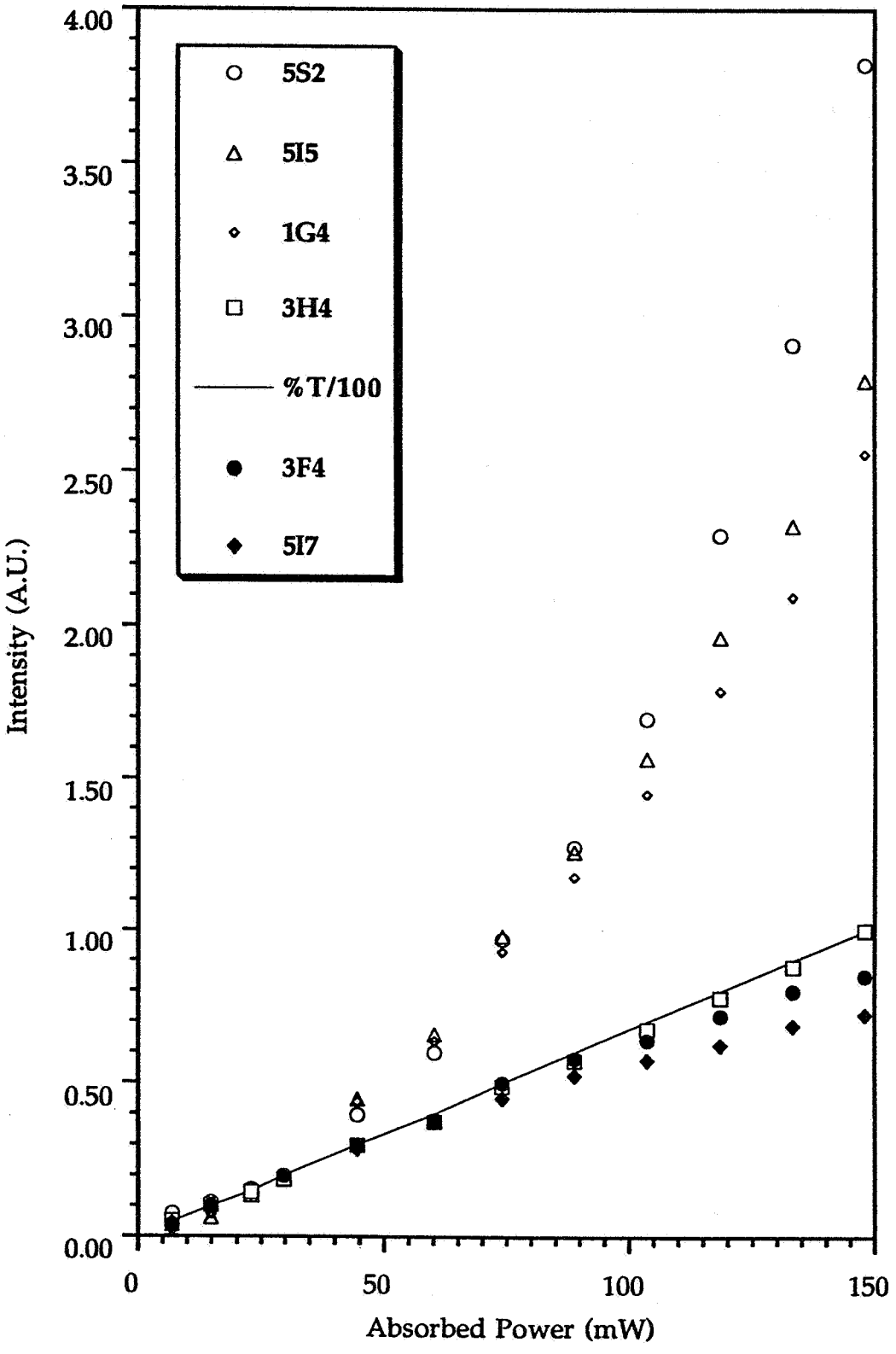

Figure 7-3 Luminescence Intensity vs. Absorbed Power in YLF:Tm(4)Ho(.5)

The task of identifying the channels of these energy transfer processes is a difficult one which is far from being solved. Ideally, the best method of approach would be to excite many different manifolds and observe the luminescence and decay characteristics of the various other manifolds under different pumping conditions and over a range of temperatures. Such experiments should also be done with a suitable range of dopant ion concentrations. Only in this way can a comprehensive and thorough analysis be done that leads to solid conclusions. In practice, this is not always possible due to constraints on the availability of the necessary apparatus. Therefore, a reliance on studies available in the literature in conjunction with ones own studies must serve as a basis for any conclusions that are made.

A number of emission spectra under diode pumping of the Tm $^3H_4$ of YLF:Tm,Ho crystals with various dopant ion concentrations and identical path lengths along the pump direction have been examined. Based on these emission spectra, the following observations can be made concerning the change of the intensity of the emission with dopant ion concentration:

1.) Ho $^5S_2$ intensity decreases with increasing Ho concentration and decreases with increasing Tm concentration
2.) Ho $^5F_5$ intensity increases with increasing Ho concentration and increases with increasing Tm concentration
3.) Ho $^5I_5$ intensity decreases with increasing Ho concentration and increases with increasing Tm concentration
4.) Ho $^5I_6$ intensity decreases with increasing Ho concentration.
5.) Ho $^5I_7$ intensity increases with increasing Ho concentration.
6) Tm $^1G_4$ intensity increases with increasing Ho concentration.
7.) Tm $^3F_2$,$^3F_3$ intensity decreases with increasing Ho concentration and decreases with increasing Tm concentration
8.) Tm $^3H_4$ intensity decreases with increasing Tm concentration and is independent of Ho concentration.
9.) Tm $^3F_4$ intensity decreases with increasing Ho concentration and increases with increasing Tm concentration.

These observations are general statements on the observed behavior of the intensity of the luminescence of various manifolds in the YLF:Tm,Ho system under excitation of the $^3H_4$ manifold of Tm. The actual behavior may be more subtle and depend on the ratio of the concentrations. At any rate we can attempt to draw some conclusions, based on these observations, regarding how these manifolds become populated.

Exciting the $^3H_4$ manifold of Tm produces luminescence from the this manifold that decreases with increasing Tm concentration. This is explained by the interaction of a Tm ion in an excited $^3H_4$ state with a ground state ion in the $^3H_6$ state, resulting in an exchange of energy that produces two ions in the $^3F_4$ state. This process is known as cross-relaxation and can be referred to by the notation $Tm(^3H_4->^3F_4);Tm(^3H_6->^3F_4)$. Observations eight and nine corroborate this interpretation because as the Tm concentration is increased the interaction among the Tm ions increases. The cross-relaxation process works towards depleting the $^3H_4$ in favor of populating the $^3F_4$. Thus, as Tm concentration is increased, the $^3H_4$ intensity decreases while the $^3F_4$ intensity increases. These are exactly observations eight and nine. This is valid for both singly doped YLF:Tm and YLF:Tm,Ho. With the addition of Holmium, however, energy transfer from the Thulium to the Holmium ions becomes possible. In observation nine we noted that the intensity of the Thulium luminescence from $^3F_4$ decreased with Holmium concentration, indicating that ions in the $^3F_4$ interact with Ho ions and exchange energy, depleting $^3F_4$ states and populating Ho states.

One such channel of energy transfer involves direct transfer from Tm $^3F_4$ to the Ho $^5I_7$, $Tm(^3F_4->^3H_6);Ho(^5I_8->^5I_7)$, in which an excited $^3F_4$ ion drops to the $^3H_6$ ground state and a Ho ion is excited from the $^5I_8$ ground state to the excited $^5I_7$ state. This is supported by the decay kinetics of these two manifolds. When exciting the $^3F_4$ manifold, this manifold shows an initial fast decay (tens of microseconds), followed by a long decay (thousands of microseconds) when looking at the $^3F_4$ emission. When looking at the $^5I_7$ emission, an initial fast rise is seen, followed by a long decay equal to the long decay of

the $^3F_4$ emission. This behavior will be explained in more detail later. At this point we are only concerned with the qualitative behavior. The Tm $^3F_4$->Ho $^5I_7$ energy transfer is the first step from which all other Ho manifolds become populated.

For instance, Fan et al. [Fa88] has postulated that the luminescence in the Ho $^5I_5$ results from the upconversion process Tm($^3F_4$->$^3H_6$);Ho($^5I_7$ ->$^5I_5$). This seems to be in agreement with observations three and nine. Since the $^3F_4$ emission increases with Tm concentration then the $^5I_5$ emission would be expected to increase also with increasing Tm since there are more excited ions in the $^3F_4$ state available for upconversion. Also, if this upconversion is present then a sublinear rise in intensity of the $^5I_7$ emission with absorbed power and a super linear rise in intensity of the $^5I_5$ emission with absorbed power would be expected. This is, in fact, the case as evidenced by figure7-2.

Tyminski, et al. [Ty89] has attributed the $^5S_2$ luminescence as resulting from the upconversion process Tm($^3H_4$->$^3H_6$);Ho($^5I_7$ ->$^5S_2$). Unlike the $^5I_5$ luminescence, the $^5S_2$ emission decreases with increasing Tm concentration (observation one). Since the $^3H_4$ emission decreases with Tm concentration, then the $^5S_2$ emission would be expected to also decrease with increasing Tm because there are less excited ions in the $^3H_4$ state (due to cross relaxation to the $^3F_4$) available for upconversion. Like the $^5I_5$, the $^5S_2$ intensity shows a super linear rise with absorbed pump power.

There has been some controversy regarding the importance of these upconversion processes with regards to depletion of the metastable $^5I_7$ laser level. A depletion of the population in the laser level decreases the 2μ laser output by increasing the threshold (the condition regarding the required population inversion for lasing to occur) [Sv82]. It has generally been assumed that the $^5S_2$ upconversion is unimportant [Fa87, Ki87], but no justification for this assumption has been presented. Figures 7-2 show the relative intensities of the emission from a sample of Tm(4)Ho(.5)YLF by exciting the $^3H_4$ manifold with a diode laser. As can be seen from these figures, the intensity of the $^5S_2$ emission is 100 times smaller than the $^5I_7$ emission, while the $^5I_5$ emission is only about

10 times smaller. A possible explanation for this could be that the $^5S_2$ does not have as large a population as the $^5I_5$. This would seem to indicate that the $^5S_2$ upconversion is less significant than the $^5I_5$ upconversion in depleting the $^5I_7$ laser level. On the other hand, the nonradiative decay could also play a part in deactivating the $^5S_2$.

7.2 Luminescence Decay in YLF:Tm,Ho

Many measurements have been made of the temporal decay in YLF:Tm,Ho with different Tm and Ho dopant concentrations under different excitation wavelengths. These measurements are very useful for identifying the channels of energy transfer and determining the rates at which they occur. For instance, measuring the decay time of a particular manifold in singly doped YLF:Tm and YLF:Ho and then measuring the decay of the same manifold in the co-doped sample can indicate the presence of energy transfer or trapping of energy by observing the shortening or lengthening of the decay time.

Two laser excitation sources were used to measure the temporal behavior in co-doped YLF:Tm,Ho. The Ti:Al_2O_3 was tuned to 785nm exciting the $^3H_4$ manifold of Tm and tuned to 890nm exciting the $^5I_5$ manifold of Ho. The $CoMgF_2$ laser was tuned to 1.75μm to excite the $^3F_4$ manifold of Tm and tuned to 1.96μm to excite the $^5I_7$ manifold of Ho. Using these two excitation sources we were able to selectively excite the above indicated manifolds and observe the decay of the fluorescence emitted by ions in various manifolds. The wavelength selection of the fluorescence was achieved with the use of narrow band filters when exciting with the $CoMgF_2$ laser, and with a spectrometer when exciting with the Ti:Al_2O_3 laser. The reason for this is that the energy of the $CoMgF_2$ beam was 6mJ while the beam energy of the Ti:Al_2O_3 was 25mj. With the low energy of the $CoMgF_2$ laser it was necessary to use filters to get sufficient signal. The use of filters has the drawback that while much more signal is observed there is always some leakage of scattered light from the pump beam which can mix with the fluorescence signal. This is undesirable so all attempts were made to keep this to a minimum. No preamplifiers were

used to minimize signal distortion and a 50Ω resistor was used to terminate the signal to the CAMAC to eradicate the RC time constant. Before proceeding, it should also be mentioned that the pulse length of the $CoMgF_2$ laser was measured to be 480ns and the pulse length of the Ti:Al_2O_3 laser was <100ns.

The remainder of this chapter will be concerned with analyzing some of the energy transfer processes in detail by modeling the decay behavior.

7.2.1 Cross-Relaxation Ho($^5I_5$->$^5I_7$);Tm($^3H_6$ ->$^3F_4$) in YLF:Tm,Ho

The decay of the $^5I_5$ manifold in singly doped YLF:Ho has already been presented in chapter 5. Figure 5-7 shows the decay of the Ho $^5I_5$, Ho $^5F_5$, and the Ho $^5S_2$ resulting from excitation of the Ho $^5I_5$ at 890nm. From these measurements, the natural decay time of the Ho $^5I_5$ was found to be 20μs. In systems co-doped with Tm, however, the decay becomes non-exponential and the lifetime is found to be shortened. It seems evident that there is an interaction between Tm ions and ions in the excited Ho $^5I_5$ manifold. The most likely process is the cross relaxation process Ho($^5I_5$->$^5I_7$);Tm($^3H_6$ ->$^3F_4$), which is a reverse process to the upconversion Tm($^3F_4$->$^3H_6$);Ho($^5I_7$ ->$^5I_5$) mentioned earlier. The cross relaxation process is pictured in figure 7-4.

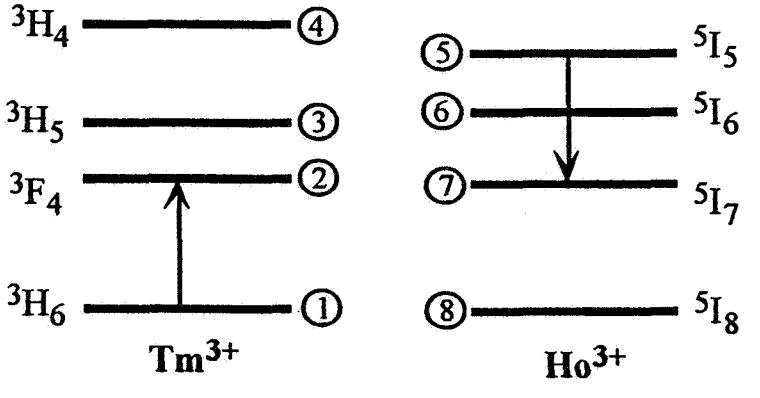

Figure 7-4 Illustration of the Cross-relaxation Process Ho($^5I_5$->$^5I_7$);Tm($^3H_6$ ->$^3F_4$)

The decay of the Ho $^5I_5$ was measured for several co-doped samples with different Ho and Tm concentrations. Figure 7-5 shows a representative decay of the Ho $^5I_5$ at 912nm for excitation at 890nm. In this case Ho(.5)YLF and Tm(5)Ho(.5)YLF are pictured. As can be seen in this figure, the shortening of the lifetime is obvious.

For each co-doped sample, the decay curve was fit to a series of exponentials using the Kaleidagraph™ data analysis/graphics application. It was found that a good fit was obtained with two exponentials. Table 7-1 tabulates the results of the fitting. The time-dependent fluorescence of the co-doped materials shows an initial quick exponential decay (~ 2 – 4 μs) followed by a slightly longer exponential decay (~ 11 – 14 μs).

We would like to be able to extract a rate constant for this process. Toward this end, we take a rate equation approach and write the rate of change of the Ho $^5I_5$ population as:

$$\frac{dn_5}{dt} = -\frac{n_5}{\tau_5} - p_{51}n_5n_1 + p_{27}n_2n_7 \qquad (7\text{-}1)$$

Table 7-1 Components of Ho $^5I_5$ Decay @912 nm for Ho $^5I_5$ Excitation @890 nm

	$n(t)/n(0) = A_1\exp(-t/\tau_1) + A_2\exp(-t/\tau_2)$				
Sample	A_1	τ_1	A_2	τ_2	Integrated time (μs)
Ho(0.5)YLF	1.0000	20.0	—	—	20.0
Tm(4)Ho(0.5)YLF	0.5698	2.67	0.4543	13.16	7.47
Tm(4)Ho(1.0)YLF	0.3938	1.71	0.6338	11.92	8.25
Tm(5)Ho(1.5)YLF	0.4227	2.75	0.5788	11.81	7.96
Tm(5)H0(0.5)YLF	0.5587	3.89	0.4329	13.43	7.94
Tm(6)Ho(1.0)YLF	0.6294	3.61	0.3540	11.58	5.98
Tm(1)Ho(12)YLF	0.4753	66.5	0.4712	518	280

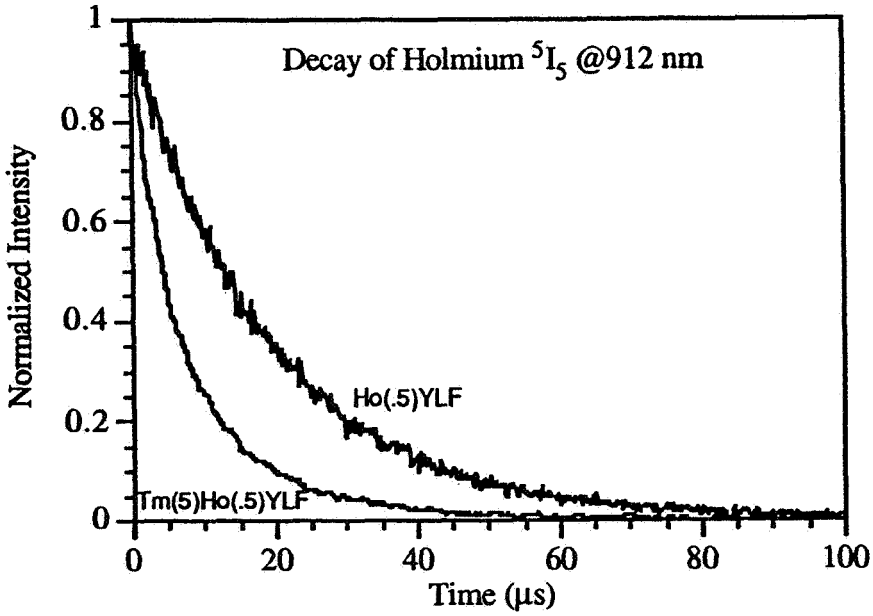

Figure 7-5 Representative Decay of Ho $^5I_5$ under Ho $^5I_5$ excitation.

The subscript numbers refer to a particular manifold as indicated in figure 7-4. The first term in this equation refers to the natural decay of the Ho $^5I_5$ manifold. The other terms account for the interaction of the manifolds participating in the process. In this case p_{51} is the rate constant of the cross relaxation Ho($^5I_5$->$^5I_7$);Tm($^3H_6$ ->$^3F_4$) and p_{27} is the rate constant of the upconversion Tm($^3F_4$->$^3H_6$);Ho($^5I_7$ ->$^5I_5$). Considering only the manifolds participating in these processes, we can write the ground state populations as $n_1 = C_{Tm}N - n_2$, and $n_8 = C_{Ho}N - n_5 - n_7$. This is just a statement of conservation of Tm and Ho ions. C_{Tm} is the concentration of Tm ions and N is the density of Y^{3+} sites in YLF. Using these expressions in eq. 7-1 and neglecting all nonlinear terms, that is terms which are a product of populations, we find that:

$$\frac{dn_5}{dt} = -\frac{n_5}{\tau_5} - p_{51}C_{Tm}Nn_5 \qquad (7\text{-}2)$$

Neglecting the non-linear terms is a rather drastic assumption, but it is one which may not be too bad considering that the manifold which is being excited in the situation we are studying is the Ho $^5I_5$. It will initially have a large population relative to the other manifolds in the system and the non-linear terms will be unimportant. At later times, however, this assumption could drastically breakdown as the other manifolds also become populated. We will assume that the assumption holds fairly well and proceed. Equation 7-2 is easily solved. The solution is:

$$\frac{n_5(t)}{n_5(0)} = A\exp\left[-\frac{t}{\tau_5} - p_{51}C_{Tm}Nt\right] \qquad (7\text{-}3)$$

This equation was fit to several Ho $^5I_5$ decay curves with p_{51} as the fitting parameter. τ_5 is known from measurements of singly doped YLF:Ho. The value of τ_5 was given in table 7-1 as 20μs. The results of the fitting appear in table 7-2

Table 7-2 Rate Constants For Cross Relaxation Ho($^5I_5$->$^5I_7$);Tm($^3H_6$ ->$^3F_4$)

	$\frac{n_5(t)}{n_5(0)} = A\exp\left[-\frac{t}{\tau_5} - p_{51}C_{Tm}Nt\right]$	
Sample	A	p_{51} ($cm^3/\mu s$)
Tm(4)Ho(0.5)YLF	0.8598	1.4043×10^{-22}
Tm(4)Ho(1.0)YLF	0.8326	1.0322×10^{-22}
Tm(5)Ho(1.5)YLF	0.8753	1.2077×10^{-22}
Tm(5)H0(0.5)YLF	0.8973	1.0403×10^{-22}
Tm(6)Ho(1.0)YLF	0.8680	1.3449×10^{-22}
Average	0.8666	1.2058×10^{-22}

It should be pointed out that the cross-relaxation process discussed here is not the only possible explanation of the Ho $^5I_5$ decay in co-doped systems. It is only a possible explanation supported by the fact that the energy transfer is resonant, that is, the participating levels overlap in energy (see tables 5-1 and 6-1 for range of transitions), and by the fact that the decay in Ho is exponential, eliminating an explanation based on interactions between Holmium ions in other states (see figure 5-7). The opposite process to the one described here, that is the upconversion Tm($^3F_4$->$^3H_6$);Ho($^5I_7$ ->$^5I_8$), will be discussed next.

7.2.2 Upconversion Tm($^3F_4$->$^3H_6$);Ho($^5I_7$ ->$^5I_5$) in YLF:Tm,Ho

In section 7-1 we showed that there are several upconversion processes which may affect the laser performance of the 2μm laser in Tm,Ho systems. The upconversion process which may have the most deleterious affect on these systems has been identified as Tm($^3F_4$->$^3H_6$);Ho($^5I_7$->$^5I_5$), in which an excited Tm $^3F_4$ ion interacts with an excited Ho $^5I_7$ ion. The Tm $^3F_4$ ion decays back to the ground state and the Ho $^5I_7$ ion is excited to the Ho $^5I_5$. This process is illustrated in figure 7-6 The excitation in the $^5I_5$ then decays back to the lower manifolds through the emission of phonons with a quantum efficiency that is near one.

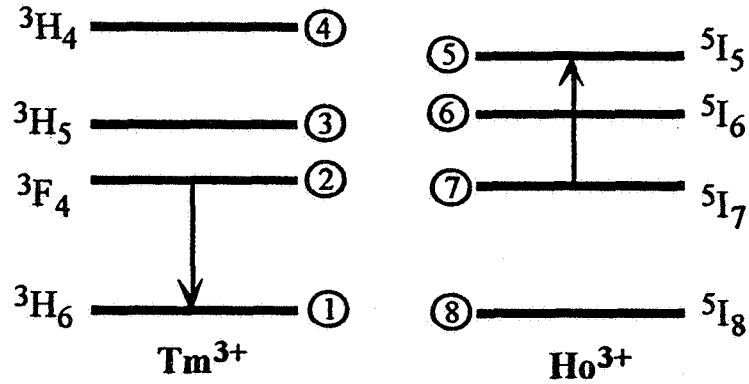

Figure 7-6 Illustration of the Upconversion Process $Tm(^3F_4 \rightarrow ^3H_6);Ho(^5I_7 \rightarrow ^5I_5)$

We would like to be able to measure the rate of this upconversion. Toward this end, a simplified rate equation model can be utilized. It will be useful to make some observations regarding the Tm,Ho system, when exciting the Tm $^3H_4$ manifold, to simplify the analytic equations governing the rate of change of the populations in the lower manifolds. One observation can be made from measurements of the upper state lifetimes in the Tm $^3F_4$ and Ho $^5I_7$ manifolds. Regardless of the Tm and Ho concentrations the upper state lifetimes in these two manifolds are the same. The lifetimes of these manifolds are very long compared to the time for the energy transfer from the Tm $^3F_4$ to the Ho $^5I_7$, so a state of quasi-thermal equilibrium is established between these manifolds. This results in a great simplification of the problem because the two upper states can be treated as a coupled system, and the relative populations of each Tm and Ho ion can be calculated from a Boltzmann distribution over the individual Stark levels. The fractional population f_{Tm} in the Tm $^3F_4$ and f_{Ho} in the Ho $^5I_7$ can be expressed as [Ca75]:

$$f_{Tm} = \frac{C_{Tm}\sum_i g_i e^{-E_i/kT}}{C_{Tm}\sum_i g_i e^{-E_i/kT} + C_{Ho}\sum_j g_j e^{-E_j/kT}} \qquad (7\text{-}4)$$

$$f_{Ho} = \frac{C_{Ho}\sum_{j} g_j e^{-E_j/kT}}{C_{Tm}\sum_{i} g_i e^{-E_i/kT} + C_{Ho}\sum_{j} g_j e^{-E_j/kT}} \qquad (7\text{-}5)$$

The ion concentration of Ho is C_{Ho} and the ion concentration of Tm is C_{Tm}. The sums over i and j are over Stark levels of the Tm $^3F_4$ and Ho $^5I_7$, respectively. These sums are the partition functions for the manifolds, and have already been calculated (see table 5-3 and table 6-3). The degeneracy of a given Stark level is taken into account by g_i and g_j. The energy of the Stark levels are E_i and E_j.

Since the Ho $^5I_7$ and the Tm $^3F_4$ upper states can be treated as a coupled system, we can write down the rate equation for such a coupled system as [Fa88]:

$$\frac{dN_u}{dt} = R_p - \frac{N_u}{\tau} - qN_{Ho}N_{Tm} + q\frac{\eta_a}{2}N_{Ho}N_{Tm} \qquad (7\text{-}6)$$

where $N_u=N_{Ho}+N_{Tm}$ represents the population of the coupled system and τ represents the coupled lifetime (the lifetime of the Ho $^5I_7$ or the Tm $^3F_4$). Now, this balance equation can be understood in the following way. The rate of change of the population in the coupled system is equal to the pump rate R_p (number of photons per second entering the coupled system within the pump volume of the crystal), minus the excitations lost through spontaneous emission (the 2nd term), minus the excitation lost through upconversion from the interaction of the Tm and Ho upper states (the 3rd term characterized by a an upconversion coefficient q), plus the excitations that return from decay of the $^5I_5$ (the 4th term which includes η_a as the quantum efficiency for the relaxation to return to the Ho $^5I_7$ and Tm $^3F_4$).

Now, we can write N_{Ho} and N_{Tm} in terms of N_u and the fractional populations f_{Ho} and f_{Tm}. Since $N_u=N_{Ho}+N_{Tm}$ then it follows that $N_{Ho}=f_{Ho}N_u$ and $N_{Tm}=f_{Tm}N_u$. The balance equation 7-6 now becomes very simple:

$$\frac{dN_u}{dt} = R_p - \frac{N_u}{\tau} - q\left(1 - \frac{\eta_a}{2}\right) f_{Ho} f_{Tm} N_u^2 \qquad (7\text{-}7)$$

For a system in steady state this equation is easily solved. The result is:

$$N_u = \frac{1}{q\tau f_{Ho} f_{Tm}}\left(\sqrt{1 + 2qR_p f_{Ho} f_{Tm} \tau^2} - 1\right) \qquad (7\text{-}8)$$

A series of experiments have been performed on a number of YLF:Tm,Ho crystals that measure the change in intensity of the Ho $^5I_7$ intensity with absorbed pump power. A 250 mW diode laser operating at 785 nm was focused to a spot of 70 μm x 130 μm radius at the crystal face. The power of the diode laser was varied from 100%-5% of the total power with a variable attenuator. The absorbed power was measured by subtracting from the input power the power measured after passage of the diode laser through the crystal. Since the Ho $^5I_7$ intensity is proportional to the population, then eq. 7-8 can be fit to the measured intensity vs. pump power curves to find the upconversion rate constant q. However, the population will depend on the spatial distribution of the pump volume inside the crystal. R_p can be written in terms of the total pump rate R and an elliptical pump beam distribution [Fa88]:

$$R_p = \frac{\eta_p P_{abs}}{h\nu_p} \cdot \frac{2\alpha}{\pi w_x w_y [1 - \exp(-\alpha \ell)]} \exp[-\alpha z] \cdot \exp\left[-2\left(\frac{x^2}{w_x^2} + \frac{x^2}{w_x^2}\right)\right] \qquad (7\text{-}9)$$

In this equation P_{abs} represents the total absorbed power, $h\nu_p$ is the energy of the pump photons, η_p is the pump quantum efficiency, α is the absorption coefficient at the pump wavelength, w_x and w_y are the elliptical radii of the pump beam at the crystal face, and ℓ is the thickness of the sample (path length).

Using eq. 7-9 in eq. 7-8 and integrating the population over the pump volume gives a value proportional to the intensity. All that needs to be done is to fit the intensity data to find the upconversion coefficient q. We did this for six samples of various Tm,Ho concentrations (five for YLF and one for YAG). The fits of eq. 7-8 to the data are shown in figures 7-7a-7-7f. The results are summarized in table 7-3. It is clear from this data that for moderate concentrations the upconversion coefficient is about an order of magnitude smaller in YLF than in YAG.

We tried to determine what the concentration dependence of the upconversion rate might be. It was expected that the rate should depend linearly on the product of the Thulium and Holmium concentrations, but no such dependency could be determined from the experimental results. The q values appear to follow a linear dependence with the ratio of the concentrations, but this makes little physical sense.

Table 7-3 Parameters Used in the Data Fit to Upconversion Coefficient q

Sample	τ (ms)	η_a	f_{Ho}	f_{Tm}	q ($cm^3/\mu s$)
Tm(4)Ho(.5)YLF	16.5 ms	1.91	0.2940	0.7060	7.0×10^{-24}
Tm(4)Ho(1.5)YLF	19.0 ms	1.91	0.5554	0.4446	2.3×10^{-24}
Tm(5)Ho(.2)YLF	15.0 ms	1.95	0.1176	0.8824	1.0×10^{-23}
Tm(6)H0(1)YLF	13.0 ms	1.97	0.3570	0.6430	6.5×10^{-24}
Tm(12)Ho(.2)YLF	8.5 ms	2.00	0.5260	0.9473	4.0×10^{-23}
Tm(6)Ho(1)YAG	12.0 ms	1.95	0.4179	0.5821	1.2×10^{-23}

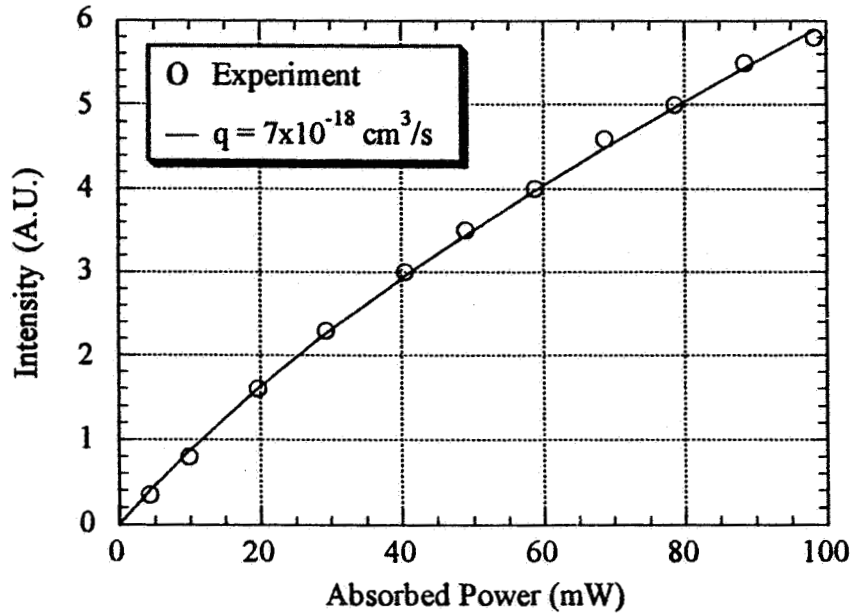

Figure 7-7a Fitting for Upconversion Coefficient in Tm(4)Ho(.5) YLF

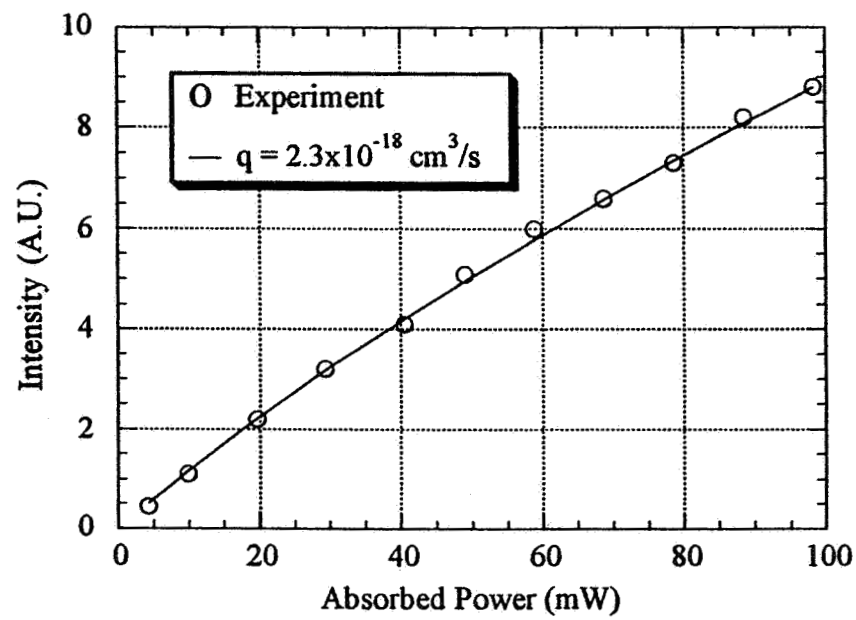

Figure 7-7b Fitting for Upconversion Coefficient in Tm(4)Ho(1.5)YLF

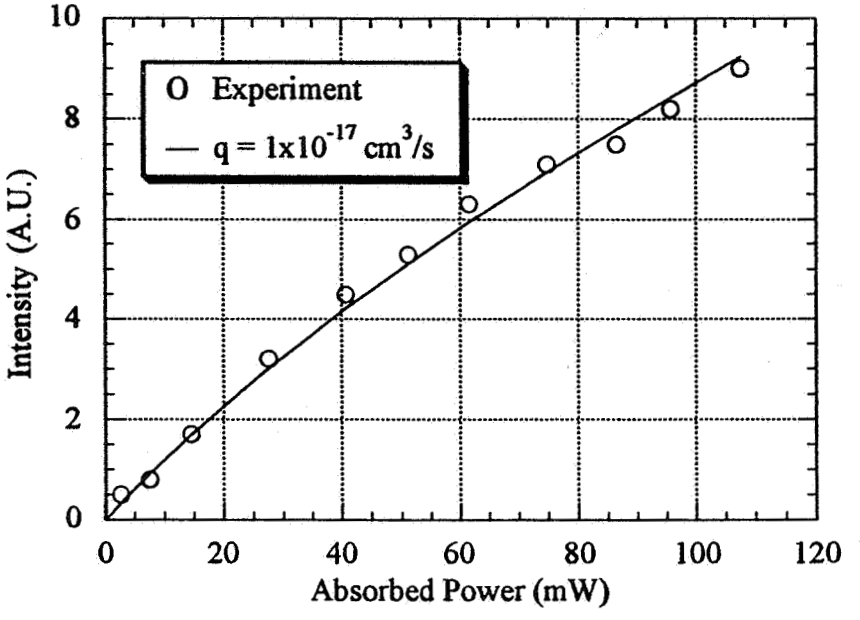

Figure 7-7c Fitting for Upconversion Coefficient in Tm(5)Ho(.2) YLF

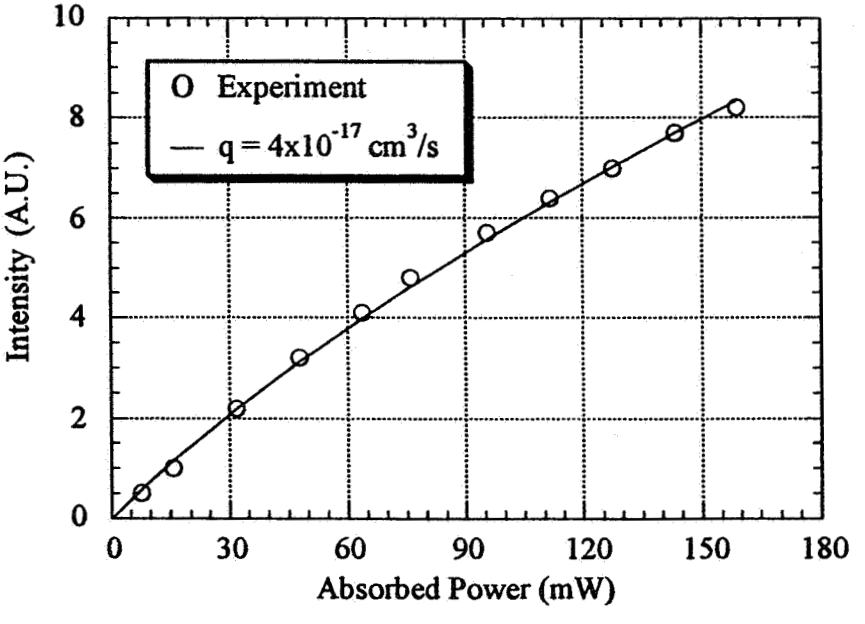

Figure 7-7d Fitting for Upconversion Coefficient in Tm(12)Ho(.2) YLF

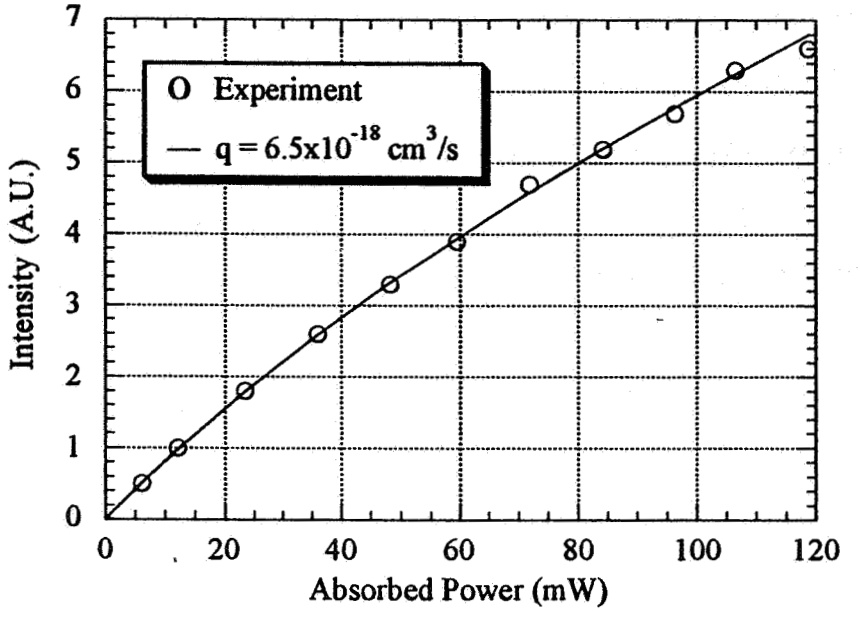

Figure 7-7e Fitting for Upconversion Coefficient in Tm(6)Ho(1) YLF

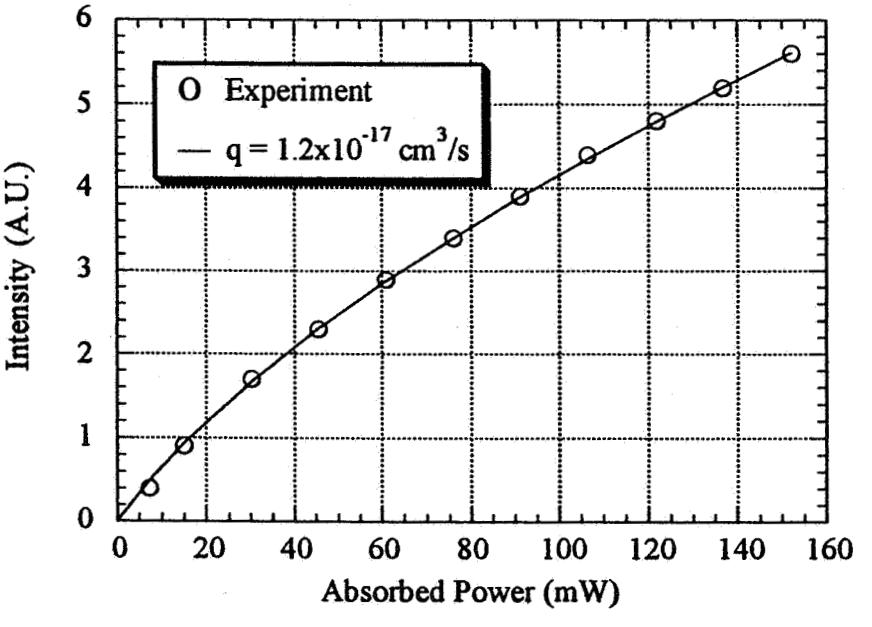

Figure 7-7f Fitting for Upconversion Coefficient in Tm(6)Ho(1) YAG

It should be noted that q is identified with the rate constant p_{27} in the notation used in section 7.2.1, representing the opposite process described by p_{51}. As can be seen from the values tabulated in table 7-3, there is a bit of scatter in the values for the samples studied. If we take an average of the YLF values, neglecting the sample with 12% Tm we find that $q = p_{27} = 6.45 \times 10^{-24}$ $cm^3/\mu s$. This value should be considered, at best, a rough estimate of the rate constant due to the convoluted way in which it was determined. One of the major problems, aside from the assumptions of the rate equation model, is the measurement of the excitation volume. If the measured volume is in error by a factor of 2, the q value could change by an order of magnitude. A better way to determine p_{27} would be to pump the Tm $^3F_4$ manifold directly and look at the decay from the Ho $^5I_5$. Unfortunately, no signal could be detected for this emission under our experimental conditions.

7.2.3 Cross-relaxation $Tm(^3H_4 \rightarrow ^3H_6);Ho(^5I_7 \rightarrow ^5S_2)$ in YLF:Tm,Ho

The decay of the Ho $^5S_2$ exhibits a similar behavior to the Ho $^5I_5$, that is, the decay is exponential for singly doped Holmium, but shortens and becomes non-exponential with the addition of Thulium. Figure 7-8 shows the decay curves for the $^5S_2$ manifold when exciting the $^5S_2$ manifold in co-doped systems with a dye laser. The data for these decays were received courtesy of G. Armagan. The behavior is non exponential with an initial quick component (~ 9μs) followed by a longer one (~ 55μs). This is interpreted as the cross-relaxation process $Ho(^5S_2 \rightarrow ^5I_7);Tm(^3H_6 \rightarrow ^3H_4)$. We can make a similar rate equation analysis as was done for the $^5I_5$ cross-relaxation. In this situation it was found that the rate constant for the cross-relaxation $Ho(^5S_2 \rightarrow ^5I_7);Tm(^3H_6 \rightarrow ^3H_4)$ was $p_{91} = 2.59 \times 10^{-23}$ $cm^3/\mu s$. In the notation here, manifold 9 corresponds to the Ho $^5S_2$ and manifold 1 corresponds to the Tm $^3H_6$.

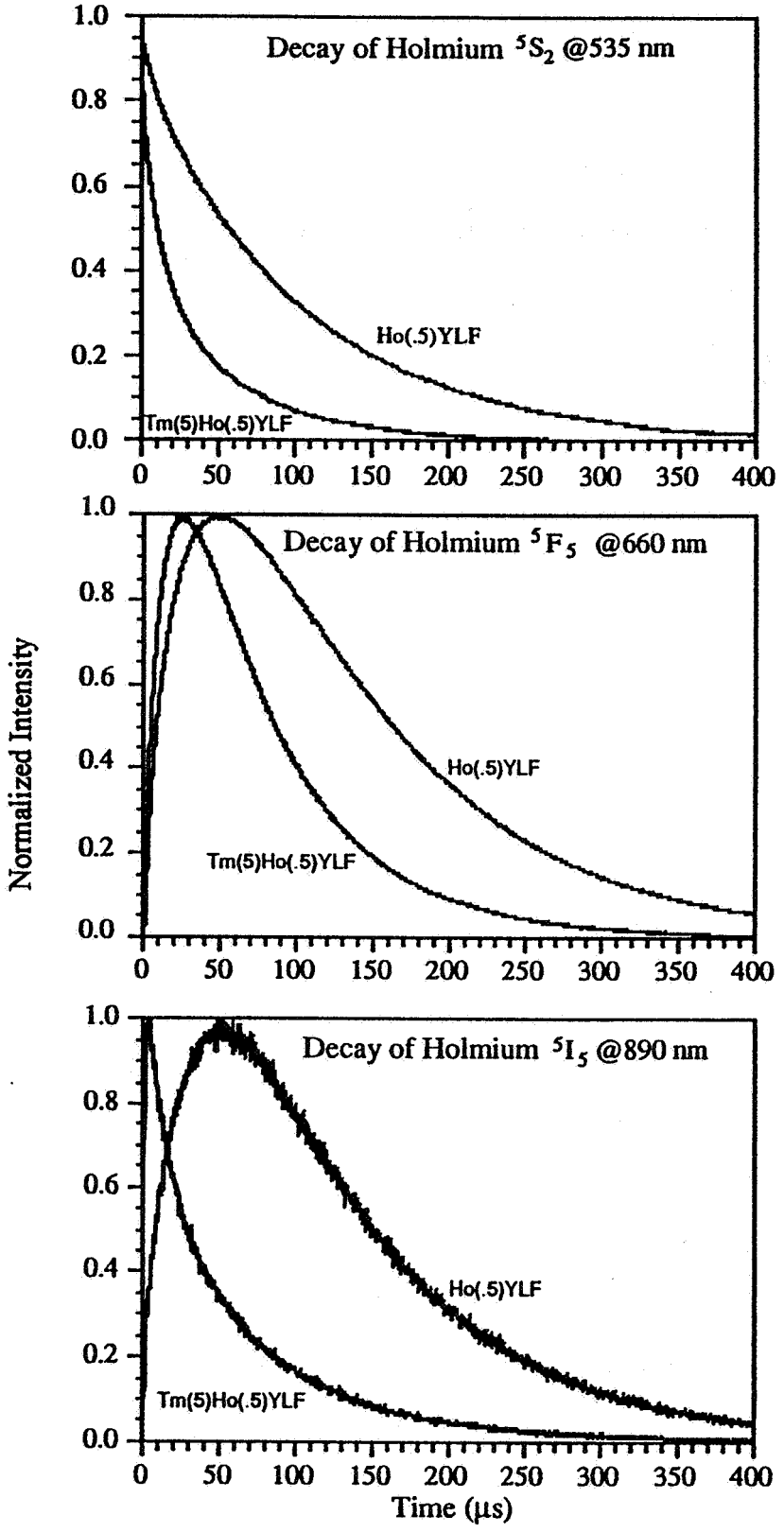

Figure 7-8 Luminescence Decay of $^5S_2$ Manifold After Excitation of $^5S_2$ @535 nm

7.2.4 Energy Transfer $Tm(^3F_4 \rightarrow ^3H_6);Ho(^5I_8 \rightarrow ^5I_7)$ in YLF:Tm,Ho

We now turn to a discussion of the energy transfer between the Tm $^3F_4$ and Ho $^5I_7$ manifolds in co-doped YLF. The transfer of energy from the Tm $^3F_4$ to the Ho $^5I_7$ is of primary interest since it is by this process that the Ho $^5I_7$ manifold becomes populated, and makes possible laser action at 2μm. The transfer has been interpreted by the process $Tm(^3F_4 \rightarrow ^3H_6);Ho(^5I_8 \rightarrow ^5I_7)$ and is pictured in figure 7-9.

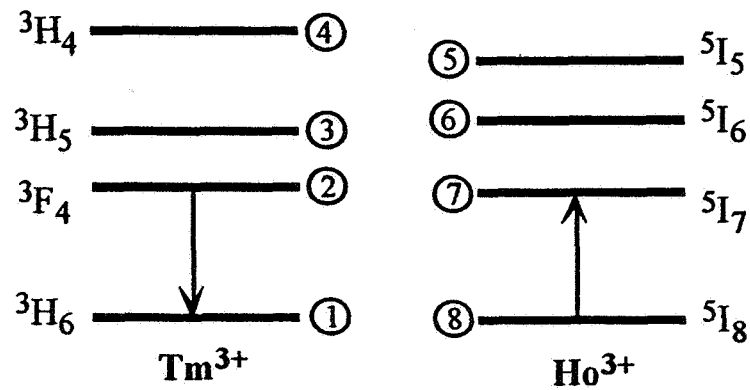

Figure 7-9 Illustration of the Energy Transfer Process $Tm(^3F_4 \rightarrow ^3H_6);Ho(^5I_8 \rightarrow ^5I_7)$

This process is a resonant one since the participating levels exhibit very good overlap (see tables 5-1 and 6-1) and is supported by the decay characteristics of these two manifolds. Figure 7-10a and 7-10b shows the time dependent fluorescence of the Tm $^3F_4$ and Ho $^5I_7$ respectively, for two different excitation wavelengths (a $TiAl_2O_3$ tuned to 785nm and a $CoMgF_2$ tuned to 1.7μm). Figures 7-10 illustrate nicely the correspondence between the decay of the Tm $^3F_4$ and the rise of the Ho $^5I_7$. For the purpose of studying this energy transfer process, direct excitation of the Tm $^3F_4$ greatly simplifies the analysis of the decay curves. For example, in figure 7-10a, when exciting the $^3H_4$, the $^3F_4$ decay has a rise time which reflects the buildup of the population as a result of the cross-relaxation $Tm(^3H_4 \rightarrow ^3F_4);Tm(^3H_6 \rightarrow ^3F_4)$ and the natural decay of the $^3H_4$.

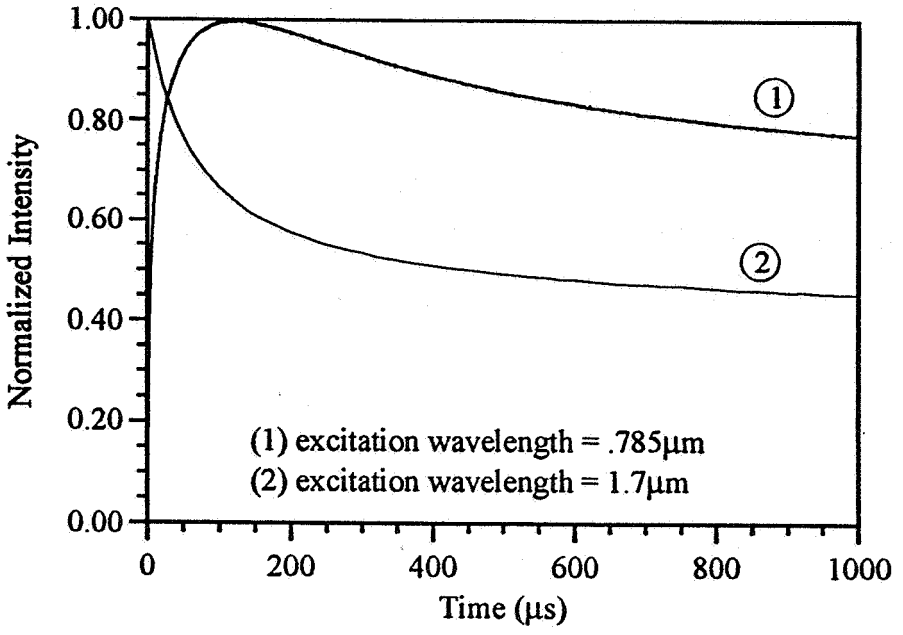

Figure 7-10a Decay of Tm $^3F_4$ in Tm(4)Ho(.5)YLF For Different Excitation Wavelengths

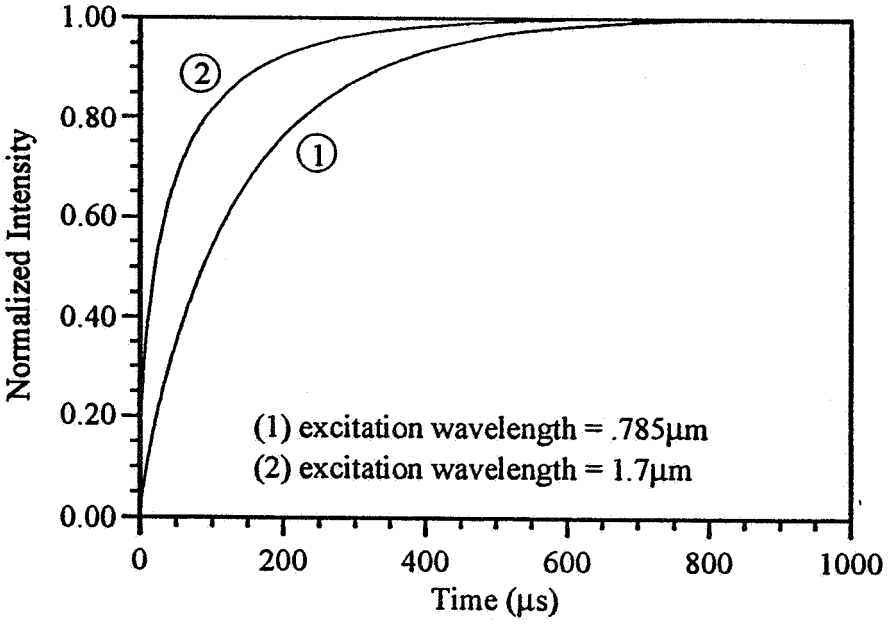

Figure 7-10b Decay of Ho $^5I_7$ in Tm(4)Ho(.5)YLF for Different Excitation Wavelengths

This complicates the analysis because the mixture of many processes combine in the decay profile and it becomes difficult to distinguish between various components. On the other hand, by exciting the Tm $^3F_4$ a much simpler decay profile develops without the complication of the rise time. However, since most of the research on Tm,Ho lasers have utilized Alexandrite or diode pumping of the Tm $^3H_4$ to achieve laser action, the time dependent fluorescence for Tm $^3H_4$ excitation is perhaps more useful. From the spectroscopic point of view, however, we will concentrate mainly on the decay characteristics of the Tm and Ho manifolds for Tm $^3F_4$ excitation.

In figure 7-10b we see an obvious difference in the buildup of the population in the Ho $^5I_7$ when exciting the Tm $^3F_4$ and the Tm $^3H_4$. The rate at which the Ho $^5I_7$ is populated is slower for Tm $^3H_4$ pumping than for Tm $^3F_4$ pumping. The reason for this is that for Tm $^3H_4$ pumping the Tm $^3F_4$ is populated mainly via cross-relaxation and increases gradually with time. During this time energy transfer is also occurring between Tm and Ho, but is dependent on the number of excited Tm ions available for transfer. So, the buildup in the Ho $^5I_7$ is dependent on the efficiency and rate of the cross-relaxation process. On the other hand, directly pumping the Tm $^3F_4$ creates a large population of Tm ions available for transfer. As a result, the Ho $^5I_7$ population rises much faster.

We will now examine the details of the Tm -> Ho energy transfer process Tm($^3F_4$->$^3H_6$);Ho($^5I_8$->$^5I_7$). We have said before that this is a resonant process since the energy levels of the Tm $^3F_4$, $^3H_6$ and Ho $^5I_7$,$^5I_8$ overlap. This is shown pictorially in an energy level diagram in figure 7-11. The overlap is quite good and considering that the line width for transitions at room temperature is about 15-20 cm^{-1} there are a large number of resonant transitions possible between Stark split levels in the lower Tm and Ho manifolds. For an energy mismatch of only 1 cm^{-1} there are three transitions possible:

1.) Tm(5599 ->305);Ho(0 ->5293)

2.)Tm(5599 ->372);Ho(7 ->5233)

3.) Tm(5599 ->419);Ho(48 ->5229)

In general, the process can be written as Tm(i ->j);Ho(ℓ ->k) where i, j, ℓ, k denotes a Stark level of the $^3F_4$,$^3H_6$,$^5I_8$, and $^5I_7$ manifold respectively. The probability of finding a Tm $^3F_4$ ion in Stark level i is given by the Boltzmann distribution P_i

$$p_i = \frac{\exp(-\Delta E_i / kT)}{\sum_i \exp(-\Delta E_i / kT)} \qquad (7\text{-}10a)$$

and the probability of finding a Ho $^5I_8$ ion in Stark level ℓ is given by:

$$p_\ell = \frac{\exp(-\Delta E_\ell / kT)}{\sum_\ell \exp(-\Delta E_\ell / kT)} \qquad (7\text{-}10b)$$

Note that ΔE_i or ΔE_ℓ are energy differences from the lowest Stark level to the Stark level i or ℓ in the $^3F_4$ or $^5I_8$ manifold. So, the energy transfer rate for a given transition Tm(i ->j);Ho(ℓ ->k) will depend on the product of the probability of an ion being in Stark level i of the Tm $^3F_4$ and an ion being in Stark level ℓ of the Ho $^5I_8$ and a temperature independent transfer rate constant, which will contain matrix elements between the initial and final states. This can be written as:

$$k_{i\ell} = w_{i\ell} p_i p_\ell \qquad (7\text{-}11a)$$

Actually, there are many possible transfers both resonant and non resonant, so eqs. 7-10 must be summed over all transitions that are deemed physically realizable. The rate of backtransfer will have a similar form:

$$k_{kj} = w_{kj} p_k p_j \qquad (7\text{-}11b)$$

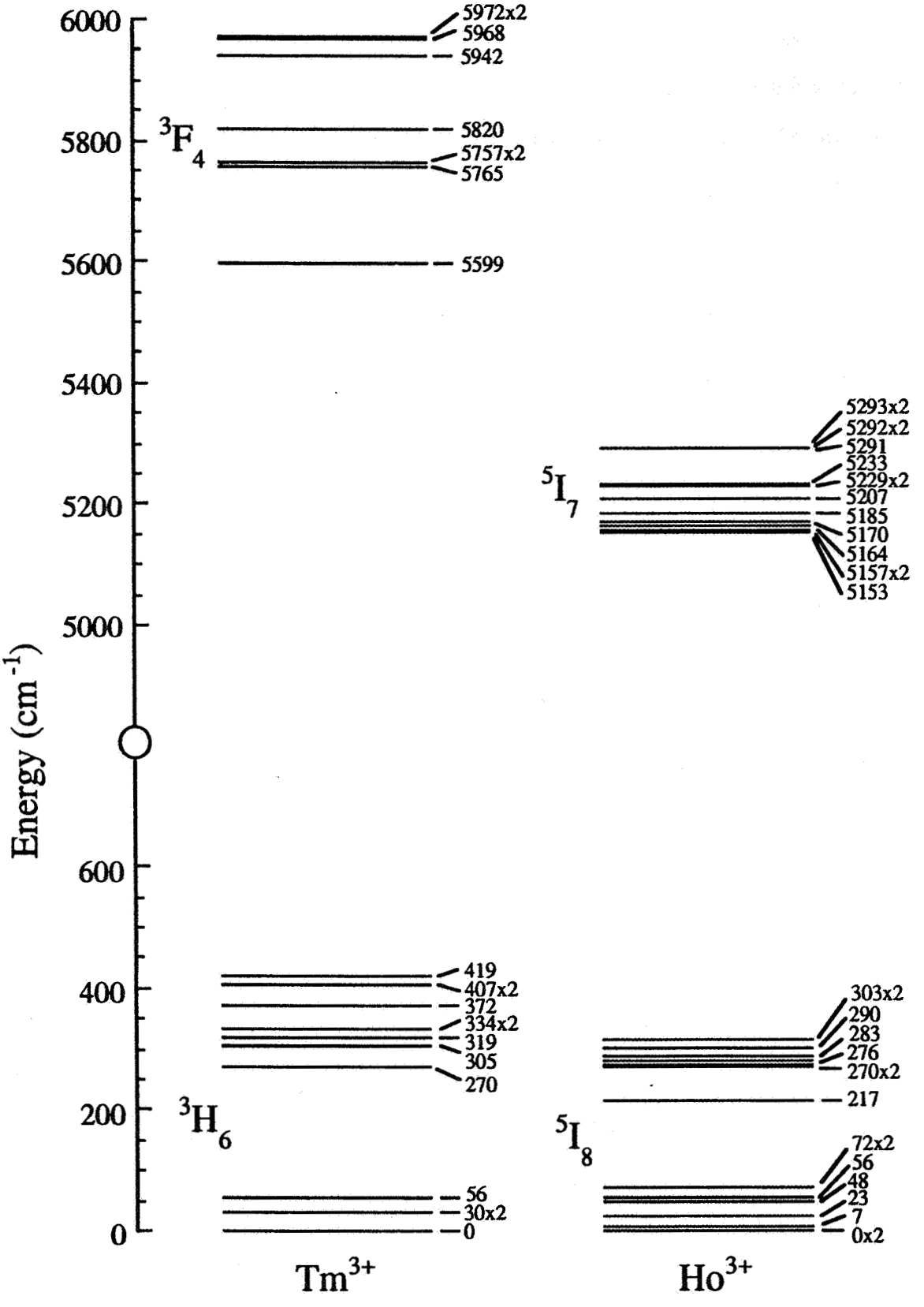

Figure 7-11 Stark Levels of the Ground and Lower Manifolds in YLF:Tm,Ho

It is obvious that such an approach to calculating energy transfer rates is intractable given the number of possible transitions, assuming one can even identify all of them. Nevertheless, the exercise is useful in understanding how energy is transferred. It also shows us that describing the population of the combined Tm $^3F_4$ and Ho $^5I_7$ populations by a thermal distribution is justified. That this is true follows from the large number of possible transitions and the fact that the transfer times are much faster than the lifetimes of the manifolds. At any rate, we can write down the system of equations of the rate of change of the Tm $^3F_4$ and Ho $^5I_7$ populations.

The rate equations are:

$$\frac{dn_2}{dt} = -\frac{n_2}{\tau_2} - p_{28}n_2n_8 + p_{71}n_7n_1 \qquad (7\text{-}12a)$$

$$\frac{dn_7}{dt} = -\frac{n_7}{\tau_7} + p_{28}n_2n_8 - p_{71}n_7n_1 \qquad (7\text{-}12b)$$

In these equations the subscript numbers refer to a particular manifold as denoted in figure 7-9. τ_2 and τ_7 are the natural (radiative + nonradiative) lifetimes of the Tm $^3F_4$ and Ho $^5I_7$ manifolds the absence of energy transfer. p_{28} and p_{71} are the rate constants of Tm -> Ho transfer and Ho -> Tm backtransfer respectively.

Now, if we assume that these are the only manifolds with any sufficient population, which is probably the case for direct excitation of the Tm $^3F_4$, then we can write $n_1 + n_2 = C_{Tm}N$ and $n_7 + n_8 = C_{Ho}N$, where C_{Tm} and C_{Ho} are the dopant concentrations of Tm and Ho. N is the number of Y^{3+} sites in YLF into which the dopant ion are substituted. This allows us to eliminate the ground state populations from the rate equations and write them as:

$$\frac{dn_2}{dt} = -\frac{n_2}{\tau_2} - \alpha n_2 + \beta n_7 + (p_{28} - p_{71})n_2n_7 \qquad (7\text{-}13a)$$

$$\frac{dn_7}{dt} = -\frac{n_7}{\tau_7} + \alpha n_2 - \beta n_7 - (p_{28} - p_{71}) n_2 n_7 \qquad (7\text{-}13b)$$

where we have written $\alpha = p_{28} C_{Ho} N$ and $\beta = p_{71} C_{Tm} N$. α and β are the rates of energy transfer and back transfer analogous to eq. 7-11a and 7-11b. This is the reason why we referred to p_{28} and p_{71} as rate constants because they are independent of concentration. The set of coupled equations can be solved numerically for supplied values of τ_2, τ_7, α and β. We have written a computer program which solves these differential equations numerically that uses a Runge Kutta method. The solutions are sufficiently smooth that it was not necessary to incorporate a variable step size for differentiation at various points. It was discovered that the solutions did not vary much if the nonlinear term involving $n_2 n_7$ was dropped, as long as the initial condition of the ions excited into the upper manifold at t=0 were relatively small. This condition corresponds to low pump densities of the excitation source. For the $CoMgF_2$ laser we used only had 6mj of energy in a beam size that was 100's of microns in diameter. This allows us to linearize equations 7-13 and solve them to obtain closed form solutions for the rate of change of the populations n_2 and n_7. The solutions were found to be (the derivation is given in Appendix D):

$$\frac{n_2(t)}{n_2(0)} = \left(\frac{\beta}{\alpha+\beta}\right)\exp(-t/\tau) + \left(\frac{\alpha}{\alpha+\beta}\right)\exp[-(\alpha+\beta)t] \qquad (7\text{-}14a)$$

$$\frac{n_7(t)}{n_2(0)} = \left(\frac{\alpha}{\alpha+\beta}\right)\exp(-t/\tau) - \left(\frac{\alpha}{\alpha+\beta}\right)\exp[-(\alpha+\beta)t] \qquad (7\text{-}14b)$$

The coupled lifetime τ in equations 7-14 represents the lifetime of the Tm and Ho manifolds since after a short amount of time the energy levels in Tm and Ho reach a thermal equilibrium and decay at the same rate. This is indeed what is found from the experiments. After several hundreds of microseconds, the decay of Tm and Ho proceed at the same rate.

This is due to the nature of the Tm <-> Ho sharing process. The upper manifolds have a certain amount of energy as a combined system and an agreement through Boltzmann statistics to maintain the distribution between the two. Even though the total amount of energy in the upper states is decreasing, the distribution between Tm and Ho is maintained, so they decay at the same rate. By looking at the very early parts of the decay curves, however, we can catch Tm and Ho in the act of sharing their energy. This is exactly the energy transfer process we are interested in.

Decay Measurements using the $CoMgF_2$ laser tuned to 1.75μm the were made on several co-doped YLF samples containing various concentrations of Tm and Ho. The emission was monitored at 1.7μm and 2.06μm and the decay curves obtained. The intensity was normalized to one and the decay curves for the Tm $^3F_4$ were fit to equation 7-14a to obtain the energy transfer rates α and β. The values of α, β and τ obtained by fitting the decay curves to Eq. 7-14a are shown in table 7-4. Figures 7-12a – 7-12h display the first 1000 μs of the measured decay curves of eight YLF samples co-doped with different amounts of Tm and Ho. The best fit to the data is also displayed in these figures by the dashed lines.

Now that we have the rates α and β , we can extract the rate constants and see how well they agree with each other because, as we said earlier, they should be independent of concentration. Recall that we defined $\alpha = p_{28}C_{Ho}N$ and $\beta = p_{71}C_{Tm}N$. We know the dopant concentrations and the density of sites in the samples. For YLF and YAG $N=1.38\times10^{-22}$ ions/cm^3 and for LuAG $N=1.42\times10^{-22}$. It is therefor a simple matter to extract the rate constants p_{28} and p_{71} . The results are presented in table 7-5. It is seen from these calculated rate constants that they do not vary too much for the different samples. Overall, the agreement is not too bad considering that the fits to the data were marginally okay.

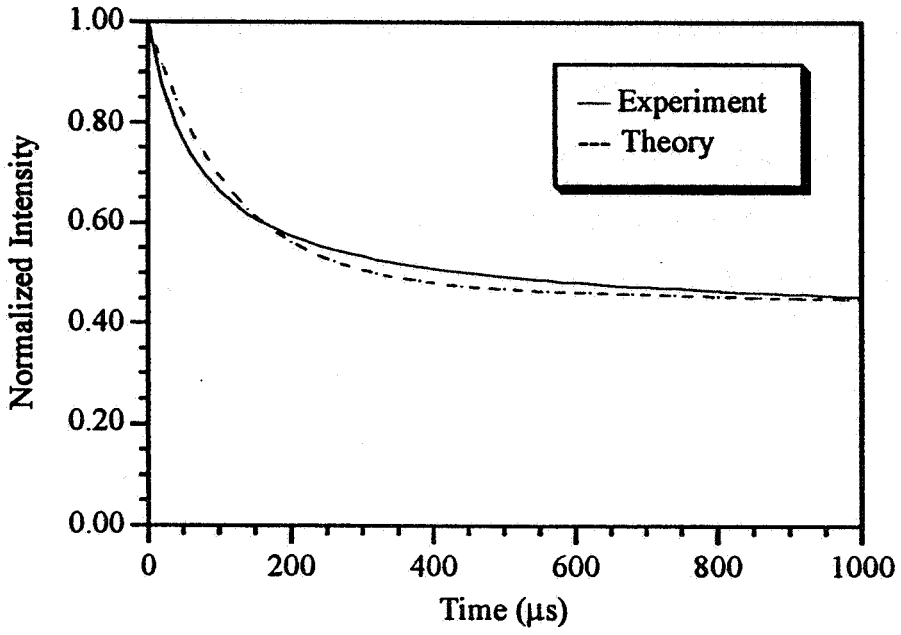

Figure 7-12a Decay Curve of Tm(4)Ho(.5)YLF

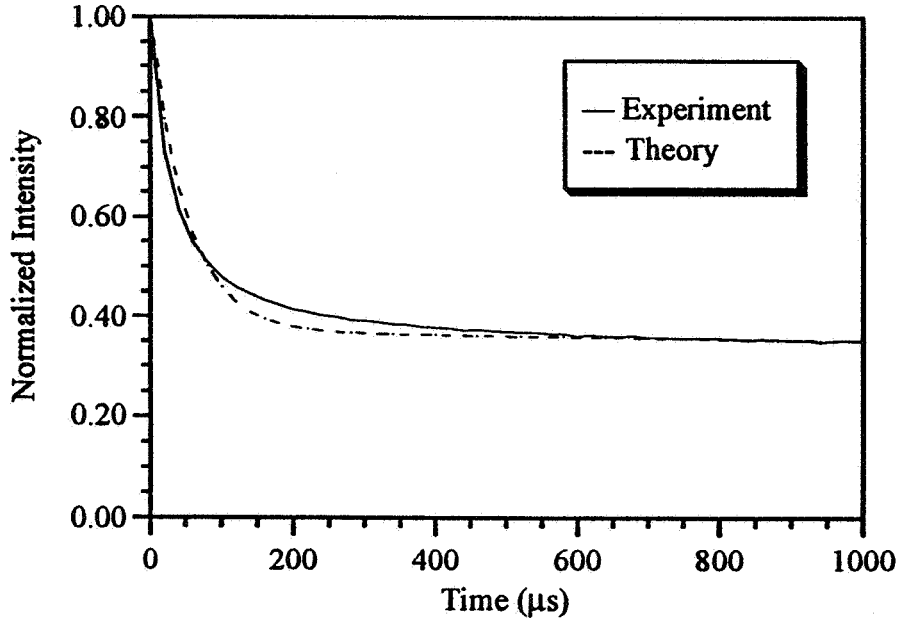

Figure 7-12b Decay of Tm(4)Ho(1.5)YLF

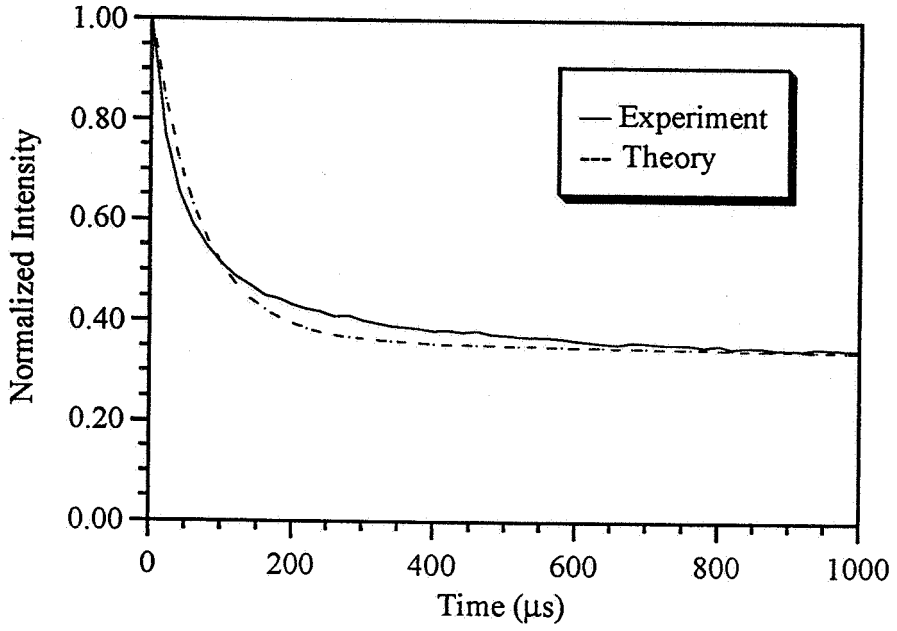

Figure 7-12c Decay of Tm(4)Ho(1)YLF

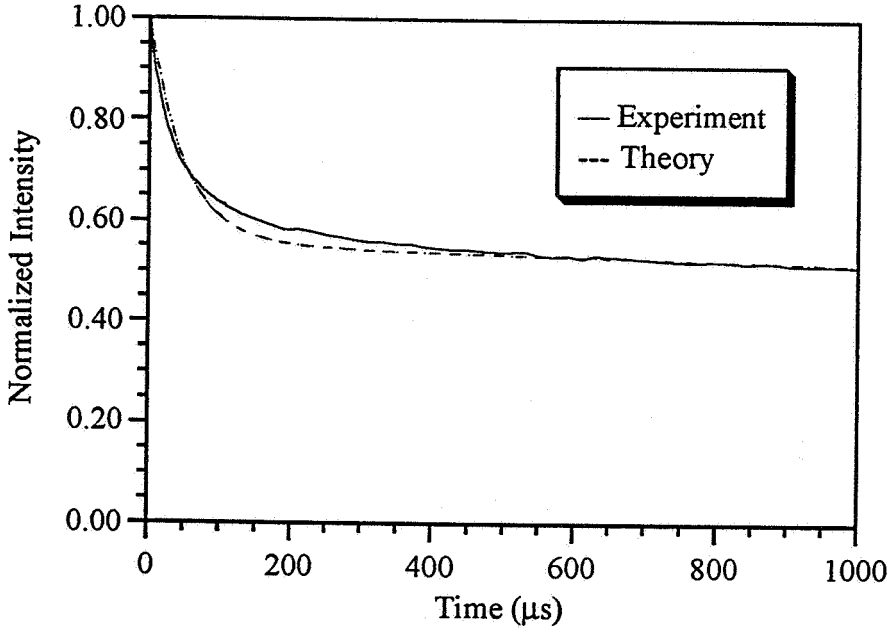

Figure 7-12d Decay of Tm(6)Ho(1)YLF

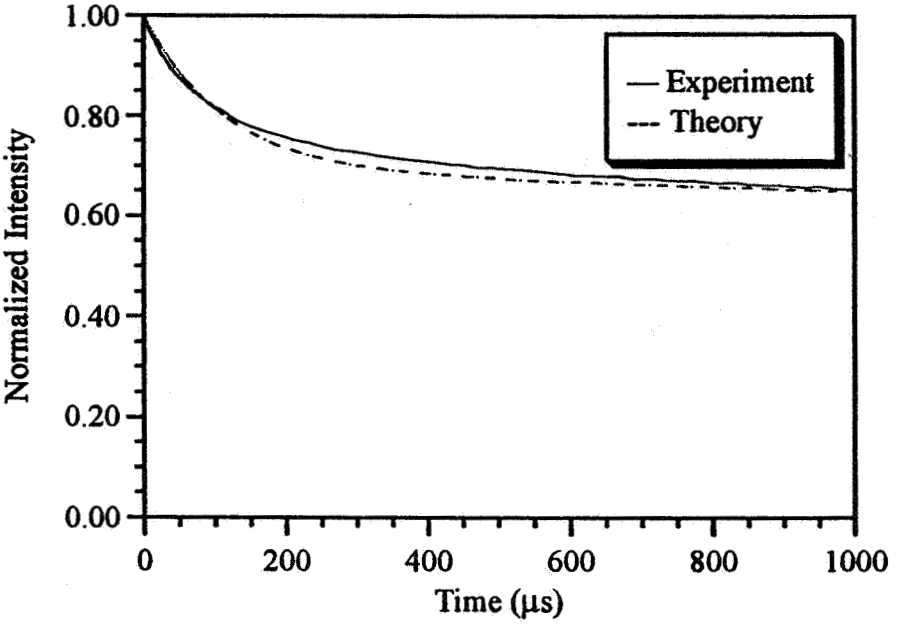

Figure 7-12e Decay of Tm(5)Ho(.2)YLF

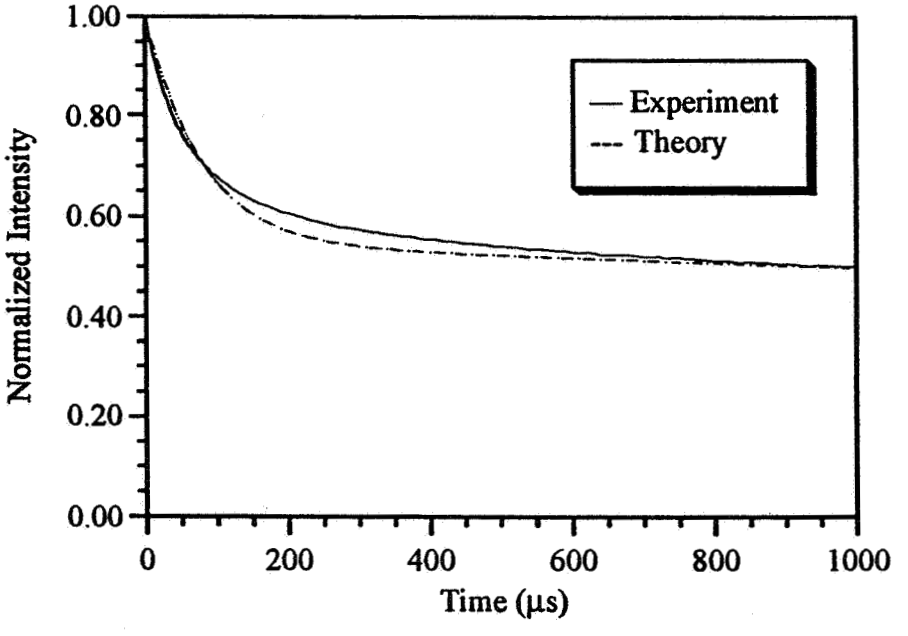

Figure 7-12f Decay of Tm(5)Ho(.5)YLF

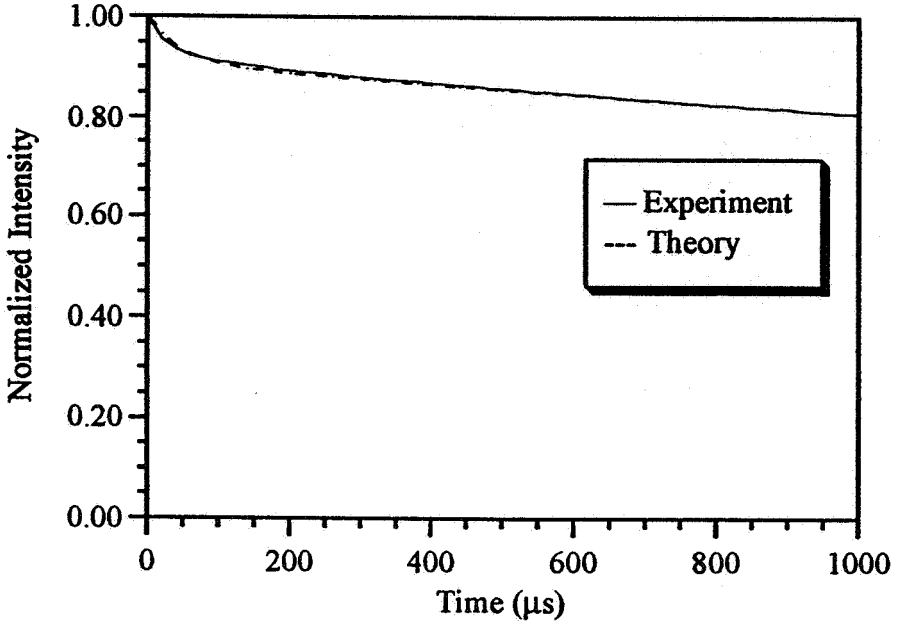

Figure 7-12g Decay of Tm(12)Ho(.2)YLF

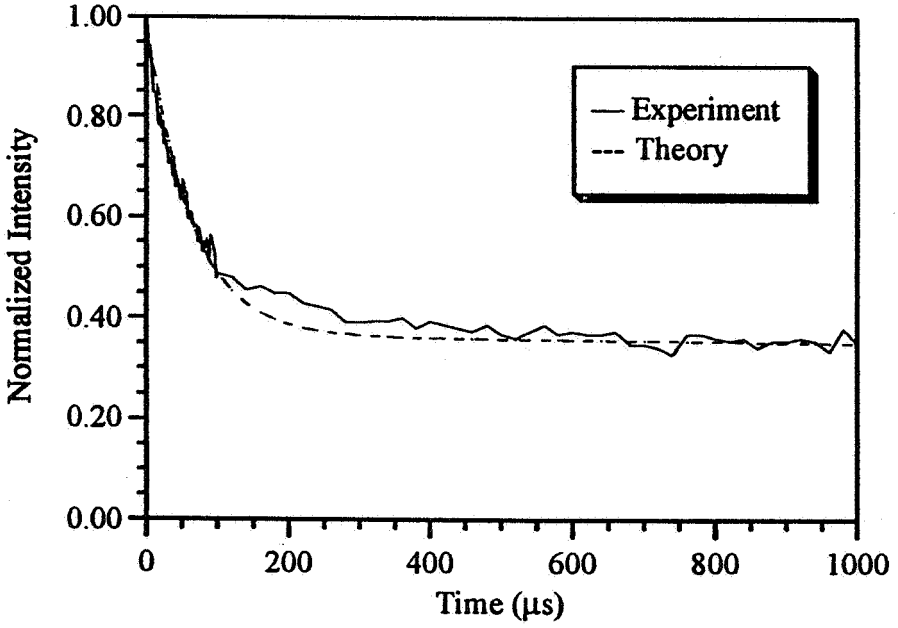

Figure 7-12h Decay of Tm(1)Ho(12)YLF

Table 7-4 Values of the Fitting Parameters to eq. 7-14a

Sample	α (μs^{-1})	β (μs^{-1})	τ (μs)
Tm(4)Ho(0.5)YLF	0.004125	0.004532	15858
Tm(4)Ho(1.0)YLF	0.009176	0.005243	16237
Tm(4)Ho(1.5)YLF	0.012221	0.007178	18674
Tm(5)Ho(0.2)YLF	0.002750	0.006295	14502
Tm(5)Ho(0.5)YLF	0.005863	0.007103	10491
Tm(6)Ho(1.0)YLF	0.009152	0.011415	13103
Tm(1)Ho(12)YLF	0.005922	0.010284	25108
Tm(12)Ho(0.2)YLF	0.020101	0.002016	8519
Tm(6)Ho(1.0)YAG	0.005124	0.011145	11758
Tm(5)Ho(.5)LuAG	0.002901	0.005944	9892

Table 7-5 Values of the Rate Constants for Energy Transfer $Tm(^3F_4 \rightarrow ^3H_6);Ho(^5I_8 \rightarrow ^5I_7)$

Sample	p_{28} ($cm^3/\mu s$)	p_{71} ($cm^3/\mu s$)	p_{71} / p_{28}
Tm(4)Ho(0.5)YLF	0.5978×10^{-22}	0.0821×10^{-22}	0.1373
Tm(4)Ho(1.0)YLF	0.6649×10^{-22}	0.0949×10^{-22}	0.1427
Tm(4)Ho(1.5)YLF	0.5898×10^{-22}	0.1300×10^{-22}	0.2204
Tm(5)Ho(0.2)YLF	0.9963×10^{-22}	0.0912×10^{-22}	0.0915
Tm(5)Ho(0.5)YLF	0.8497×10^{-22}	0.1209×10^{-22}	0.1422
Tm(6)Ho(1.0)YLF	0.6631×10^{-22}	0.1378×10^{-22}	0.2078
Tm(1)Ho(12)YLF	0.4913×10^{-22}	0.0621×10^{-22}	0.1263
Tm(12)Ho(0.2)YLF	0.7304×10^{-22}	0.1268×10^{-22}	0.1736
Tm(6)Ho(1.0)YAG	0.3713×10^{-22}	0.1346×10^{-22}	0.3625
Tm(5)Ho(.5)LuAG	0.4083×10^{-22}	0.0836×10^{-22}	0.2047

The Tm->Ho transfer and Ho->Tm transfer interaction parameters can be found by calculating the appropriate spectral overlap integral in the Förster-Dexter theory of resonant energy transfer. Using eq. 6-1 we found that:

Tm->Ho transfer $Tm(^3F_4 \rightarrow ^3H_6);Ho(^5I_8 \rightarrow ^5I_7)$: $C_{DA} = 1.6901 \times 10^{-45}$ $cm^6/\mu s$

Ho->Tm transfer $Ho(^5I_7 \rightarrow ^5I_8);Tm(^3H_6 \rightarrow ^3F_4)$: $C_{DA} = 1.2424 \times 10^{-46}$ $cm^6/\mu s$

Tm->Tm migration $Tm(^3F_4 \rightarrow ^3H_6);Tm(^3H_6 \rightarrow ^3F_4)$: $C_{DD} = 2.6191 \times 10^{-45}$ $cm^6/\mu s$

Ho->Ho migration $Ho(^5I_7 \rightarrow ^5I_8);Ho(^5I_8 \rightarrow ^5I_7)$: $C_{DD} = 7.2107 \times 10^{-45}$ $cm^6/\mu s$

The connection between the microscopic interaction parameters and the rate constants has not been put into a theoretical framework at this time, however, we would expect that the ratio of the microscopic interaction parameters should be the same as the ratio of the rate constants for Tm->Ho transfer and Ho->Tm transfer. The ratio of the interaction parameters in this case is $C_{DA}(\text{Ho->Tm})/C_{DA}(\text{Tm->Ho}) = 0.0735$. This is a factor of two smaller than the average value of the ratio of the rate constants in table 7-5, where it is found that $p_{71}/p_{28} = 0.1552$.

The reason for the difference in these two ratios possibly resides in the fact that the ratio calculated with the interaction parameters accounts only for the resonant energy transfer via the spectral overlap, whereas the ratio of the rate constants accounts for all transfers both resonant and non-resonant. To see if this reasoning is correct, we have derived a relation in terms of known quantities for the ratio of the rate constants assuming only the resonant transitions participate in the process. The derivation is given in Appendix E. The result is:

$$\frac{p_{71}}{p_{28}} = \frac{Z_2 Z_8}{Z_1 Z_7} \exp\left[-\left(E_{ZL}^{3F4} - E_{ZL}^{5I7}\right)/k_B T\right] \qquad (7\text{-}16)$$

where Z_1 is the partition function of the Tm $^3H_6$, Z_2 is the partition function of the Tm $^3F_4$, Z_7 is the partition function of the Ho $^5I_7$, and Z_8 is the partition function of the Ho $^5I_8$. E_{ZL}^{3F4} and E_{ZL}^{5I7} are the energies of the lowest Stark levels in the Tm $^3F_4$ and Ho $^5I_7$ manifolds, respectively. The values for all of these terms can be found in table 5-3 and table 6-3. The ratio of the rate constants for T=300°K was calculated from eq. 7-16 and found to be $p_{71}/p_{28} = 0.0616$. This is very close to the ratio of the interaction parameters, giving credence to our earlier statement.

We can use the ratio of Tm->Ho transfer and Ho-> Tm backtransfer to experimentally determine the fraction of ions residing in the excited Ho ions after equilibrium between the Tm and Ho ions is reached. That is:

$$f_{Ho} = \frac{n_7}{n_7 + n_2} \tag{7-17}$$

which can be rewritten as:

$$f_{Ho} = \frac{1}{1 + (n_2 / n_7)} \tag{7-18}$$

In steady state, we can set $dn_2/dt = dn_7/dt = 0$. That is we can set equations 7-12 equal to zero. If we set eq. 7-12a equal to zero and neglect the term n_2/τ_2 as being small compared to the others, then we obtain:

$$\frac{p_{71}}{p_{28}} = \frac{n_7 n_1}{n_2 n_8} \tag{7-19}$$

Using $n_1 = n_2 - C_{Tm}N$ and $n_8 = n_7 - C_{Ho}N$, the expressions for conservation of Tm and Ho ions, and neglecting the non-linear terms involving $n_2 n_7$ we find that:

$$\frac{n_2}{n_7} = \frac{C_{Tm}}{C_{Ho}} \frac{p_{71}}{p_{28}} \tag{7-20}$$

This can be used in eq. 7-18 to find the fraction of Ho ions in the $^5I_7$ state. The results are tabulated in table 7-6

Table 7-6 Fraction of Ho Ions in the $^5I_7$ state For a Given Concentration

Sample	n_2/n_7	f_{Ho}	$f_{Tm} = (1-f_{Ho})$
Tm(4)Ho(0.5)YLF	1.2416	0.4461	0.5539
Tm(4)Ho(1.0)YLF	0.6208	0.6169	0.3831
Tm(4)Ho(1.5)YLF	0.4138	0.7072	0.2928
Tm(5)Ho(0.2)YLF	3.8800	0.2049	0.7951
Tm(5)Ho(0.5)YLF	1.5520	0.3918	0.6082
Tm(6)Ho(1.0)YLF	0.9312	0.5178	0.4822
Tm(1)Ho(12)YLF	0.0129	0.0969	0.9031
Tm(12)Ho(0.2)YLF	9.3120	0.9872	0.0128

Of course, this is not the only interpretation of the data that can be put forth. In fact, given that the rate equation method did not fit the data better would suggest that the decay is not composed of two exponentials, but perhaps three or more. We did a curve fit using Kaleidagraph™ data analysis/graphics application to fit the data to three exponentials. Kaleidagraph™ uses the Levenberg-Marquart algorithm to fit the data.

Six parameters were used that composed an equation for the sum of exponentials of the form:

$$\frac{n(t)}{n(0)} = A_1 \exp(-t/\tau_1) + A_2 \exp(-t/\tau_2) + A_3 \exp(-t/\tau_3) \tag{7-21}$$

The best set of parameters A_1, τ_1, A_2, τ_2,A_3, τ_3 were obtained from the curve fits of the experimental data performed by Kaleidagraph™. The data fits were excellent for three exponentials. The parameters appear in tables 7-7 and 7-8.

From the data in tables 7-7 and 7-8 we can see first of all that the long time decay of Tm and Ho are the same. This is as expected because of the thermalization between Tm and Ho discussed earlier. The early time behavior is quite different however. In both cases the early time behavior (0 – 1000 μs) appears to be composed of two exponentials with time constants in the tens to hundreds of microseconds. The rise time of the Ho $^5I_7$, however, seems to be faster than the initial decay time of the Tm $^3H_4$. This would be contrary to common sense because if Tm is feeding Ho initially before thermal equilibrium, then the decay in Tm would be expected to match the rise in Ho. It must be remembered that the signal detected that forms the decay curve is the fluorescence, which is due to radiative emission from the ions. Given a sufficient amount of time, an ion in Ho or Tm will emit radiatively unless it finds somewhere to transfer its energy or can give phonons to the lattice and de-excite that way.

At t=0 Tm has many excitations and Ho has none. Immediately Tm starts transferring to Ho because all Ho sites welcome the energy. Not many of the Tm ions can emit radiatively because Ho is stealing the excitation energy from Tm. Many Ho ions begin to exist in excited states, but still less than Tm. The Ho ions distribute themselves among the Stark levels, but in levels which are less resonant with Tm. Remember that at the beginning of this section we saw that the most resonant transitions come from the bottom of the $^3F_4$ (5599 cm^{-1}) and they end up at the top of the $^5I_7$ (5293 cm^{-1}, 5233 cm^{-1}, and 5229 cm^{-1}). When the excitation distributes itself in the lower Stark levels of the Ho $^5I_7$ then backtransfer is less resonant. The reader can convince oneself by examining figure 7-11. So, while the backtransfer exists, it should be slower than the transfer. Thus, initially Ho keeps its excitation longer and increases its chances of decaying radiatively.

Table 7-7 Exponential Components of Tm $^3F_4$ Decay for Tm $^3F_4$ Excitation

	$n(t)/n(0) = A_1\exp(-t/\tau_1) + A_2\exp(-t/\tau_2) + A_3\exp(-t/\tau_3)$					
Sample	A_1	τ_1 (μs)	A_2	τ_2 (μs)	A_3	τ_3 (μs)
Tm(4)Ho(0.5)YLF	0.3411	57.5	0.1802	319.8	0.4721	15998
Tm(4)Ho(1.0)YLF	0.4656	37.6	0.1667	265.2	0.3591	16474
Tm(4)Ho(1.5)YLF	0.4451	26.8	0.1841	165.3	0.3677	18412
Tm(5)Ho(0.2)YLF	0.1887	66.2	0.1138	366.5	0.6911	14596
Tm(5)Ho(0.5)YLF	0.3166	47.7	0.1359	312.5	0.5402	10633
Tm(6)Ho(1.0)YLF	0.2688	23.1	0.1735	146.2	0.5509	13197
Tm(1)Ho(12)YLF	0.3960	38.8	0.2116	195.2	0.3625	25310
Tm(12)Ho(0.2)YLF	0.0835	50.9	—	—	0.9068	8536
Tm(6)Ho(1.0)YAG	0.2256	39.4	0.0770	354.0	0.6762	11907
Tm(5)Ho(.5)LuAG	0.1647	48.9	0.1622	282.5	0.6650	9926

Table 7-8 Exponential Components of Ho $^5I_7$ Decay for Tm $^3F_4$ Excitation

	$n(t)/n(0) = -A_1\exp(-t/\tau_1) - A_2\exp(-t/\tau_2) + A_3\exp(-t/\tau_3)$					
Sample	A_1	τ_1 (μs)	A_2	τ_2 (μs)	A_3	τ_3 (μs)
Tm(4)Ho(0.5)YLF	0.4754	21.1	0.4306	183.5	1.0669	17125
Tm(4)Ho(1.0)YLF	0.4325	5.65	0.5004	61.5	1.0396	16361
Tm(4)Ho(1.5)YLF	0.5291	4.76	0.4585	39.3	1.0264	19707
Tm(5)Ho(0.2)YLF	0.4333	22.5	0.3723	213.8	1.0814	15116
Tm(5)Ho(0.5)YLF	0.4415	9.07	0.5531	79.4	1.0645	10640
Tm(6)Ho(1.0)YLF	0.6109	5.36	0.3723	44.5	1.0292	13212
Tm(1)Ho(12)YLF	1.0613	2.52	—	—	1.0009	25123
Tm(12)Ho(0.2)YLF	0.7491	4.32	0.2893	30.3	1.0238	8597
Tm(6)Ho(1.0)YAG	0.7201	4.97	0.2897	57.9	1.0325	11535
Tm(5)Ho(0.5)LuAG	0.4049	22.8	0.3205	183.5	1.0766	10222

The result of all this is that the rise in Ho should be faster than the decay of Tm. As time goes on things begin to equal out and thermal equilibrium is reached between the Tm and Ho ions. However, since the backtransfer from Ho to Tm is less effective than the transfer of Tm to Ho, the thermalized lifetime of the combined Tm,Ho system decays at the lifetime that the Ho ions are decaying at. This will not always be the case because of radiative trapping or impurities that quench the lifetime.

Finally, we suggest another theory which does not necessarily negate the rate equation model but suggests a way to modify it. The fact that there are two exponentials in the early part of the decay suggests that there may be two distinct regions of decay. In one region a Tm ion sees and enhanced region of Ho ions and another region where Tm sees a depleted region of Ho ions. The rate equation model as was proposed here does not account for changes in the donor and acceptor environments. This offers an explanation for the excellent fit of the decay by three exponentials, but does not suggest a feasible way to fix the rate equation model. A fusion between these two models and a better characterization of the energy transfer process on the lines of that discussed at the beginning of this section would perhaps be a good starting point for further investigation.

References to Chapter 7

[Bu92] P.A. Budini, M.G. Knight, E.P. Chicklis, H.P. Jenssen, "Performance of a Diode-Pumped High PRF Tm,Ho:YLF Laser," IEEE J. Quan. Elec. **28**,1029 (1992)

[Ca75] D. Castlebury "Energy Transfer in Sensitized Rare Earth Lasers," PhD thesis M.I.T (1975)

[Es90] L. Esterowitz, "Diode-pumped holmium, thulium, and erbium lasers between 2 and 3 μm operating cw at room temperature," Opt. Eng. **29**, 676 (1990)

[Fa87] T.Y. Fan, G. Huber, R.L. Byer, P. Mitzscherlich, "Continuous-wave operation at 2.1 μm of a diode-laser-pumped, Tm-sensitized Ho:$Y_3Al_5O_{12}$laser at 300K," Opt. Lett. **12**, 678 (1987)

[Fa88] T.Y. Fan, G.Huber, R.L. Byer, "Spectroscopy and Diode Laser-Pumped Operation of Tm, Ho:YAG," IEEE J. Quan. Elec. **24**, 924 (1988)

[He89] H. Hemmati, "2.07-μm cw diode-laser pumped Tm,Ho:$YLiF_4$ room-temperature laser," Opt. Lett. **14**, 435 (1989)

[Ki87] G.Kintz, I.D. Abella and L. Esterowitz, Proc. International Conference on lasers, LASERS '87, 398-403 (1987)

[Km94] J.D Kmetec,T.S. Kubo, T.J. Kane, C.J. Grund, "Laser performance of diode-pumped thulium-doped $Y_3Al_5O_{12}$, $(Y,Lu)_3Al_5O_{12}$, and $Lu_3Al_5O_{12}$ crystals," Opt. Lett. **19**, 186 (1994)

[St93] M.E. Storm, "Holmium YLF Amplifier Performance and the Prospects for Multi-Joule Energies Using Diode-Laser Pumping," IEEE J. Quan. Elec. **29**, 440 (1993)

[Sv82] O. Svelto "Principles of Lasers," 2nd ed. Plenum Press (1982)

[Ty89] J.K. Tyminski,D.M. Franish and M. Kokta, "Gain Dynamics of T:Ho:YAG pumped in near infrared," J. Appl. Phys. **65**, 3181-3188 (1988)

CHAPTER 8
Summary and Conclusions

The results of the preceding investigation lead to a very interesting conclusion, which is here to be deduced.

Albert Einstein
Does the Inertia of a body depend upon its energy content?
Annalen der Physik, 17, 1905

8.1 Summary of the Results

A detailed analysis of the spectroscopy and excitation dynamics of Tm^{3+} and Ho^{3+} in Lithium Yttrium Fluoride has been done. Quantitative as well as qualitative approaches have been taken towards the interpretation of the experimental data. This is particularly evident in chapter 7, where the various energy transfer processes are discussed and interpreted. A purely quantitative approach is limiting in scope and does not always lead to new ideas. It can, in fact, be misleading especially where modeling is concerned. The construction of a model that fits the data well does not imply the model is correct. The physical reasoning behind it must be sound also. So, attempts have been made to discuss at length the reasoning behind the ideas presented.

The introductory chapters (chapters 1-4) laid the groundwork for this study. A thorough introduction was presented in chapter 1 to familiarize the reader with the subject under study, and to give a sense of the direction this thesis would take. A brief preview of the contents and results were also presented to peak the interest of potential readers. The theoretical background was given in chapter 2. This is material which is well known. The classic textbooks of Di Bartolo, Wybourne, Judd and Dieke really have no

substitute, all written during the 1960's when laser spectroscopy was a new field. Chapter 3 covered the details of the YLF host lattice. While the properties of symmetry and group theoretical treatment of the crystal field effects on ions in solid state materials is a fascinating subject in itself, only the details and topics necessary to an understanding of the phenomena discussed here were presented. Chapter 4 carefully detailed the experimental apparatus and techniques used in the data collection. None of the experiments were novel or new, but are well worn favorites.

Chapters 5 through 7 constitute the presentation of the data and the analysis. They form, in a sense, a trilogy: The results and interpretation of YLF:Tm, The results and interpretation of YLF:Ho, and the results and interpretation of YLF:Tm,Ho. The outcome of a Judd-Ofelt analysis on YLF:Tm and YLF:Ho were given. Manifold to manifold radiative lifetiimes and branching ratios were determined. Comparison of emission and absorption cross sections provided an alternate method for extracting radiative lifetimes.The correspondence between the radiative lifetimes calculated by the two methods was satisfactory. They both gave results in the same order of magnitude and, in fact, differed by less than a factor of two.

A limited presentation and discussion of the excitation dynamics of singly doped YLF:Ho was given at the end of chapter 5. It was very interesting to discover that the green luminescence from the Ho $^5S_2$ was observed when exciting the Ho $^5I_5$ and also when exciting the Ho $^5F_5$, both of which lie lower in energy than the Ho $^5S_2$. Some kind of upconversion in Ho is evident from this observation, but all of the manifolds studied had nearly the same decay behavior whether they were excited directly or not. The conclusion is that this upconversion is rather weak or the result of excited state absorption by a second pump photon.

In chapter 6, the excitation dynamics of YLF:Tm was discussed. Under $^3H_4$

excitation, the concentration dependence of the $^3H_4$ fluorescence was examined. The concentration quenching is generally interpreted as a process in which an ion initially excited to the $^3H_4$ state interacts with an unexcited ion in the $^3H_6$ ground state. The ion in the $^3H_4$ state gives up part of its energy to the ion in the $^3H_6$ state, producing two ions in the $^3F_4$ state.This energy transfer process is called cross relaxation and is referred to notationally as $Tm(^3H_4 \rightarrow ^3F_4);Tm(^3H_6 \rightarrow ^3F_4)$. This process was seen to be accompanied by energy migration amonq Tm ions within the $^3H_4$ state $Tm(^3H_4 \rightarrow ^3H_6);Tm(^3H_6 \rightarrow ^3H_4)$. The migration was interpreted as a hopping process in which the energy migrates in a random walk process among ions in the $^3H_4$ state until it happens to hop onto a quenching center where cross relaxation takes place. The hopping model was used to find the interaction strengths of the migration and cross relaxation processes (C_{DA}, and C_{DD}) by fitting the model equation to measured decay curves of the $^3H_4$ fluorescence. The values of the interaction parameters obtained from the hopping model were compared to the values obtained from the Förster-Dexter theory by calculating the appropriate spectral overlap integral. Good agreement was found between these two methods. In both cases it was found that $C_{DA}<C_{DD}$, within the range of applicability of the hopping mechanism.

In chapter 7, various energy transfer processes in co-doped YLF:Tm,Ho were examined. Under cw diode laser excitation of the Tm $^3H_4$, co-doped YLF:Tm,Ho was seen to exhibit fluoresence at many different wavelengths. The transitions corresponding to these wavelengths were seen to originate from both Tm and Ho ions, indicating the presence of energy transfer from Tm to Ho. Some of these processes were examined by directly exciting the manifolds involved in the energy transfer with a pulsed laser source tuned to the appropriate wavelength.

Of particular interest, due to its importance for understanding 2.0μm YLF:Tm,Ho

lasers, is the energy transfer from the Tm $^3F_4$ to the Ho $^5I_7$ Tm($^3F_4$–>$^3H_6$);Ho($^5I_8$–> $^5I_7$). This transfer was found to occur in both directions, with the Tm->Ho transfer occuring more rapidly than the Ho->Tm transfer. A state of equillibrium between Tm ions in the $^3F_4$ and Ho ions in the $^5I_7$ sets in quickly (100-400μs) after which the Tm and Ho ions decay at the same rate

To probe into the dynamics of this energy transfer process the Tm $^3F_4$ manifold was excited directly with a $CoMgF_2$ pulsed laser, and the time dependence of the Tm $^3F_4$ and Ho $^5I_7$ fluorescence decay was measured. A rate equation model for this Tm->Ho energy transfer was developed, and used to model the decay behavior. For the excitation density in our experiments, it was discovered that the non-linear terms in the rate equations were unimportant. This allowed us to solve the set of coupled differential equations in closed form. The closed form solutions were fit to the experimental data collected for various Tm,Ho dopant ion concentrations. Rate constants for the Tm->Ho energy transfer and Ho->Tm backtransfer were extracted from the best fit to the data. The rate constants showed only minor variation within the range of Tm,Ho concentrations studied, indicating the success of the model, despite the fact that the model did not exactly fit the experimental data. The basis for this reasoning is that the rate constants represent an average transfer rate, and are only capable of predicting an average bahavior within the framework of the model. In reality, the transfer rates will depend on the spatial distribution of Tm and Ho ions in the crystal, and on the thermal distribution of excitations within the Stark levels of the manifolds involved in the energy transfer.

Tables 8-1 and 8-2 compile some values generated by this thesis that may be useful for researchers interested in the design of YLF:Tm,Ho lasers.

Table 8-1 Useful Values and Parameters for YLF Tm,Ho

	Symbol and value
Judd Ofelt Parameters Ho YLF	$\Omega_2 = 0.7483 \times 10^{-20}$ cm^2 $\Omega_2 = 1.6168 \times 10^{-20}$ cm^2 $\Omega_2 = 1.2269 \times 10^{-20}$ cm^2
Judd Ofelt Parameters Tm YLF	$\Omega_2 = 1.6673 \times 10^{-20}$ cm^2 $\Omega_2 = 1.9184 \times 10^{-20}$ cm^2 $\Omega_2 = 1.0897 \times 10^{-20}$ cm^2
Energy level range in Ho YLF	ΔE_{5I7} (5153-5293cm^{-1}), ΔE_{5I8} (0-315cm^{-1})
Energy level range in Tm YLF	ΔE_{3F4} (5599-5972cm^{-1}), ΔE_{3H6} (0-419cm^{-1})
Partition functions in Ho YLF	$Z_{5I7} = 11.415$, $Z_{5I8} = 9.199$
Partition functions in Tm YLF	$Z_{3F4} = 3.432$, $Z_{3H6} = 5.207$
Radiative lifetimes in Ho YLF	$\tau_{5I5} = 7.0$ ms, $\tau_{5I6} = 5.6$ ms, $\tau_{5I7} = 14.0$ms
Radiative lifetimes in Tm YLF	$\tau_{3H4} = 2.4$ ms, $\tau_{3F4} = 15.6$ms
Emission cross sections of Ho $^5I_7$	$\sigma = 1.2286 \times 10^{-20}$ cm^2 (π-pol.,E // c) @2.06μm $\sigma = 0.6530 \times 10^{-20}$ cm^2 (σ-pol.,E $\perp$ c)@2.06μm
Absorption cross section of Tm $^3H_4$ @785 nm	0.312×10^{-20} cm^2 (same for π-pol. and σ-pol.)

Table 8-2 Measured Energy Transfer Parameters

	Value
Interaction parameter of Tm-Tm cross-relaxation: $Tm(^3H_4 \rightarrow ^3F_4);Tm(^3H_6 \rightarrow ^3F_4)$	$C_{DA} = 4.7402 \times 10^{-47}$ cm^6/μs
Interaction parameter of Tm-Tm migration $Tm(^3H_4 \rightarrow ^3H_6);Tm(^3H_6 \rightarrow ^3H_4)$	$C_{DD} = 2.7238 \times 10^{-45}$ cm^6/μs
Interaction parameter of Tm->Ho energy transfer: $Tm(^3F_4 \rightarrow ^3H_6);Ho(^5I_8 \rightarrow ^5I_7)$	$C_{DA} = 1.6905 \times 10^{-45}$ cm^6/μs
Interaction parameter of Ho->Tm energy transfer: $Ho(^5I_7 \rightarrow ^5I_8)Tm(^3H_6 \rightarrow ^3F_4)$	$C_{DA} = 1.2424 \times 10^{-46}$ cm^6/μs
Rate constant of Tm->Ho energy transfer: $Tm(^3F_4 \rightarrow ^3H_6);Ho(^5I_8 \rightarrow ^5I_7)$	$p28 = 6.979 \times 10^{-23}$ cm^3/μs
Rate constant of Ho->Tm energy transfer: $Ho(^5I_7 \rightarrow ^5I_8);Tm(^3H_6 \rightarrow ^3F_4);$	$p71 = 1.057 \times 10^{-23}$ cm^3/μs
Rate constant of Tm-Ho upconversion $Tm(^3F_4 \rightarrow ^3H_6);Ho(^5I_7 \rightarrow ^5I_5)$	$p27 = 7.560 \times 10^{-24}$ cm^3/μs
Rate constant of Ho-Tm cross relaxation: $Ho(^5I_5 \rightarrow ^5I_7)Tm(^3H_6 \rightarrow ^3F_4);$	$p51 = 1.2058 \times 10^{-22}$ cm^3/μs
Rate constant of Tm-Ho upconversion $Tm(^3H_4 \rightarrow ^3H_6);Ho(^5I_7 \rightarrow ^5S_2)$	$p91 = 2.59 \times 10^{-23}$ cm^3/μs

8.2 Suggestions For Future Work

This thesis represents a comprehensive study of the spectroscopy and excitation dynamics of YLF:Tm,Ho at room temperature. A proper characterization of the temperature dependence of many of the phenomena discussed in this thesis has yet to be done. Phonons play an important role in the absorption, emission and energy transfer processes in Rare-Earth doped solid-state materials, and a better understanding of some of these processes would be gained by studies of the behavior at low temperatures, and at high temperature. This is especially true in the case of the Tm-Tm cross-relaxation and Tm->Ho transfer. It would be interesting to see if the models proposed in this thesis to describe the observed decay behavior remained valid at low temperatures and at high temperatures.

Another area that provides a direction for future work is the use of more sofisticated techniques to probe into the energy transfer processes. Time resolved studies, for instance, can reveal information about the individual Stark levels participating in the transfer process by observing the fluorescence at various delay times after the excitation pulse. Time resolved studies of the Tm->Ho energy transfer would improve the understanding of the Tm<->Ho energy sharing.

Concerning the models used to describe the experimental data in this thesis, there is always room for improvement. New experimental techniques lead to a greater finesse in the methodology that inevitably produces new physical insights into the processes being studied. The new physical insights allow for refinements in the present models or possibly entirely new models.

Appendix A Beer-Lambert Law for a Uniaxial Crystal

For a uniaxial crystal, such as $LiYF_4$, the polarization variation for the attenuation of an electromagnetic wave can be derived. We consider an incident electromagnetic wave propagating in an arbitrary direction described by the wave vector $\vec{k}$. This is pictured in figure A-1.

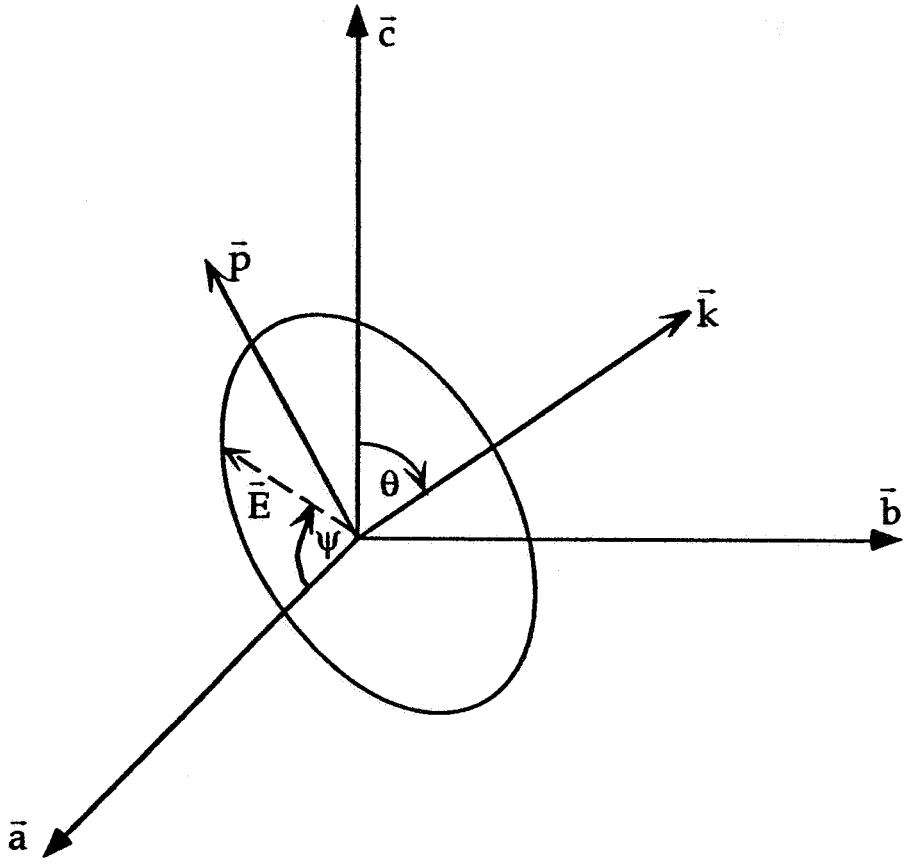

Figure A-1 Coordinate System for Arbitrary direction of Propagation

The angle between the wave vector $\vec{k}$ and the c-axis is θ. The incoming E-vector is randomly oriented in the p-a plane, where the p-axis denotes the polarization axis. The orientation of $\vec{E}$ transverse to $\vec{k}$ is given by the angle ψ. For a beam (with a polarization described by ψ) of intensity I_o incident on a uniaxial crystal at some arbitrary angle θ

with respect to the c-axis, the transmitted light through the crystal can be written, after some geometrical considerations as:

$$I(\lambda;\theta,\varphi,\psi) = I_0\left\{\sin^2\psi\sin^2\theta\exp[-\alpha_\pi(\lambda)\ell] + (\cos^2\psi + \sin^2\psi\cos^2\theta)\exp[-\alpha_\sigma(\lambda)\ell]\right\} \tag{A-1}$$

Note that this result is independent of the azimuthal angle ϕ. For an unpolarized beam, we must average over the polarization angle ψ from 0 to 2π. The result is:

$$I(\lambda;\theta,\varphi) = \tfrac{1}{2}I_0\left\{\sin^2\theta\exp[-\alpha_\pi(\lambda)\ell] + (1+\cos^2\theta)\exp[-\alpha_\sigma(\lambda)\ell]\right\} \tag{A-2}$$

The spatially averaged transmitted intensity over the angles θ, ϕ is:

$$I(\lambda) = \tfrac{1}{2}I_0\frac{\int_0^{2\pi}d\varphi\int_0^{\pi}\left\{\sin^2\theta\exp[-\alpha_\pi(\lambda)\ell] + (1+\cos^2\theta)\exp[-\alpha_\sigma(\lambda)\ell]\right\}\sin\theta d\theta}{\int_0^{2\pi}d\varphi\int_0^{\pi}\sin\theta d\theta} \tag{A-3}$$

Performing this integration we find the result:

$$I(\lambda) = I_0\left\{\tfrac{1}{3}\exp[-\alpha_\pi(\lambda)\ell] + \tfrac{2}{3}\exp[-\alpha_\sigma(\lambda)\ell]\right\} \tag{A-4}$$

The absorption coefficients can be written in terms of the absorption cross sections $\sigma_\pi=\alpha_\pi/N$ and $\sigma_\sigma=\alpha_\sigma/N$. Thus, eq. 5-1 is obtained:

$$I(\lambda) = I_0\left\{\tfrac{1}{3}\exp[-\sigma_\pi(\lambda)N\ell] + \tfrac{2}{3}\exp[-\sigma_\sigma(\lambda)N\ell]\right\} \tag{A-5}$$

Appendix B Least Squares Fitting Equation for Judd-Ofelt Parameters

In order to find the set of Judd-Ofelt parameters that minimizes the sum of the squares of the differences between the theoretical and experimental linestrengths, begin with the matrix equation 5-5 for the theoretical linestrength:

$$\mathbf{S} = \mathbf{M}\Omega \tag{B-1}$$

This can be written in component form as:

$$S_j = \sum_{i=1}^{n} M_{ji}\Omega_i \tag{B-2}$$

We want to minimize the expression:

$$\chi^2 = \sum_{i=1}^{n} \left(S_j - S_j^E\right) \tag{B-3}$$

where S_j^E is the experimental linestrength. This is achieved by taking the derivative:

$$\frac{\partial \chi^2}{\partial \Omega_k} = \frac{\partial}{\partial \Omega_k} \sum_{j=1}^{n} \left[\sum_{i=1}^{n} M_{ji}\Omega_i - S_j^E \right]^2 \tag{B-4}$$

and setting it equal to zero. This is easily done, and the result is:

$$\sum_{j=1}^{n} M_{jk} \sum_{i=1}^{n} M_{ji}\Omega_i = \sum_{j=1}^{n} M_{jk} S_j^E \tag{B-5}$$

The right hand side of eq. B-5 has the same form as eq. B-2 for the theoretical linestrength. The only difference is in the order of the indicies. So, recalling that the definition of the adjoint of a matrix, we can write $M_{jk} = M^{\dagger}_{kj}$. Eq. B-5 becomes:

$$\sum_{i=1}^{n}\left[\sum_{j=1}^{n} M^{\dagger}_{kj} M_{ji} \Omega_i\right] = \sum_{j=1}^{n} M^{\dagger}_{kj} S^{E}_{j} \qquad \text{(B-6)}$$

This substitution has the effect of turning the right hand side of eq. B-5 from a row matrix to a column matrix. In matrix form this is:

$$\mathbf{M^{\dagger} M \Omega^{o} = M^{\dagger} S^{E}} \qquad \text{(B-7)}$$

Eq. 5-6 then follows from the above expression:

$$\mathbf{\Omega^{o} = (M^{\dagger} M)^{-1} M^{\dagger} S^{E}} \qquad \text{(B-8)}$$

which gives the set of Judd-Ofelt parameters Ω^{o} that minimizes eq. B-3.

Appendix C System Response Calibration for Luminescence Measurements

It is possible to take into account the signal response of the experimental apparatus as a function of wavelength. Depending upon the spectrometer grating, detector, optics, polarizers, etc. the measured signal will have a wavelength dependent variation. For example, a grating has its highest efficiency at the Blaze wavelength, and becomes less efficient the further the wavelength is from the Blaze wavelength. Detectors have a characteristic responsivity that varies with wavelength. All of the effects that cause fluctuations in the signal level with changes in wavelength can be corrected for with the use of a lamp of known temperature.

Suppose a luminescence spectrum is obtained. By introducing a correction function $h(\lambda)$ we can write:

$$L_{meas} = h(\lambda)L_{real} \qquad \text{(C-1)}$$

where L_{meas} is the measured luminescence spectrum and L_{real} is the actual luminescence spectrum. The function $h(\lambda)$ takes care of the wavelength dependent changes in signal level due to the experimental apparatus.

Similarly, we can obtain a spectrum of the temperature lamp. The temperature lamp simulates a blackbody source and will have a spectrum that is similar to a Planck distribution curve for the given temperature. Therefore we can write:

$$P_{meas} = h(\lambda)P_{planck} \qquad \text{(C-2)}$$

Combining equations C-1 and C-2 the real luminescence spectrum is found:

$$L_{real} = \frac{P_{planck}}{P_{meas}} L_{meas} \qquad \text{(C-3)}$$

In order to find the real luminescence spectrum, we must obtain the luminescence and lamp spectra under the same conditions and wavelength range. The Planck curve can be calculated if the temperature of the lamp filament is known. A convenient form for the power radiated by a blackbody per unit area per wavelength interval is:

$$W_\lambda = \frac{C_1}{\lambda^5 [\exp(C_2 / \lambda T) - 1]}$$

where,

$C_1 = 2\pi c^2 h = 3.746 \times 10^5$ mW-cm^2

$C_2 = hc/k_B = 1.438 \times 10^7$ nm-°K

T = lamp temperature

c = velocity of light

h = Planck's constant

k_B = Boltzmann's constant

All of the spectra required to calculate the real luminescence spectrum corrected for system response through eq. C-3 can be combined with a suitable computer program or a commercial graphing application such as Kaleidagraph or Cricket Graph.

Appendix D Closed Form Solution to Rate Equations for Tm->Ho Energy Transfer

We begin with the linearized form ($n_2 n_7 = 0$) of equations 7-14:

$$\frac{dn_2}{dt} = -\frac{n_2}{\tau_2} - \alpha n_2 + \beta n_7 \qquad \text{(D-1a)}$$

$$\frac{dn_7}{dt} = -\frac{n_7}{\tau_7} + \alpha n_2 - \beta n_7 \qquad \text{(D-1b)}$$

We take as a trial solution: $n_2(t) = A_2 \exp(-\gamma t)$ and $n_7(t) = A_7 \exp(-\gamma t)$. The trial solutions are then substituted back into equations D-1a and D-1b. The result is two equations:

$$\left(\gamma - \frac{1}{\tau_2} - \alpha\right) A_2 + \beta A_7 = 0 \qquad \text{(D-2a)}$$

$$\left(\gamma - \frac{1}{\tau_7} - \beta\right) A_7 + \alpha A_2 = 0 \qquad \text{(D-2b)}$$

Solving these equations for γ leads to a quadratic equation:

$$\gamma^2 - \left(\frac{1}{\tau_7} + \frac{1}{\tau_2} + \alpha + \beta\right)\gamma + \left(\frac{1}{\tau_2 \tau_7} + \frac{\alpha}{\tau_7} + \frac{\beta}{\tau_2}\right) = 0 \qquad \text{(D-3)}$$

The solution to eq. D-3 is:

$$\gamma = \frac{1}{2}\left(\frac{1}{\tau_7} + \frac{1}{\tau_2} + \alpha + \beta\right) \pm \frac{1}{2}\sqrt{\left(\frac{1}{\tau_7} + \frac{1}{\tau_2} + \alpha + \beta\right)^2 - 4\left(\frac{1}{\tau_2 \tau_7} + \frac{\alpha}{\tau_7} + \frac{\beta}{\tau_2}\right)} \qquad \text{(D-4)}$$

This can be rearranged into the form:

$$\gamma = \frac{1}{2}\left(\frac{1}{\tau_7}+\frac{1}{\tau_2}+\alpha+\beta\right) \pm \frac{1}{2}\sqrt{\left(\frac{1}{\tau_2}-\frac{1}{\tau_7}\right)^2 + 2(\alpha-\beta)\left(\frac{1}{\tau_2}-\frac{1}{\tau_7}\right)+(\alpha+\beta)^2} \quad \text{(D-5)}$$

At this point we can make the reasonable assumption that the energy transfer rates are much faster than the lifetimes of the Tm,Ho manifolds. That is:

$$\left(\frac{1}{\tau_2}-\frac{1}{\tau_7}\right)^2 << (\alpha+\beta)^2 \quad \text{(D-6)}$$

Equation D-5 can now be written as:

$$\gamma = \frac{1}{2}\left(\frac{1}{\tau_7}+\frac{1}{\tau_2}+\alpha+\beta\right) \pm \frac{1}{2}(\alpha+\beta)\sqrt{1+\frac{2(\alpha-\beta)}{(\alpha+\beta)^2}\left(\frac{1}{\tau_2}-\frac{1}{\tau_7}\right)} \quad \text{(D-7)}$$

Invoking the binomial expansion $(1+x)^{1/2} = 1+ nx + [n(n-1)/2]x^2 + ...$ and keeping only terms to first order:

$$\gamma = \frac{1}{2}\left(\frac{1}{\tau_7}+\frac{1}{\tau_2}+\alpha+\beta\right) \pm \frac{1}{2}\left[\alpha+\beta+\frac{\alpha-\beta}{\alpha+\beta}\left(\frac{1}{\tau_2}-\frac{1}{\tau_7}\right)\right] \quad \text{(D-8)}$$

This equation leads to two solutions:

$$\gamma_1 = \alpha+\beta+\frac{1}{\alpha+\beta}\left(\frac{\alpha}{\tau_2}+\frac{\beta}{\tau_7}\right) \quad \text{(D-9a)}$$

$$\gamma_2 = \frac{1}{\alpha+\beta}\left(\frac{\alpha}{\tau_2}+\frac{\beta}{\tau_7}\right) \quad \text{(D-9b)}$$

The trial solutions are now modified to be a linear combination of exponentials for the two possible gammas:

$$n_2(t) = A_2 \exp(-\gamma_1 t) + B_2 \exp(-\gamma_2 t) \qquad \text{(D-10a)}$$

$$n_7(t) = A_7 \exp(-\gamma_1 t) + B_7 \exp(-\gamma_2 t) \qquad \text{(D-10b)}$$

The exponential coefficients are found by substituting equations D-9 into equations D-10 and by considering the initial excitation conditions (@t=0 pumping Tm $n_2(0) = n_{20}$, $n_7(0) = 0$). Making the assumption again that the energy transfer rates are much faster than the lifetimes of the manifolds and that the manifolds reach equillibrium quickly ($\tau_2 = \tau_7$) then the final result is:

$$\frac{n_2(t)}{n_2(0)} = \left(\frac{\beta}{\alpha+\beta}\right)\exp(-t/\tau) + \left(\frac{\alpha}{\alpha+\beta}\right)\exp[-(\alpha+\beta)t] \qquad \text{(D-11a)}$$

$$\frac{n_7(t)}{n_2(0)} = \left(\frac{\alpha}{\alpha+\beta}\right)\exp(-t/\tau) - \left(\frac{\alpha}{\alpha+\beta}\right)\exp[-(\alpha+\beta)t] \qquad \text{(D-11b)}$$

which are the equations 7-14a and 7-14b.

Appendix E Expression For Ratio of Rate Constants for Resonant Transfer

We begin with writing the rate constants as a summation over the initial and final levels of Ho, and the initial and final levels of Tm for the Tm<–> Ho energy transfer:

$$p_{28} = \sum_{jk}\sum_{i\ell} w_{i\ell} p_i p_\ell \tag{E-1a}$$

$$p_{71} = \sum_{i\ell}\sum_{jk} w_{jk} p_j p_k \tag{E-1b}$$

Writing the Boltzmann fractions out explicitly, these equations can written as:

$$p_{28} = \frac{1}{Z_2 Z_8}\sum_{i\ell}\sum_{jk} w_{i\ell} \exp(-\Delta E_i / k_B T)\exp(-\Delta E_\ell / k_B T) \tag{E-2a}$$

$$p_{71} = \frac{1}{Z_7 Z_1}\sum_{i\ell}\sum_{jk} w_{jk} \exp(-\Delta E_j / k_B T)\exp(-\Delta E_k / k_B T) \tag{E-2b}$$

The Stark level energies for an ion in the upper manifold can be written in terms of the zero line energy, Stark level energy of the lower manifold, and the energy difference between the upper and lower Stark levels. This procedure is similar to that discussed in chapter 2, section 6. The result is:

$$\Delta E_i = \Delta E_j + h\nu_{ij} - E_{ZL}^{3F4} \tag{E-3a}$$

$$\Delta E_k = \Delta E_\ell + h\nu_{k\ell} - E_{ZL}^{5I7} \tag{E-3b}$$

Inserting these in equations E-2 we find:

$$p_{28} = \frac{\exp(E_{ZL}^{3F4} / k_B T)}{Z_2 Z_8} \sum_{i\ell} \sum_{jk} w_{i\ell} \exp\left[(-\Delta E_j - \Delta E_\ell) / k_B T\right] \exp(-h\nu_{ij} / k_B T) \quad \text{(E-4a)}$$

$$p_{71} = \frac{\exp(E_{ZL}^{5I7} / k_B T)}{Z_7 Z_1} \sum_{i\ell} \sum_{jk} w_{jk} \exp\left[(-\Delta E_j - \Delta E_\ell) / k_B T\right] \exp(-h\nu_{k\ell} / k_B T) \quad \text{(E-4b)}$$

For resonant transitions we would expect $\nu_{ij} = \nu_{k\ell}$, and $w_{i\ell} = w_{kj}$. So, the terms in summation in E-4a and E-4b are equal. Taking the ratio of E-4a and E-4b, then, we have Equation 7-16:

$$\frac{p_{71}}{p_{28}} = \frac{Z_2 Z_8}{Z_1 Z_7} \exp\left[-(E_{ZL}^{3F4} - E_{ZL}^{5I7}) / k_B T\right] \quad \text{(E-5)}$$

This equation is a general relation for any resonant sets of energy levels, and is applicable to other sets of energy levels, not just the ones discussed here.

REPORT DOCUMENTATION PAGE

Form Approved
OMB No. 0704-0188

1. AGENCY USE ONLY *(Leave blank)*	2. REPORT DATE	3. REPORT TYPE AND DATES COVERED
	August 1995	Contractor Report

4. TITLE AND SUBTITLE
Spectroscopy and Excitation Dynamics of the Trivalent Lanthanides Tm^{3+} and Ho^{3+} in $LiYF_4$

5. FUNDING NUMBERS
G NAG1-955

WU 233-01-03-08

6. AUTHOR(S)
Brian M. Walsh

7. PERFORMING ORGANIZATION NAME(S) AND ADDRESS(ES)
Boston College
Department of Physics
Chestnut Hill, MA 02167

8. PERFORMING ORGANIZATION REPORT NUMBER

9. SPONSORING / MONITORING AGENCY NAME(S) AND ADDRESS(ES)
NASA Langley Research Center
Hampton, VA 23681

10. SPONSORING / MONITORING AGENCY REPORT NUMBER
NASA CR-4689

11. SUPPLEMENTARY NOTES
The information presented in this report was offered as a thesis in partial fulfillment of the requirements for the Degree of Doctor of Philosophy, Boston College, September 1995.
Langley Technical Monitor: Norman P. Barnes

12a. DISTRIBUTION / AVAILABILITY STATEMENT
Unclassified - Unlimited

Subject Category 76

12b. DISTRIBUTION CODE

13. ABSTRACT ***(Maximum 200 words)***

A detailed study of the spectroscopy and excitation dynamics Tm3+ and Ho3+ in Yttrium Lithium Fluoride, LiYF4 (YLF), has been done. Absorption spectroscopy is utilized in the Judd-Ofelt theory to determine radiative transition rates of spontaneous emission. Luminescence spectroscopy is studied under cw diode laser excitation at 785nm. The effect of dopant ion concentration and excitation power on the observed luminescence are considered in these measurements. An analysis of these measurements have been used to determine channels of energy transfer between Tm3+ and Ho3+ ions. The temporal response of Tm and Ho in singly and co-doped YLF to pulsed laser excitation with a Ti:Al2O3 laser and a CoMgF2 laser tuned to various wavelengths have also been studied. The energy transfer mechanisms of cross relaxation, upconversion, and resonant energy transfer between Tm3+ and Ho3+ ions have been modeled, and the model parameters extracted by a fitting procedure to the measured temporal response curves. Rate equation approaches to modeling are presented that result in predictions of rate constants for energy transfer processes, as well as more conventional approaches to modeling such as the Forster-Dexter models, which give the interaction strengths in terms of microscopic interaction parameters.

14. SUBJECT TERMS
Solid State Lasers
Rare Earth Ions in Solids
Energy Transfer
Spectroscopy of Solid-State Laser Materials

15. NUMBER OF PAGES
170

16. PRICE CODE
A08

17. SECURITY CLASSIFICATION OF REPORT	18. SECURITY CLASSIFICATION OF THIS PAGE	19. SECURITY CLASSIFICATION OF ABSTRACT	20. LIMITATION OF ABSTRACT
Unclassified	Unclassified	Unclassified	